Radiative reverse shock experiments in high-energy-density plasmas

by

Christine M. Krauland

A dissertation submitted in partial fulfillment
of the requirements for the degree of
Doctor of Philosophy
(Applied Physics)
in The University of Michigan
2013

Doctoral Committee:

Professor R Paul Drake, Co-Chair
Assistant Research Scientist Carolyn C. Kuranz, Co-chair
Professor Fred C. Adams
Assistant Professor Eric Johnsen
Professor Ken Powell

To the hope that one day I will be the slightest bit closer to these systems we study.

ACKNOWLEDGEMENTS

Firstly, I want to thank my graduate students peers, past and present, in the Drake lab research group; Tony Visco, Forrest Doss, Channing Huntington, and Carlos Di Stefano, who shared many useful discussions regarding relevant physics, OMEGA experimental constraints, and occasional words of wisdom. I appreciated sharing much of my graduate experience with them.

I would also like to acknowledge the extensive contributions of the target fabrication team within our lab at the University of Michigan, especially Donna Marion, Sallee Klein, Phil Bonofiglo, and David Kaczala, who built, transported and organized my targets. I would not have had nearly as many 2D/3D simulations without the efforts of Mike Grosskopf. His contributions also in mentoring others, particularly Ryan Sweeney, wholly contributed to computational output for this experiment.

Thank you also to the technical staff at the Omega Laser facility, without whom none of these experiments could have been executed. Thank you especially to Steve Stagnitto, Jack Armstrong, Andrew Sorce and Chuck Sorce for always having the patience to deal with our Michigan targets and changes.

I have also had many helpful discussions with an international group of collaborators, which includes Michel Koenig, Berenice Loupias and Emeric Falize. I appreciate their help and participation in this parallel method of experimentation.

I want to thank my family and friends for always supporting me in my decision to stay in college for a decade. Without their contributions (of reminding me to have fun), I probably could have graduated and joined the real world much sooner. I love

you Mom, Dad, and Rick for keeping me grounded, and thank you to the Kaczala's who gave Jack and me a home away from home.

I want to especially thank Dr. Carolyn Kuranz for being my mentor (in life) during this time. She was always more than just my co-chair, and I am forever grateful that she got pregnant with her son because I would likely not be here otherwise! Most importantly, I want to thank my advisor Paul Drake, who has always given me the support that I needed whether I realized it at the time or not. I'm very lucky to have completed my graduate work under his supervision.

Lastly, I want to thank my committee for giving my their time and interest in my work.

TABLE OF CONTENTS

LIST OF FIGURES

Figure

LIST OF TABLES

Table

LIST OF APPENDICES

Appendix

LIST OF ABBREVIATIONS

HED high-energy-density

HEDLA high-energy-density laboratory astrophysics

CV cataclysmic variable

WD white dwarf

1D one dimensional

2D two dimensional

3D three dimensional

RLOF Roche Lobe overflow

$\mathbf{L}_1$ inner Lagrangian point

$\mathbf{B}_{WD}$ Magnetic field strength of white dwarf

EOS equation of state

LLE Laboratory for Laser Energetics

DPP distributed phase plate

SSD smoothing by spectral dispersion

BXMS bremsstrahlung spectrometer

ITS INTEGRATED TIGER SERIES

XRPHC x-ray pinhole camera

CID charge-injection device

SOP Streaked optical pyrometer

CCD charged-coupling device

SEM scanning electron microscope

CRASH Center for Radiative Shock Hydrodynamics

KH Kelvin-Helmholtz

IDL Interactive Data Language

NIF National Ignition Facility

LLNL Lawrence Livermore National Laboratory

MPBL Magnetic Point Backlighter

ABSTRACT

Radiative reverse shock experiments in high-energy-density plasmas

by

Christine Krauland

Co-Chair: R Paul Drake Co-chair: Carolyn C. Kuranz

This thesis presents the development of a new high-energy-density laboratory astrophysics (HEDLA) experimental platform that explores radiative reverse shock waves. In the context of this work, a reverse shock is a shock wave that develops when a freely flowing, supersonic plasma is impeded. Obtaining a radiative reverse shock in the laboratory requires a sufficiently fast flow (> 60 km/s) within a material whose opacity is large enough to produce energetically significant emission from experimentally achievable layers. Data show that when these conditions are met, the post-shock material evolution is quite different than in an analogous purely hydrodynamic system. In the case where a plasma flow collides orthogonal to a surface, radiative losses cause the collapse of shocked material to high densities, such that the compression across the shock is $\gg 4$. Additionally, when a stream impacts a surface at an angle, an oblique shock will divert the material moving through it, creating a supersonic shear flow that may become unstable.

This work is motivated by the ambiguities that surround reverse radiative shocks and their contribution to the evolving dynamics of the cataclysmic variable in which they occur. Cataclysmic variables (CVs) are close binary star systems containing

a white dwarf (WD) which accretes matter from its late-type main sequence companion star. They can be classified under two main categories, non-magnetic and magnetic. In the process of accretion, both types involve strongly radiating shocks that provide the main source of radiation in the binary systems. In the case of the non-magnetic CV, mass onto an accretion disk produces this 'hot spot', where the infalling supersonic flow obliquely strikes the rotating accretion disk. Astrophysical simulations of this collision region show various outcomes as a function of the code's treatment of radiative cooling [3]. Ultimately, HEDLA experiments aim to bridge the gap between theoretical models and observations, and the design of laboratory experiments presented in this text suggest that correlations may be made to the CV system.

This thesis assembles data taken at the Omega-60 laser facility over four experimental campaigns: August 5, 2010; June 15, 2011; September 8, 2011; and July 19, 2012. Simulations from one-dimensional (1D) and two-dimensional (2D) radiation hydrodynamics codes accompany this work and are included.

CHAPTER I

Introduction

The aim of this thesis work is to experimentally address the hydrodynamic and radiative properties of a reverse shock wave in connection with a cataclysmic binary system. The experimental goal is to produce a similar shock system that occurs at the point of material interaction between the two stars. While there are various classifications under the binary umbrella, multiple star systems collectively occur more frequently than single stars in our galaxy. Ultimately, this experimental work could be used to bridge astrophysical theory and simulation in understanding the evolution of the particular Cataclysmic Variable binary star systems. In this chapter, the details of the astrophysical system are presented as well as implications suggested by observational data and simulations. A brief description is given on the field of high-energy-density laboratory astrophysics, followed by an overview of how the laboratory experiments presented in this thesis may be comparable to particular categorizations of the binary systems. This chapter concludes with a brief description of the later chapters in this thesis.

1.1 Non-magnetic cataclysmic variable system

Over the last half century, there has been extensive astrophysical research on dwarf novae, novae, and nova-like systems, which are all categorized as cataclysmic

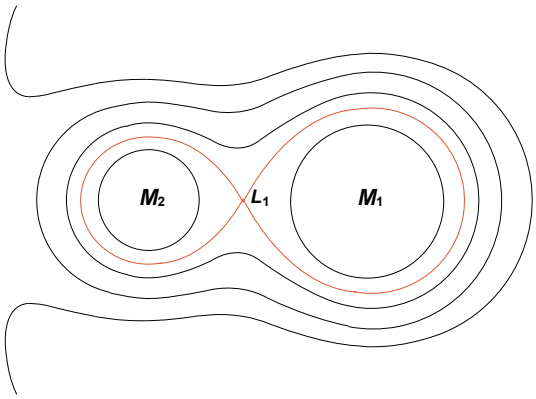

Figure 1.1: Contours of equal gravitational potential drawn for a binary in which M_2 is half of the mass of M_1. The stars orbit in the plane of the paper. The potential surfaces (red) just touching L_1 point are the Roche lobes of the two stars.

variables (CVs) [90]. CVs are binary star systems consisting of a white dwarf (WD) and a late-type main sequence star. Much CV work has shown that the nature of these systems depends on the gas flow from the cool companion star (i.e. the secondary) to the WD (i.e. primary) [56]. The secondary, though larger, is less dense than the WD and distorted by the gravity of the WD. In the course of its evolution, mass flows away from the secondary star. Once it fills its largest closed equipotential surface in the binary system, known as the Roche lobe, it begins to overflow [77]. This Roche Lobe overflow (RLOF) is distinguished by the loss of mass through the point in the system between the stars where their combined gravitational pull provides precisely the centripetal force required to maintain stable orbit with them. This is known as the inner Lagrangian point (L_1) [18, 66], depicted in Figure 1.1. Systems that undergo RLOF are also referred to as a semi-detached binaries. One important consequence of these systems is that the companion star spins at the same rate that it orbits (known as tidal locking), mitigating tidal flows through its Roche lobe.

As the material moves through L_1, it is injected into the empty Roche lobe of the WD at roughly the sound speed in the gas ($\sim$10 km/s). However, L_1 is orbiting perpendicular to this motion at 100s of km/s. The CVs of interest here can be considered

non-magnetic ($\mathbf{B}_{WD} < 1$ MG), such that the mass transfer is not affected by a WD magnetic field. The supersonic gas leaves L_1 in a coherent stream with approximately gaussian density profiles in the two directions perpendicular to its ballistic trajectory [59], Figure 1.2(a). Conservation of angular momentum and viscous processes cause the stream to flow around the WD during initial mass transfer (with the trajectory lying entirely in the orbital plane of the binary) and spread into an accretion disk [88], shown in Figure 1.2(b)-1.2(d). Angular momentum flows outward through the disk, enabling the inward flow of material such that it can accrete onto the white dwarf surface. Tidal interactions with the main sequence star limit the outer spread of the disk. The mass transfer maintains the existence of the disk.

The work discussed throughout the remaining chapters is motivated by the stream-disk interaction once the disk has been established. The supersonic gas stream will continue to leave L_1 and follow the same ballistic trajectory until it strikes the outer regions of the disk. This produces a localized shock-heated area that may radiate as much or more energy at optical wavelengths as the WD, secondary, and disk combined [90]. The resulting emission feature is commonly referred to as the *hot spot* or *bright spot*.

1.1.1 Observational data

Eclipsing systems, where the observer's line of sight is along the plane of the disk, offer the best opportunity to understand CVs and hot spots. The time at which a feature is eclipsed gives information about its location and how bright it is. Early observations of CVs in the 1950's showed evidence for the existence of some type of bright spot with orbital humps, where additional light from a brighter spot is on the side of the disk facing the observer. Later observations in the emission line spectrum hinted further that this stemmed from the disk-stream interaction. Viewing the accretion disk edge-on, recorded spectra show very strong, double H emission lines

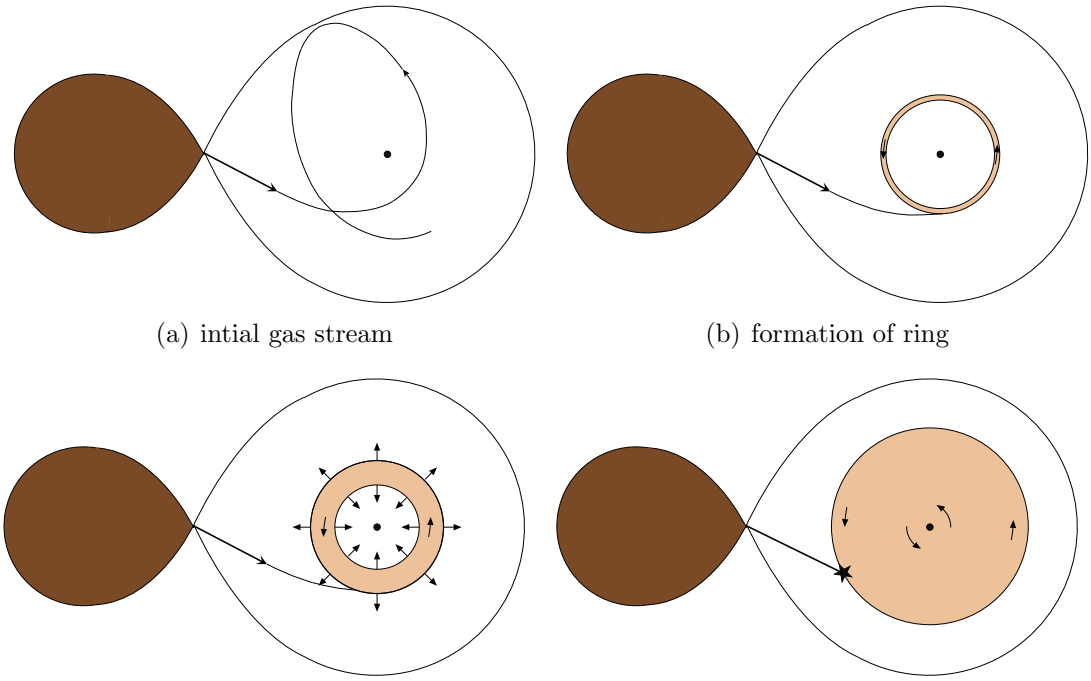

(a) intial gas stream (b) formation of ring

(c) ring spreading (d) disk and *hot spot* are formed

Figure 1.2: The formation of the accretion disk in a semi-detached binary in the orbital plane. (a) The initial trajectory of a gas stream emanating from the companion (brown, left). The WD (dot) is deep in its Roche Lobe (outer line, right). The stream is diverted around the WD and collides with itself. (b) The stream eventually settles into the lowest energy orbit, i.e. circular orbit. (c) While the stream continues to add material, the ring spreads into a thin disk until tidal interactions limit its growth. (d) The *hot spot* is distinguishable in a steady accretion disk.

that are stationary and believed to be produced in the disk. This would be expected as the gas in one half of the disk is moving towards the observer, such that its emission is blue-shifted, while the gas in the other half is moving away and thus its emission is red-shifted. On top of these, however, there is a weak H emission line that varies in radial velocity and forms an "s-wave" between the stationary lines [45, 46]. Figure 1.3 shows a series of spectra taken over an orbital cycle and plotted in sequence, revealing the sinusoidal pattern that gives the s-wave its the name. This feature is due to the Doppler shifting of the bright spot emission as it orbits with the disk. The fact that the s-wave component is fairly sharp compared to the emission line's total width indicates that it originates in a relatively small region of higher temperature [56].

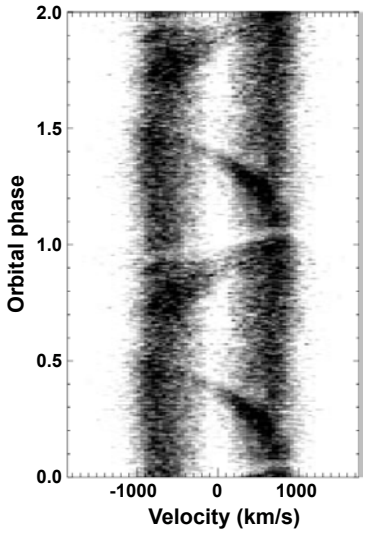

Figure 1.3: Hα spectra of WZ Sge [84]. The line profile at each phase is displayed as a greyscale, with the darker coloring indicating greater intensity. The data shows the double peaks (darkest vertical bands) characteristic of an accretion disk, with an S-wave running from side to side over the orbit.

Furthermore, particular CV data of s-wave amplitude and phase [47] suggests that the velocity vector of the emitting atoms is either nearly identical to incoming gas stream near the point of collision with the disk or that it shares the rotational velocity of disk and the emitting atoms are located on the outer parts of the disk. These two scenarios differ by how or where the stream material interacts with disk, suggesting that the s-wave emission can originate in either (i) stream flow above and below the disk or (ii) a collided flow bulge at the outer disk edge [80]. It should also be noted that different eclipse data further suggests the occurrence of both of these situations: [84, 41, 81, 85].

1.1.2 Astrophysical simulations

The theory of isolated aspects of the CV system, including the gas outflow and accretion disk formation, are well accepted. On the other hand, there is much less certainty about the stream-disk impact region. While the stream will necessarily undergo a shock transition in its interaction with the disk material, the collision region

has many ambiguities as a radiation hydrodynamic system. To the knowledge of this author, preliminary attempts at three-dimensional pseudo particle code and two-dimensional hydrodynamic modeling of the stream-disk impact have been performed only up through the early 2000s: [57, 73, 72, 20, 43, 53, 54, 3, 42, 7]. Collectively they offer four important complications in the interaction of the stream and disk [56]:

- two shocks may form such that the stream material passes through one and the disk material passes through the other. These shocks form a 'V', bounding a region of converged downstream flow with the potential for shear instabilities to grow;

- the denser core of the stream can penetrate into the edge of the disk releasing its kinetic energy at optical depths greater than one, thus locally heating the rim, increasing its scale height and causing a bulge that runs around the edge of the disk for typically half of the perimeter;

- if the impact region is optically thick so that the energy of impact is not quickly radiated, then part of the stream bounces off the disk and is sprayed into the Roche lobe of the WD;

- part of the stream can flow over the rim of the disk and continue approximately along the single particle trajectory over the face of the disk until it impacts the disk at a different radius, also susceptible to the possibly of shear instabilities.

The question of whether the accreting material penetrates, flows alongside, or is reflected from the accretion disk is an open one with astronomical data supporting each case, as discussed above. The generation of a turbulent region in stream penetration has also been suggested as the cause for rapid photometric variations, known as *flickering* [16]. Each one of these interaction outcomes has been proposed based on the radiative cooling properties of the system. However, most of the cited

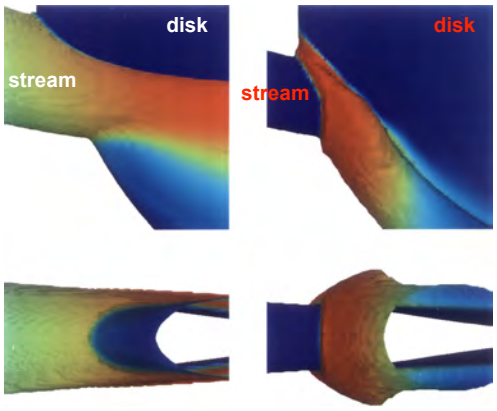

Figure 1.4: Hydrodynamic simulations of the interaction of the stream with the accretion disk [3]. The left panels show isodensity surfaces for an isothermal calculation, plotted at a density that is 10^{-3} of the central disk density (or 1/10 of the central stream density). The colors represent the radial velocities on this surface. The right panels show results for an adiabatic equation of state. Now the isodensity surface is plotted at $10^{-2.75}$ of the central disk density, and the colors represent log c_s on that surface. The upper panels show the top view, with the stream flowing left to right and the disk flowing downward; the lower panels show side views in which the disk material is moving out of the plane of the paper.

computational treatments of the collision region did not include radiation and have been purely hydrodynamic. In the publications [3] and [73] showing 3D and 2D simulations, respectively, the authors attempt to show the extremes of possible behavior (i.e. efficient radiative cooling and no radiative cooling) by using isothermal and adiabatic equations of state (EOS). Figure 1.4 illustrates the primary differences between the EOS radiation treatment in the 3D runs as well as the listed interactions above. Qualitatively, the structure in the flow is distinctly different when comparing their adiabatic and the isothermal calculations. The left two images represent efficient radiative cooling, where the stream is overflowing the disk almost freely, with modest deflection of the edge facing the disk material. In the right panels, the hot, shock-heated gas expands in all directions and disrupts what could have been a coherent overflowing stream. It is evident in the disk midplane that there is "splashing" of hot material downstream of the impact point.

The authors of [3] go further to suggest that a varying optical thickness at the collision region may result from the accretion rate (or mass flow) in the system. The radiation emitted as the shocked stream gas cools must escape through the hot ($\sim 10^6$ K) shocked layer and the relatively cool ($\sim 10^4$ K) inflowing stream material. The opacity of the cooler stream dominated by H^- scattering is approximated by $\kappa = \kappa_o \rho_s^{\frac{1}{3}} T^{10}$ in units of cm^2 g^{-1} with constant $\kappa_o = 10^{-36}$, stream density ρ_s, and temperature T [5]. The optical depth of a column density ($\rho_{so} H_s$) for escape of the hot spot radiation is then given by:

$$\tau = \frac{\kappa \dot{M}}{\pi H_s v_s}, \tag{1.1}$$

where H_s is the scale height of the stream, v_s is stream velocity at impact point, and $\dot{M}$ is the mass flow in units of $M_\odot yr^{-1}$. Setting $\tau = 1$, one can solve for a critical $\dot{M}$ that can define the boundary in optical depth regimes. Using estimated numerical values (from [60, 76]), $\dot{M}_{crit}$ can be approximated at 10^{-9} $M_\odot yr^{-1}$. For accretion rates below this value, cooling should be efficient; above it, the radiation will be trapped by the inflowing stream gas and the initial cooling of the hot spot region will occur via adiabatic expansion. While this analysis is greatly simplified and not a substitute for proper radiative transfer calculation of the impact, it suggests that the hotspot region in low accretion rate cataclysmic variables might well be capable of cooling efficiently, whereas nova-like variables and supersoft x-ray sources with accretion rates much larger than $\dot{M}_{crit}$ are almost certainly unable to do so.

1.2 Introduction to laboratory astrophysics

Laboratory astrophysics is a subset of the high-energy-density (HED) physics field [28]. The subject matter aims to bridge the gap between astrophysical observations and theoretical models with experimental conditions that are equivalent, in a rigor-

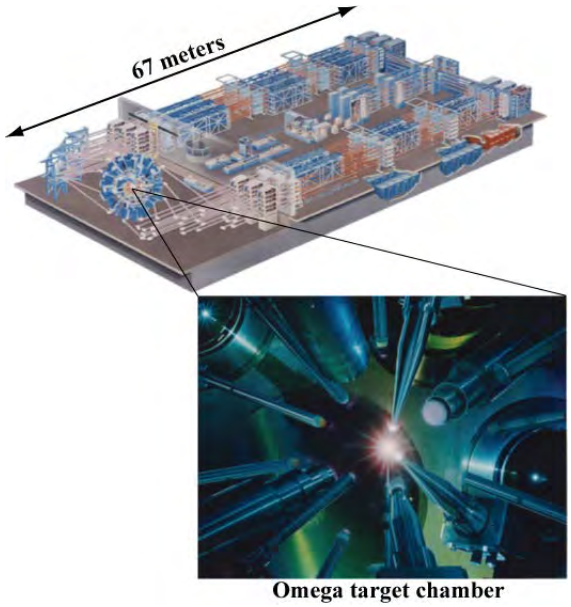

Figure 1.5: The Omega laser system is shown on the top. The long rows of equipment on the right side of the image around the perimeter are the final stages of the Nd:glass amplifiers. 60 total beams can be focused into the spherical, 3.3 m diameter target chamber, shown at the left end of the image. The bottom image shows the center of the target chamber during an experiment. The glowing target is located at the center of the picture having been irradiated and is surrounded by diagnostics.

ously scaled sense, to those in large astrophysical systems. While there are different types of HED facilities, the work detailed in this thesis is done solely with high-intensity lasers. Modern intense lasers can deposit kJs of energy in submillimeter-scale volumes. As shown in Ryutov et al. [74], equations describing the hydrodynamic evolution of an astrophysical system can be scaled in space and time if radiation flux, viscosity, heat flow can be neglected. Therefore, studying a specific phase or part of an astrophysical object or event can be possible on smaller length scales and shorter time scales if other factors are scaled as well. These types of experiments have been done successfully many times [49, 71, 30] at the Omega-60 laser facility in the Laboratory for Laser Energetics (LLE) in Rochester, NY [83] shown in Figure 1.5. However, when radiation flux becomes important, this scaling becomes more complicated. In such systems, comparison of the optical depth structure reveals that the systems might be

described by similar physics. If the optical depth profile of two systems is similar, radiation should have similar effects in each. In this same vein, it should be noted that although the exact astrophysical environment can not be reproduced in the lab, astrophysical modelers remain eager for radiation hydrodynamic experimental data like that done on the Omega laser to use for benchmarking code. Any simulation code that cannot calculate the experimental interaction correctly based on input data of the flows will not correctly calculate the astrophysical case.

One long-researched radiative hydrodynamic system is that of the radiative shock. Since the 1980s, high-power lasers have been used to create strong shock waves and drive them to the speeds and conditions necessary for radiative cooling to play a significant role in their structure and evolution [12, 10, 69, 44]. As is the case with those cited, such laboratory experiments often involve a gas-filled tube driven by a piston onto which the laser imparts 10's of Mbar of ablation pressure. This process causes a shock to be launched into the gas, moving in the laboratory frame. Radiative shock experiments of this design have reached velocities upwards of 130 km/s with the Omega laser and have several years of history before the present work [70, 21].

While radiative shocks are ubiquitous in space, one astrophysical connection to this work that has been explored is supernova remnants. Observed structure in old supernova remnants suggest that radiatively-induced collapse of material into a thin shell occurs. In turn, this structure could be susceptible to thin-shell instabilities [89]. More recent work by Doss et al discusses the necessary parameters for scaling the driven radiative shock experiments to the astrophysical instability [24]. Certain dimensionless variables can be evaluated from experimentally available data both for the decelerating, dense, post-shock layer in the radiative shock experiment and for astrophysical systems with spherically diverging shocks. This has the potential to better explain the origin of clumpy, irregular structure in supernova remnants.

1.3 Scaling experiments to astrophysical regimes

In the case of the driven radiative shock experiments above, the need for a gas-filled shock tube introduces structure and limitations to how shocked material evolves due to target wall effects [26]. The new experiments detailed in this thesis propose a radiative shock system where a supersonic stream moves into the shock front in the laboratory frame. It can be called a "reverse shock" system because the shock wave is created when the freely flowing, supersonic plasma is impeded. In this experiment, a static foil is used. This can be done without confining the system in a shock tube which will be shown in Chapter III. In consideration of the "hot spot" geometry, the experiment involves similar basic components: a supersonic plasma flow and an obstacle. In order to draw physical connections to the CV, however, further evaluation of the system is explored here.

It should be noted that the comparison of interest is with in a long-period CV system in quiescence where a steady accretion disk is inferred. The undisturbed velocities of the stream and disk's rim are chosen following the restricted 3-body problem calculations by [79] and [67]. In the reference frame co-rotating with the binary, the velocity of the disk rim, v_d, is 300 km/s. Likewise the stream flows at a velocity, v_s, of 300 km/s prior to it colliding with the disk at an impact angle β, often taken to be 60 degrees. Following [58], the density of the stream, ρ_s is a Gaussian function of the distance r from a symmetry axis:

$$\rho_s = \rho_{sc} \exp^{-r^2/r_s^2}, \tag{1.2}$$

where r_s is the effective half-width of the stream (so, $2r_s = h_s$, scale height of the stream) and ρ_{sc} is the maximum density of the stream. The edge of the disk is defined in a similar way. Prior to impact with the stream, the disk is taken to be in hydrostatic equilibrium in the vertical direction, which together with an isothermal

vertical structure corresponds to a Gaussian density profile with scale height h_d. At the disk edge, h_s is typically bigger than h_d by a factor of 2-3 [59]. The stream gas is taken to have the same temperature as the outer edge of the disk. Slow inflow through a viscous disk implies that $\rho_d \gg \rho_{sc}$. A steady-state disk described by [75] suggests $\rho_d \ / \ \rho_s \sim 100$.

The main hydrodynamic parameters of the CV system are the Mach number of the flow, the ratio of accretion disk to stream density and the ratio of disk to stream scale height. Considering these dimensionless numbers provides some framework in designing a laboratory experiment. As mentioned above, the addition of radiation importance makes a well-scaled experiment very difficult. Instead one can calculate useful dimensionless numbers relevant to radiative systems to compare them. This work considers two other sets of parameters: radiative properties and timescales.

The first, designated R_{rad}, is the ratio of material energy flux going into the shock front to the energy flux lost to radiation in an optically thick system at the immediate post-shock temperature. Similar to the Boltzmann number [64], this ratio offers a measure of the relative importance between radiative and material energy transport in the radiating system. Because the increase of material enthalpy flux is balanced directly by the decrease in kinetic energy flux across the discontinuity, R_{rad} can be defined as

$$R_{rad} = \frac{\frac{1}{2}\rho_o u_{flow}^3}{\sigma T_{ps}^4}, \tag{1.3}$$

where ρ_o and u_{flow} are the density and velocity of the incoming flow, respectively, σ is the Stefan-Boltzmann constant, and T_{ps} is the post-shock temperature. If R_{rad} falls below 1, i.e. the continuum emission exceeds the material energy flux, the optically thick system would be violating energy balance, and so the structure of the shocked layer must change to prevent this. Therefore, when radiative energy transport is dominant one will have $R_{rad} \ll 1$. The second parameter, known as the cooling parameter χ, provides a measure of the qualitative hydrodynamics of the flow. In

Table 1.1: Main dimensionless numbers characterizing the hot spot regions and the laboratory plasma. The indices s, d and ps correspond to stream, disk and post-shocked plasma.

Plasma parameters	Hot spot	Laboratory plasma
T_{ps} (eV)	100	200
ρ_s (g cm^{-3})	5×10^{-11}	10^{-2}
u_s (km s^{-1})	300	150
$\eta_o = \rho_s/\rho_d$	10^{-2}	10^{-2}
h_s/h_d	2	2
M_s	30	10
R_{rad}	6.5×10^{-7}	8.5×10^{-3}
χ	0.1	0.8

the most general form, it is the ratio of cooling time to the dynamical time. The determination of this ratio varies for the CV and the laboratory. Following [8], a simple description of the hot spot cooling supports

$$\chi_{astro} = \frac{t_{cooling}}{t_{dynamical}} \approx \frac{k_B T_{ps}^3}{n\Lambda(T_{ps})} \times \Omega, \tag{1.4}$$

where k_B is the Boltzmann constant, n is the number density of electrons, and Λ is the cooling function which is taken from [19] for this approximation. Ω is the Keplerian angular velocity, which approximates the dynamical time at the edge of the disk by $\sim \Omega^{-1}$ [s].

Following [31], the laboratory system is described by

$$\chi_{expt} = \frac{t_{cooling}}{t_{dynamical}} \approx \frac{p_{shock}}{(\gamma - 1)\Lambda} \times \frac{u_{flow}}{w_{shock}}, \tag{1.5}$$

where $\Lambda \approx \sigma T_{ps}^4 \kappa_p$ with κ_p is the Planck mean opacity in Sn, and w_{shock} is the shock width. The experiment dynamical time is the ratio of the shock width to the flow velocity, u_{flow}.

Table 1.1 shows the comparison of these two possible systems. Experimental

values used in Table 1.1 are taken from both simulation and laboratory data. The experimental design made a priority to conserve both the density ratio between the supersonic stream and the "disk", as well as the ratio of scale heights. With this and Mach numbers $\gg 1$, it should be producing similar impact physics with strong shocks. Furthermore, if $R_{rad} \ll 1$, both shocks would be strongly radiating, a distinction needed without the magnitudes being the same. Finally, and perhaps most importantly, if one could produce an experiment with a comparable (invariant) χ to the CV system, that would suggest it can conceivably maintain the same balance between the radiation and hydrodynamic effects in the systems. Note that the existing experiment cools more strongly than the CV referenced in the table, so that by changing material to decrease the rate of radiative cooling, one should be able to make the experimental value of χ closer to the astrophysical one. Overall, Table 1.1 shows promising results for correlations between the systems.

1.4 Outline of future chapters

The previous sections outline the non-magnetic cataclysmic variable system which motivates the subsequent laboratory work. Much of this motivation and the scaling analysis are published in the Astrophysical Journal Letters, Volume 762, Issue 1, entitled, "Reverse Radiation Shock Laser Experiments Relevant to Accreting Stream–Disk Impact in Interacting Binaries." The majority of the remaining text deals with the implementation of the experiments, diagnosing and understanding the reverse shocks in the laboratory.

Chapter II first reviews the physics of radiative reverse shocks. This includes output from the 1D HYADES code that simulates the basic mechanism for the experiment. As discussed in the scaling above, the radiative shocks considered here are in the so-called "flux-dominated" regime where the flux of radiation energy is non-negligible when compared with the flux of material energy. The relations for

the state variables in terms of the "downstream" (i.e. shocked) region are derived using a treatment of the fluid dynamics and the radiative transfer. Following the predicted experimental system, the optical depth profile is such that radiative energy from the downstream state with a large optical depth does not return to the shock. In other words, the shocked region is optically thick while the "upstream" (i.e. incoming unshocked flow) is optically thin, allowing radiative cooling to occur. Given this profile, the downstream pressure and temperature as well as the shock velocity and compression ratio, are plotted against a shock strength parameter.

Chapter III encompasses the experiment design and the process of collecting data. The primary aspects of creating a supersonic flow, and then the shock, involve a total of 3 material foils. However, the process of mounting these foils into a vacuum chamber for the laser ablation involves much more superstructure. This chapter discusses the evolution of target structure over a few iterations of the experiment. In order to image the shock physics, secondary targets are added in the chamber serving as x-ray sources. Chapter III includes part of the manuscript that discusses these x-ray sources and the bremsstrahlung spectrum that is observed from them which was published in Review of Scientific Instruments, Volume 83, Issue 10, with the title, "An evaluation of high energy bremsstrahlung background in point-projection x-ray radiography experiments." The chapter concludes with an overview of other secondary diagnostics that were implemented on the experiments.

Chapter IV discusses experimental data from normal-incidence reverse shock waves. It presents two methods for extracting compression ratios from x-ray data images. The first concerns basic geometric measurements, while the second examines mass density profiles. The uncertainty in the latter is discussed in conjunction with known experimental shortcomings. Towards the end of the chapter, the profiles are compared to some computational work done with 2D CRASH [87] simulations. Some of this analysis is part of the manuscript "Radiative reverse shock laser experiments rel-

evant to accretion processes in cataclysmic variables" which was published in Physics of Plasmas, Volume 20, Issue 5. Other findings from this radiography analysis are further discussed in context of or with comparison to the secondary diagnostic data.

Chapter V introduces the oblique geometry experiment that was devised for the purpose of moving closer to the CV system. Initial attempts had design flaws that affected the reverse shock's evolution. These data are shown and considered briefly. While the most recent target design also had flaws, it produced some intriguing results. A discussion is presented in this chapter as an opening for more experimental data and simulation with regard to Kelvin-Helmholtz instability. 2D CRASH simulations suggest that vortex growth can occur in the post-shock flow of an oblique radiative reverse shock. Ongoing analysis has moved this conversation in many directions, however, the chapter concludes with some findings drawn from recent supplemental runs. The work done with regard to this experimental data and simulation is being collected for another manuscript.

Chapter VI concludes this thesis with a summary of personal contributions and thesis contents. It also presents ideas for future directions and experiments, which aim to further this work. This thesis also includes several appendices. The target specifications for each design attempted in a campaign are shown in Appendix A, including fabrication tolerances within which all targets are individually characterized prior to the experiment. An additional experiment was completed in conjunction with this work to better characterize high-energy background from the x-ray sources created in the laboratory for diagnostic purposes. The targets used in this campaign are also shown in Appendix A. Appendix B presents a catalog of some radiographs from each campaign, not presented in the main text, that show evidence of unwanted signal effecting either the experiment or the diagnosing of it. One example easily seen is the film background exposure that occurs from unshielded emission in the chamber. Finally, Appendix C provides the Omega laser facility details needed to

execute each experiment, including the laser conditions and diagnostic specifications. These documents give the reader an overview of the facility's setup and requirements for running the reverse shock campaigns.

CHAPTER II

Normal Radiative Reverse Shock Theory

The first attempts at creating this reverse radiative shock in the laboratory were a proof-of-principle experiment. Simulations of the reverse shock experimental system were performed using the HYADES [55] code, a one-dimensional, Lagrangian, three-temperature, single-fluid code with a multigroup flux-limited diffusion radiative transport model. Although the radiation transport model is not as accurate as full treatment of the radiative transfer equation and two-dimensional effects could play an important role in the experiments at the collision region, HYADES is a useful tool for experimental scoping. In a Lagrangian description the mesh moves with the material so that each element of mass in the mesh is conserved over time. The Euler equations are used for the three-temperature, single-fluid description. However, in the momentum equation, the pressure is determined by summing the contributions from the electrons, ions, and radiation, while the energy equation is replaced by one equation for each species. Multigroup radiation allows the user to assign energies to many different photon groups and then an average opacity is calculated for each of those groups. A simulation of the reverse shock experiment can be seen in Figure 2.1. HYADES predicts the creation of a very fast moving flow via laser ablation that, in turn, creates a strongly radiating shock when it is impeded. In the simulation, the laser had propagated from the left and the flow expands to the right. Around 21 ns

after the laser pulse initiates the simulation, the incident flow collides with the 100 μm Al layer and both a reverse shock and transmitted shock form, which can be seen in the density curve (black). As material moves through the shock, it undergoes a quick jump in pressure, density, and ion temperature. This happens physically over the course of a few ion-ion mean free paths and is not well resolved in the simulation. Most of the energy goes into initially heating the much heavier ions, however, electrons gain energy from collisions with the warm ions causing the ions to lose energy. In the evolution of this shock system, there is a decrease in ion temperature that is proportional to the increase in electron temperature, and as electrons get warmer, they are capable of radiating away a more significant fraction of the energy in the system [28]. Given this, a characteristic spike in ion temperature across the shock verifies a radiative phase to the shock. In Figure 2.1, this can be seen in the ion temperature profile (blue curve) at Z = 0.39 mm, signifying that the code approximates a radiative phase to the reverse shock. As the system cools, conservation equations must still hold, and other quantities must adjust in response to the lost energy. This chapter reviews the system adjustments analytically.

2.1 Reverse radiative shock

The impact of a high speed gas stream on an infinite plane fixed obstacle is considered in the quasi-steady-state formulation. In this case the reverse shock wave forms in the rebounding direction and propagates counter to the free stream. This 1D formulation aims to represent the shock wave processes in the HYADES simulations and thus the laboratory experiment. Consideration of radiation flux at the system boundaries yields information about the structure of a radiative shock transition and the extent of its cooling layer. In addition to the energy losses from the shock front, the reflection of radiation from the obstacle in the reverse shock case can significantly affect the energy balance. Figure 2.2 outlines the system. The “upstream” region

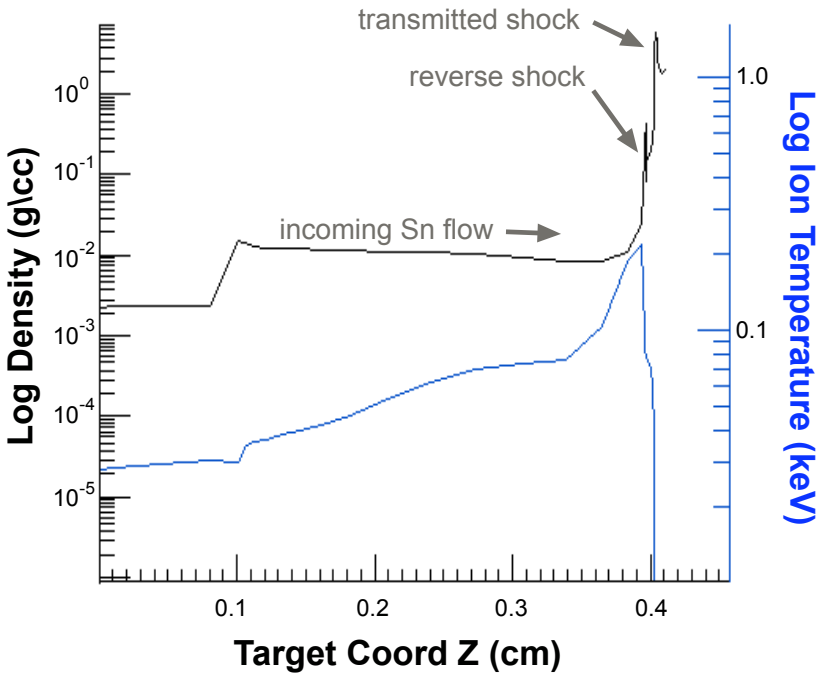

Figure 2.1: 1D HYADES simulation of reverse shock experiment at t = 22 ns, right after the shock has formed. The laser is incident from the left at t = 0, creating a Sn flow that is launched into an Al wall Z = 0.4 cm.

refers to the incoming, fast moving flow that is the pre-shock state. It has constant values for the radiation flux as well as density and temperature. The density jump of the shock front is between the cooling layer and the upstream region. The cooling layer contains the maximum temperature in the system and that temperature cools via radiation until the final downstream, or post-shock, state. In the following evaluation, the upstream region is assumed to be optically transparent for radiation from the front. Ablation of the obstacle initiated by heat fluxes from the internal hot shocked zone is neglected. Although it is shown in Figure 2.2, this is meant to represent a more accurate downstream boundary. The effect of emission and reflectivity of obstacle on the parameters behind the shock wave is analyzed. Differing from previous analysis [62], the shock wave velocity is not assumed to be a given parameter but represents an unknown quantity determined, as other quantities, by the characteristics of the stream and the condition of its stagnation against the obstacle. Thus, shock-frame

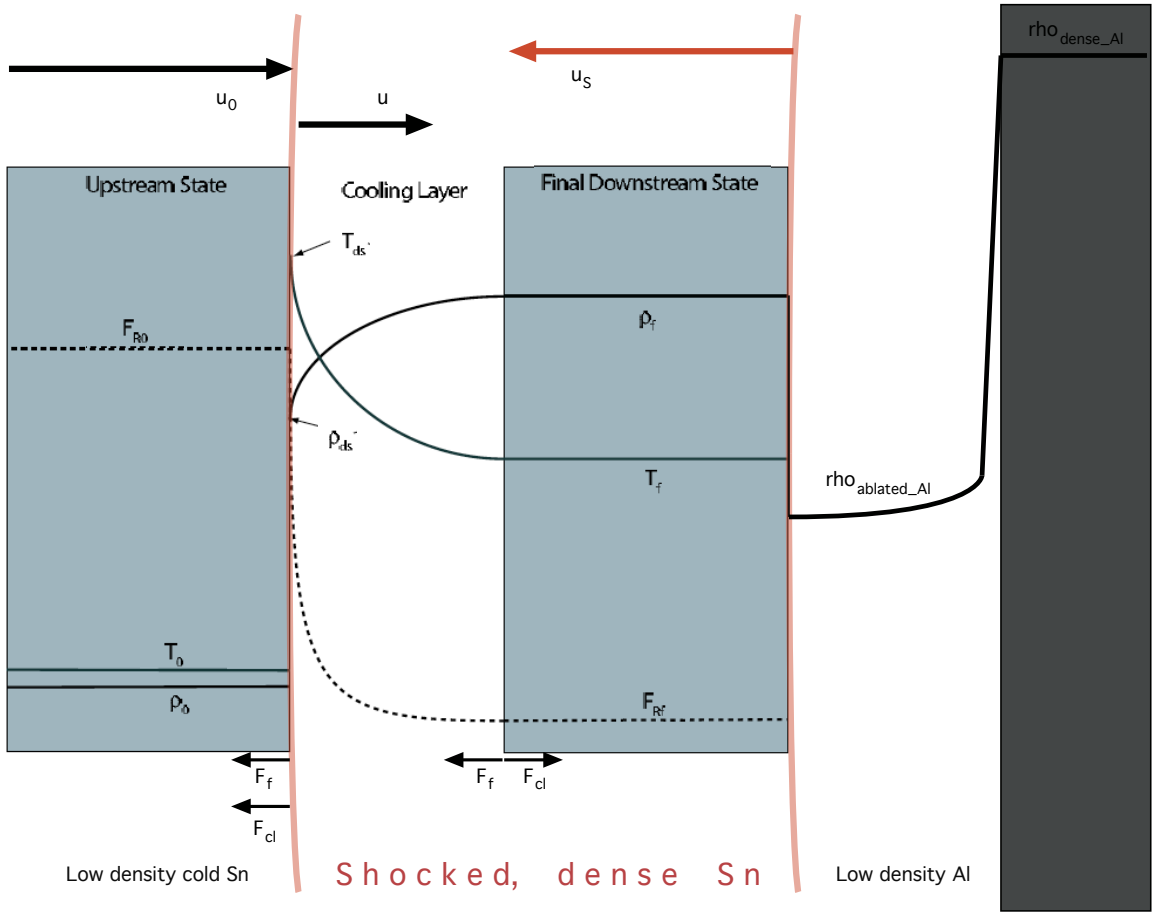

Figure 2.2: Cartoon of the reverse shock model, where the shock (red boundary) is moving right to left with speed u_s. The density jump of the shock front is at the boundary between the upstream state and the cooling layer. Beyond the downstream state, there is a layer of low density Al between the shock and the Al obstacle. Note that in this model the radiation flux is constant in the upstream portion of the system.

velocities are defined such that

$$U_1 = u_0 + u_s \tag{2.1}$$

$$U = u + u_s \tag{2.2}$$

where u_0 is the stream velocity moving into the shock, u_s is the velocity of the reverse shock, and u is the velocity of shocked material all in the laboratory frame. Here $u_s < 0$. The following relations hold for the flux of mass, momentum, and energy throughout the shock profile:

Conservation of mass flux:

$$\rho_1 U_1 = \rho U$$

Conservation of momentum flux:

$$P_1 + \rho_1 U_1^2 = P + \rho U^2 \tag{2.3}$$

Conservation of energy flux:

$$\left(\frac{\gamma_1}{(\gamma_1 - 1)}\frac{P_1}{\rho_1} + \frac{U_1^2}{2}\right)\rho_1 U_1 + F_1 = \left(\frac{\gamma}{(\gamma - 1)}\frac{P}{\rho} + \frac{U^2}{2}\right)\rho U + F$$

where the subscript "1" corresponds to parameters of the upstream state. Introducing normalized parameters

$$\rho_N = \frac{\rho}{\rho_1}, \tag{2.4}$$

$$u_N = \frac{u}{u_0}, \tag{2.5}$$

$$P_N = \frac{P}{\rho_1 u_0^2}, \tag{2.6}$$

$$F_N = \frac{F}{\frac{1}{2}\rho_1 u_0^3} \tag{2.7}$$

to get a non-dimensional form and inserting equations (2.1) and (2.2), (2.3) can be combined into one equation, such that

$$\begin{aligned} 1 + u_{sN} = \rho_N(u_N + u_{sN}) &= \left(\frac{P_N - P_{1N}}{1 - \frac{1}{\rho_N}}\right)^{1/2} \\ (1 + u_{sN})\left[\frac{2\gamma_1 P_{1N}}{(\gamma_1 - 1)} - \frac{2\gamma P_N}{(\gamma - 1)}\frac{1}{\rho_N} + (P_N - P_{1N})\left(1 + \frac{1}{\rho_N}\right)\right] &= F_N - F_{1N}. \end{aligned} \tag{2.8}$$

The final condition, mentioned above, is the idea that there is stagnation of shocked material on the obstacle. This corresponds to $u = 0$. Subscript "2" designates the corresponding parameters at this point, i.e. on the obstacle. Using equation (2.3), now

$$1 + u_{sN} = \rho_{2N} u_{sN} \qquad \text{or} \quad u_{sN} = \frac{1}{\rho_{2N} - 1} \qquad \text{and} \tag{2.9}$$

$$1 + u_{sN} = P_{2N} - P_{1N} \qquad \text{or} \quad u_{sN} = P_{2N} - P_{1N} - 1 \tag{2.10}$$

which by equating, gives

$$\frac{1}{\rho_{2N}} = 1 - \frac{1}{P_2 - P_1}. \tag{2.11}$$

Similarly to get one equation, plugging equations (2.10) and (2.11) into equation (2.8) finds

$$\begin{aligned} \frac{-P_{1N}^2(\gamma_2 - 1)}{(\gamma_1 - 1)} + P_{1N}P_{2N} + \frac{P_{1N}P_{2N}(\gamma_2 - 1)}{(\gamma_1 - 1)} + \frac{P_{1N}(\gamma_2 - 1)}{2} \\ - P_{2N}^2 + \frac{P_{2N}(\gamma_2 + 1)}{2} = \frac{(\gamma_2 - 1)}{2}(F_{2N} - F_{1N}). \end{aligned} \tag{2.12}$$

Here, the quantity $(F_{2N} - F_{1N})$ determines the dimensionless radiation loss or, in other terms, the conversion ratio of the incoming flow's kinetic energy to the total radiation energy from the shock front and to the obstacle. For simplicity, assume

that $P_{1N} \ll 1$, which is reasonable for the system of interest. This allows

$$u_{sN} = P_{2N} - P_{1N} - 1 \quad \rightarrow \quad u_{sN} = P_{2N} - 1, \tag{2.13}$$

$$u_N = 1 - \frac{P_N}{P_{2N}}, \tag{2.14}$$

$$\text{and} \quad \frac{1}{\rho_N} = 1 - \frac{P_N}{P_{2N}^2}. \tag{2.15}$$

Furthermore, (2.12) without P_{1N} becomes

$$P_N - \frac{P_N^2}{P_{2N}^2}\frac{(\gamma+1)}{2} + \frac{(\gamma-1)}{2P_{2N}}\Delta F_N = 0, \tag{2.16}$$

where $\Delta F = F_N$ - F_{1N}. Together, equations (2.13)-(2.16) express the parameters at an arbitrary point of the shock wave in terms of the pressure on the obstacle (subscript "2"). In other words, they determine the shock wave structure. One can solve (2.16) for P_N to get

$$P_N = \frac{P_{2N}^2}{(\gamma+1)}\left(1 \pm \sqrt{1 + \frac{\Delta F(\gamma^2-1)}{P_{2N}^3}}\right). \tag{2.17}$$

In order to use equation 2.17 to derive the relation between the temperature and the increase in the radiative flux ΔF at a given point, the equation of state is introduced:

$$T = \frac{Am_p}{(Z+1)k_B}\frac{P}{\rho}, \qquad \text{with} \quad R = \frac{(Z+1)k_B}{Am_p}, \tag{2.18}$$

where Z is the average ionization state, k_B is the Boltzmann constant, A is the atomic weight of the material, and m_p is the mass of a proton. Dividing by $T_0 = \sqrt[4]{\frac{F_0}{\sigma}}$ and recalling that $F_0 = \frac{1}{2}\rho_1 u_0^3$, a normalized expression for temperature can be expressed by

$$T_N = \frac{P_N}{\rho_N}\left(\frac{\rho_1 R^4}{2\sigma u_0^5}\right)^{-\frac{1}{4}}. \tag{2.19}$$

Previous work done by Drake [68, 29] for the theory of optically thick radiating shocks

introduces the parameter $Q = \frac{2\sigma u_0^5}{\rho_1 R^4}$, as the dimensionless shock strength. This gives

$$T_N = \sqrt[4]{Q}\frac{P_N}{\rho_N}. \tag{2.20}$$

Inserting the expression for $\frac{1}{\rho_N}$ from (2.15), (2.20) becomes

$$T_N \;\; = \sqrt[4]{Q}\, P_N \left(1 - \tfrac{P_N}{P_{2N}^2}\right) \;\; = \sqrt[4]{Q}\left(P_N - \frac{P_N^2}{P_{2N}^2}\right) \tag{2.21}$$

which expresses temperature at an arbitrary point of the shock wave in terms of the pressure on the obstacle. Now substituting the solution for P_N, equation (2.17), into T_N, equation (2.21), the relation between the temperature and the increase in the radiant flux ΔF at a given point is

$$T_N = \sqrt[4]{Q}P_{2N}^2\frac{(\gamma-1)}{(\gamma+1)^2}\left(1 - \frac{(\gamma+1)\Delta F}{P_{2N}^3} + \sqrt{1 + \frac{\Delta F(\gamma^2-1)}{P_{2N}^3}}\right). \tag{2.22}$$

Similarly this set of equations can be found for the stagnation point and are:

$$u_{2N} = 0 \tag{2.23}$$

$$\frac{1}{\rho_{2N}} = 1 - \frac{1}{P_2} \tag{2.24}$$

$$P_{2N}^2 - \frac{P_{2N}(\gamma_2+1)}{2} + \frac{(\gamma_2-1)}{2}\Delta F_{2N} = 0 \tag{2.25}$$

$$T_N = \sqrt[4]{Q}(P_{2N} - 1). \tag{2.26}$$

With the exception of an expression for F, equations (2.14)-(2.16) and (2.22) [and at the stagnation point: equations (2.23)-(2.26)] determine the shock wave dynamics in the quasi-steady-state approximation of the experiment, including not only the initial stage of strong emission ($\Delta F_2 \neq 0$) but also when it is no longer radiative ($\Delta F_2 = 0$). All of the parameters behind the discontinuity are functions of the pressure on

the obstacle, P_{2N}, and depend on the characteristics of the gas stream through P_{2N}. Equations (2.14)-(2.16) and (2.22) show that as the particles are decelerated, the pressure and compression ($\frac{\rho}{\rho_1}$) increases as the temperature decreases. This density effect is what makes it possible to diagnose a radiative shock in the laboratory and is revisited in context of experimental data analysis in Chapter IV.

In order specify the radiative parameters in the shock system, an optically thick shock is considered. This case is of interest since it determines the maximum possible radiation fluxes from the front and to the obstacle. Assuming that the energy lost from the wave front is mainly emitted from material in equilibrium, it is further supposed that the shock layer radiates as the blackbody with the temperature T_p toward the upstream and with the temperature T_2 in the direction of the obstacle, where some part of radiation can be reflected from the obstacle. Then from the above equations, one finds

$$P_{pN} - \frac{P_{pN}^2}{P_{2N}^2}\frac{(\gamma+1)}{2} + \frac{(\gamma-1)}{2P_{2N}}\Delta F_{pN} = 0 \tag{2.27}$$

$$-F_{pN} = \sigma T_{pN}^4 = Q\left(P_{pN} - \frac{P_{pN}^2}{P_{2N}^2}\right)^4 \tag{2.28}$$

$$P_{2N}^2 - \frac{P_{2N}(\gamma_2+1)}{2} + \frac{(\gamma_2-1)}{2}\Delta F_{2N} = 0 \tag{2.29}$$

$$F_2 = (1-\beta)T_{2N}^4 = (1-\beta)Q(P_{2N}-1)^4 \tag{2.30}$$

where β is the radiation reflection coefficient of the obstacle. These equations provide information about the effect of reflection of radiation from the obstacle on the parameters in the shock-compressed zone. In the simplest case, $\beta = 1$ where the total radiation is reflected by the obstacle. From (2.30), it follows that $F_2 = 0$, and $T_p = T_2$. So given the total reflection, in the final downstream state for an optically thick shock the difference between the local radiation flux and the far upstream radiation flux is zero, $\Delta F_2 = \Delta F_p$. With this result, equations (2.27) and (2.29) become equivalent

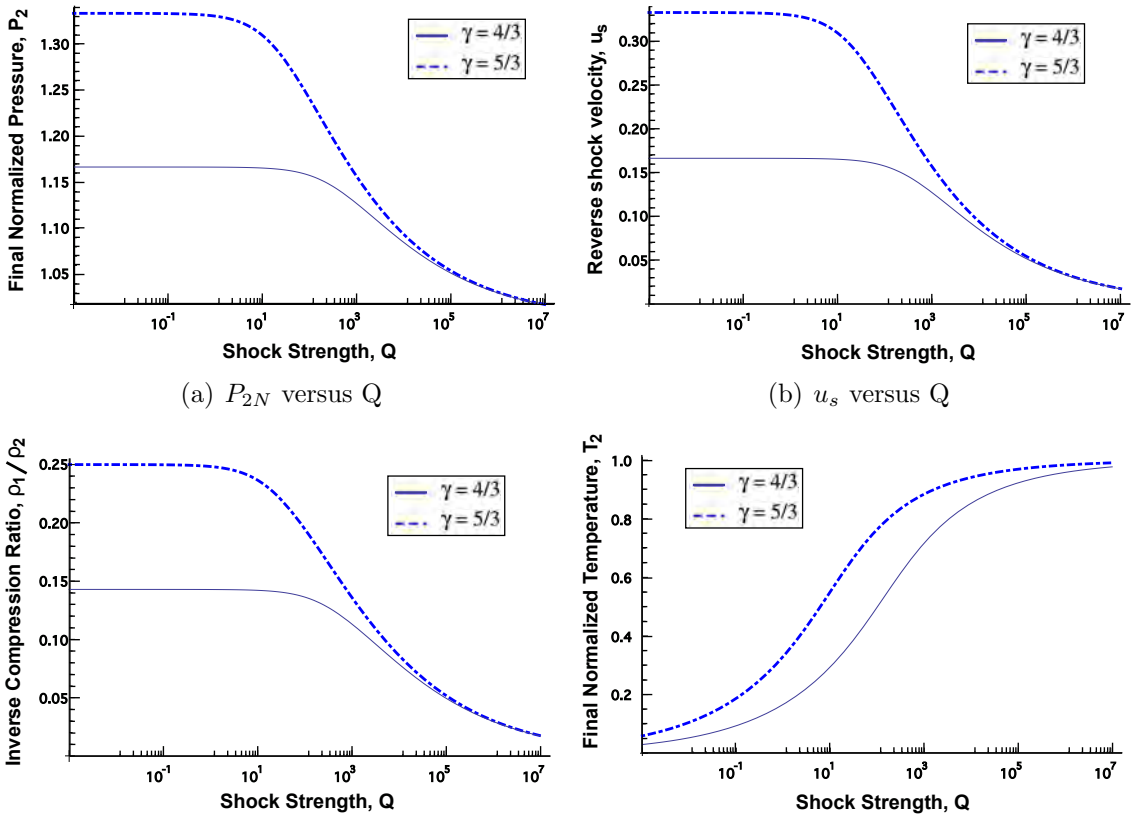

(a) P_{2N} versus Q

(b) u_s versus Q

(c) $\frac{\rho_1}{\rho_2}$ versus Q

(d) T_2 versus Q

Figure 2.3: Parameters of reverse shock system in terms of the dimensionless shock strength Q

to one another and it is found that

$$P_{2N}^2 - \frac{P_{2N}(\gamma_2+1)}{2} + \frac{(\gamma_2-1)}{2}Q(P_{2N}-1)^4 = 0. \tag{2.31}$$

Finally, P_{2N} can be solved in terms of Q. This solution can in turn be used to express each parameter in terms of Q, some of which are plotted in Figure 2.3 for both $\gamma_2 = 4/3$ and $5/3$. Evaluating the normalized parameters in terms of Q shows restrictive limits that correspond to the physical limit that radiation flux from the shock front can not exceed the incoming material (kinetic) energy flux. In the case where Q = 0 (i.e. a strong non-radiative shock), the classical values are found such that $P_{2N} = \frac{\gamma+1}{2}$, $T_2 = 0$, and inverse compression ratio, $\frac{\rho_1}{\rho_2} = \frac{\gamma-1}{\gamma+1}$. Also, shock velocity, $u_s = \frac{\gamma-1}{2}$.

In the limit where Q $\rightarrow \infty$, P_{2N}, $T_2 \rightarrow 1$, and $\frac{\rho_1}{\rho_2}$, $u_s \rightarrow 0$.

In the HYADES simulation shown in Figure 2.1, the initial incoming flow velocity, u_0, is $\sim$ 190 μm/ns with a density of 10^{-2} g/cm^3. This corresponds to a value for Q of roughly 8.2 $\times$ 10^6. The simulation likely predicts higher values than what is occurring in the experiment for both u_0 and ρ_1 due to the single dimensionality. The experimental data discussed in the Chapter IV suggests that Q is closer to 2.5 $\times$ 10^7, where lower density accounts for the increase.

CHAPTER III

Experimental Description

This chapter fully details the experimental design for creating a reverse radiative shock by means of launching a supersonic plasma flow and diagnosing it. The laser-ablated experimental package is referred to as the target. The design of the target had various iterations over the course of this thesis work, some of which will be discussed in this chapter for reasons relevant to the data. Target components are often simulated with the one-dimensional radiation hydrodynamics code HYADES [55] prior to being implemented. A fabrication team [36] at the University of Michigan constructs and characterizes all targets with the use of motorized stages with ~ 25 μm precision. The details of the laser and generation of the flow are also discussed, in context of both simulation and data. The latter half of the chapter also presents the primary means by which data are collected in some detail and concludes with overviews of secondary diagnostics.

3.1 Target

The basic components of the target that produce the reverse shock are shown in Figure 3.1(a). The overall concept is to launch a high-velocity flow of plasma into a static wall. To create the flow, the Omega laser is used to irradiate a thin foil of material, referred to as the drive foil. The large ablation pressure from the laser launches a

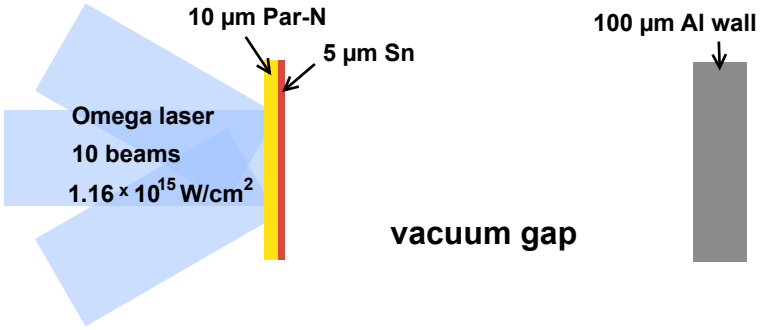

(a) basic components needed for reverse shock system

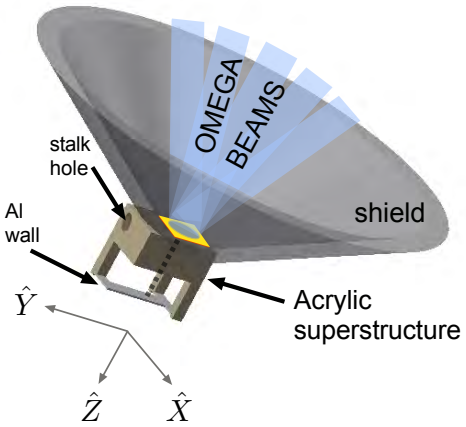

(b) CAD model of full target

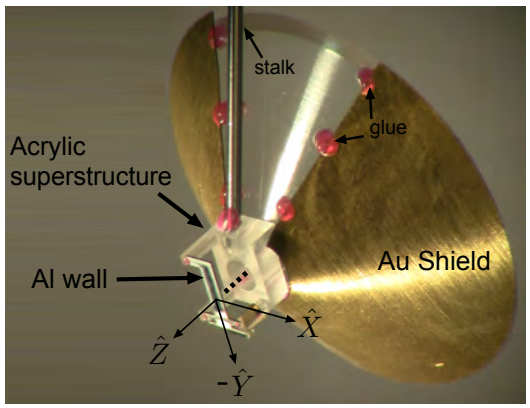

(c) Full scale experimental target

Figure 3.1: (a) Three foils that create the reverse shock. Plastic side of the layered foils is ablated to drive the plasma stream into vacuum and the Al wall causes the shock to form. (b) Full model of the target shows large superstructure onto which the three foils are attached. Once the laser strikes the drive foils, Sn plasma flows down the cylindrical axis (shown by the dotted line) towards the Al obstacle. (c) Here target perspective is such that the laser ablation spot can not be seen. The acrylic face holding the CH/Sn foil is tilted into the page and surrounded by Au conical shielding. The end of the milled cylinder through which the Sn flows can be seen. The pink dots are glue and the vertical rod is the stalk that holds the target.

forward shock into the drive foil, which becomes compressed and ionized. The shock then breaks out of the rear of the Sn into a vacuum gap. Depending on the size of the gap and the laser temporal duration, the compressed material will decompress and increase its spatial extent to varying degrees as it accelerates across the gap. Some distance away, the flow strikes an Al foil and a reverse shock propagates back into the oncoming flow. A CAD model of the full target in Figure 3.1(b) shows how these foils are suspended in the vacuum chamber. The laser-ablated foil is attached to one side of an evacuated 2 mm diameter cylinder. This tube is milled out of a larger acrylic block such that the face on which the CH/Sn foil is glued is normal to the tube axis. The acrylic block is a 4.3 mm $\times$ 3.2 mm $\times$ 2 mm superstructure that has additional extended 2 mm "legs" from three of the corners along the 2 mm height of block. These acrylic extensions provide attachment points for the Al obstacle radially far from the central tube axis and roughly 4 mm down the axis from the drive foil. Therefore the Sn flow, moving along the cylindrical axis, will move across a 4 mm vacuum gap before impacting the Al. This distance was chosen as a compromise between target structure stability and simulation data of flow speed. The area of interaction at the Al occurs within a 2 mm by 1 mm strip of 100 μm thick Al foil that spans the cross-sectional circle. A large conical shield is added around the drive foils to block any emission at the laser spot from reaching some diagnostics.

3.1.1 Evolution of targets

Because this work is the development of a new experimental platform, there were a few other target designs prior to arriving at the model in Figure 3.1(b). Initial designs addressed the concern for enough diagnosable mass. In the interest of containing the plasma flow, a 1 mm long polyimide tube (25 μm wall thickness) was placed at the collision region, such that a >2 mm $\times$ >2 mm $\times$ 100 μm Al obstacle capped it. This "bucket" target can be seen in Figure 3.2(a). Here the acrylic block is a 4.3

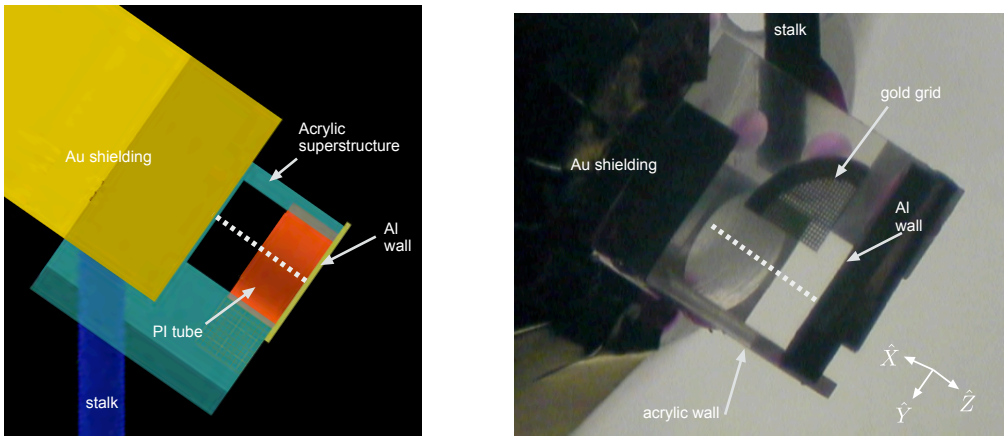

(a) "Bucket" target

(b) "Strip" target

Figure 3.2: Target perspective is such that the laser beams would be coming from the top left corner. Sn plasma still flows down a cylindrical axis (shown by the dotted line) towards the Al obstacle. In (a) the Au shielding is a bent foil that hangs diagonally away from the target near the drive foil. The polyimide tube is flush against the Al wall, such that a square piece of Al completely caps the end it. In (b), the Au shielding is supported by a large acrylic cone whose narrow end is around the drive foil. In the absence of the tube, the Al wall is made to be a long rectangular strip that now does not span the cross-sectional area of the milled cylinder. Although a window is cut through the acrylic body along the lines of sight of the images, the important feature is that acrylic walls are near the collision region in the orthogonal direction.

mm × 3.2 mm × 4.8 mm superstructure, that has a 2 mm diameter (and 4.8 mm length) cylinder milled into it. A 1.8 mm × 3.2 mm × 2 mm window is cut out of the structure and the polyimide tube is inserted at the end of it. This design results in a 1 mm space between acrylic and polyimide through which a fixed diagnostic soft x-ray spectrometer might record shock radiative flux. This spectrometer is referred to by the name Dante [82] and is very similar to a secondary diagnostic discussed at the end of this chapter. This target was fielded for two experimental shots, both of which returned unclear data. The images showed weak contrast between the upstream flow and the shock. Simulations show that once the incoming flow reaches the Al wall, it will be interacting with the walls of the polyimide bucket. This results in weak shocks being driven radially towards the center axis over the length of the polyimide. From the perspective of the desired reverse shock, these "wall shocks" are moving orthogonally towards it across the immediate the upstream region. It is assumed that this additional density causes the more attenuation to occur in the upstream region while producing data images, resulting in the worse contrast. The targets were not attempted after the first experimental campaign.

The second target design had the same superstructure as the bucket target. The two differences to its design were the absence of the polyimide tube and the dimensions of the Al foil. This "strip" target can be seen in 3.2(b) slightly tilted off axis so that it is possible to see the Al dimensions. The Al obstacle was > 2 mm $\times$ 1 mm $\times$ 100 μm, allowing radially extended plasma to move around the strip in the direction of the window. While this design produced diagnosable shocks and was used over the first three campaigns, there was still the presence of acrylic near the shock formation that affected the shock structure. This will be discussed in Chapter V.

3.2 Experimental constraints

Successfully creating and diagnosing a reverse radiative shock requires that a flow of enough material is sustained moving fast enough to produce a radiative phase. For laser-driven HED experiments the amount of mass involved in the fluid flow is limited by the deposited laser energy on the target. This amount of mass limits the flow velocity. In turn, this dictates the time scale of the desired experimental system conditions. Also, in order to image the radiative shock, there has to be enough material to fill above the resolution limit of the device. (These limits and the process of imaging are discussed at length in Section 3.3.)

The experiments employ a laser configuration of 10 beams with ∼4.5 kJ of energy, 1 ns square pulse, and 704 μm diameter FWHM spot produced by SG4 distributed phase plates (DPPs). These DPPs have an irradiance envelope *I(r)* approximated by a rotationally symmetric super-Gaussian profile [$I(r) \propto exp(r/r_0)^n$, where r is radius, $r_0 = 380$ μm, and $n \approx 4$] [33]. When combined with beam smoothing by spectral dispersion (SSD), the profile of time-averaged irradiance across the overall laser spot is very smooth. Because the drive foils are only 15 μm thick, beam smoothing is important to drive a uniform flow. With an irradiance of $\sim 10^{15}$ W/cm^2, a laser produces an ablation pressure slightly above 40 Mbar.

3.2.1 The plasma flow

In order to maximize forward direction of a Sn plasma flow, the layer of plastic is added to serve as an ablator. The ablation process is similar to a rocket, where forward motion is driven by mass leaving. In the laser-heated plasma, the approximation is used that light will propagate until the local electron density reaches a critical density where absorption occurs. The acceleration wave ahead of the absorption front is a strong shock [28]. Given the parameters of the ablator and the laser light, it is possible to approximate the pressure generated from the ablation process (∼40 Mbar

here) and a total ablated material depth, Δm. These derived quantities along with the initial thickness of the ablator, m_0, can then be used in the well-known "rocket equation",

$$V_f = V_e \; ln \left(\frac{m_0}{m_0 - \Delta m} \right), \tag{3.1}$$

which describes the final velocity, V_f, achieved by continuous ejection of material at output speed, V_e. In order to maximize forward velocity, (m_0 - Δm) should be minimized. The 10 μm thickness was chosen based on simulations such that maximum plastic and no Sn would be ablated by the laser. Laser ablation of the Sn would lead to unwanted x-ray production and preheat that could affect the initial state of the rest of target.

Previous work done by Harding et al. [39] showed that in order to create the most uniform flow with this technique, thermal evaporation deposition of the metal onto the plastic ablator produced minimal surface perturbations. Every iteration of these experiments used Sn deposited on Parylene-N. After the initial shock passes through the plastic and Sn, taking a few hundreds of picoseconds, it breaks out of the rear of the foil into the vacuum gap. The compressed Sn will now release and expand as it accelerates across the gap. The associated lateral expansion can be considered like the opening angle of a jet, given by $\tan\theta = \frac{c_s}{u_{flow}}$. As the flow accelerates forward into the vacuum gap, it expands less laterally. This forward motion is approximated as homologous expansion, which means the fractional rate of change of velocity is constant, at least up until the terminal velocity. In other words, v $\propto$ d/t and the terminal velocity will be designated as v_{max}, which based on simulation, is $\sim$200 $\frac{km}{s}$ or $\frac{um}{ns}$. For an obstacle at distance D, the radiative phase would begin at

$$t_{begin} = \frac{D}{v_{max}} < \frac{D}{200um/ns} \sim 20ns, \tag{3.2}$$

for a 4.0 mm distance D to the "wall". In the case of strong shocks, the post-shock

temperature, T_{ps} can be defined as:

$$T_{ps} = \frac{1}{k_B}\frac{Am_p}{(1+Z)}u_s^2\frac{2(\gamma-1)}{(\gamma+1)^2}. \tag{3.3}$$

Plugging this into the R_{rad} parameter equation (1.3) and setting $R_{rad} = 1$, it is possible to solve for a threshold velocity for radiative shocks:

$$u_{threshold} = \left[\frac{(\gamma+1)^8}{32}\left(\frac{(1+Z)k_B}{(\gamma-1)Am_p}\right)^4\frac{\rho}{\sigma}\right]^{\frac{1}{5}} \tag{3.4}$$

where γ is the polytropic index, Z is the ionization, k_B in the Boltzmann constant, A is the atomic weight, m_p is proton mass, ρ is the density of the flow material, and σ is the Stefan-Boltzmann constant. Using parameters for Sn, this velocity is ∼60 km/s. Given this number, a similar approximation can be made for the end of the radiative phase with

$$t_{end} \sim \frac{D}{v_{threshold}} \sim \frac{D}{60um/ns} \sim 67ns, \tag{3.5}$$

again for a 4.0 mm distance D to the 'wall'. These estimations suggest an experimental large enough window (ΔT) for diagnosing a radiative shocks in a system where the plasma flow collides millimeters away from its initial position, i.e. where the foil would be.

3.3 X-ray Radiography

The primary method to diagnose the shock system is to image it at different points in its evolution. X-ray radiography serves to produce a high-resolution x-ray image of the signal transmitted through a given target package. To image the range of densities present in the system, 8.95 keV x-rays produced from the irradiation of zinc are used. Their transmission through the target is recorded on Agfa Structurix D8

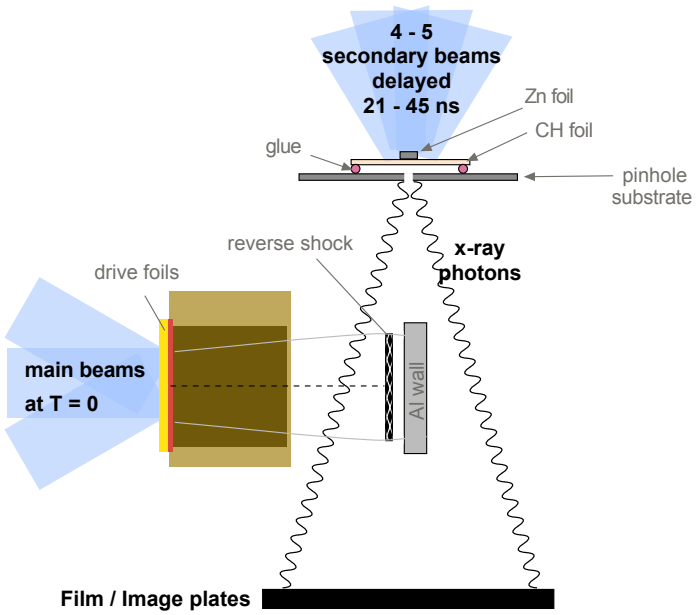

Figure 3.3: Cartoon of x-ray radiography. Secondary laser beams illuminate a thin metal to create an x-ray source which are funneled through a pinhole in order to image the main target.

x-ray film [52].

Figure 3.3 shows the basic layout of the point-projection x-ray radiography scheme. The x-ray source comes from the secondary target, referred to here as the backlighter. This target consists of a 7 mm square foil of 50 μm thick Ta with a pinhole in the center. A 3 mm square CH foil is attached to the Ta at a standoff distance of roughly 0.5 mm behind the pinhole, on top of which a Zn foil microdot 200 μm in diameter is centered. Secondary laser beams irradiate the foil and the surrounding plastic, creating metal plasma, plastic plasma, and the desired Zn He-alpha x-rays of energy 8.95 keV.

The plastic plasma flows outward with the metal plasma and tamps the radial motion of this plasma. This helps to prevent the exposure of the film by x-rays around the edges of the Ta. The purpose of the Ta is to both shield the diagnostic from hot coronal plasma emission created by the laser beams and collimate the x-ray source. The pinhole in the center of the Ta serves as a filter, only allowing x-rays

pointing directly at the target to pass. The experiments in this thesis used tapered pinholes such that one side has a larger 50 μm (or 20 μm) diameter opening and the other is 20 μm (or 10 μm) diameter. Using a tapered pinhole, as opposed to a straight (uniform diameter) pinhole, produces x-rays having a larger cone angle and a more uniform intensity. It can also reduce the sensitivity of the pinhole backlighters to rotational alignment.

In order to reduce the cross-talk, all experiments used a nose cone around each film holder. The main target is 228 mm from the film, and the 18 mm circular aperture mounted onto the narrow front end of the nose cone is 1/3 of that distance, at 76 mm from the target. With two pinhole substrates each displaced 12 mm from the flow axis along orthogonal lines of sight, two simultaneous images of the target are produced with a magnification of about 20 on the radiograph. Given the circular aperture, each radiograph has a field of view of roughly 2500 μm of the target. These images are taken at some delay to the initiation of the main beams, across the 21 ns to 45 ns range, where 4 to 5 secondary beams irradiate the Zn with a 1 ns pulse, 425 J/beam, and 800 μm spot size. This means that the x-ray source is on for roughly 1 ns. Improvements to this diagnostic technique have shown that less noise is detected with film when a gated detector is not required [48]. Therefore the images on the film are time-integrated over the course of the experiment which requires that the film be shielded at all times from all other sources of emission at energies above $\sim$1 keV. This is the reason all targets have large conical acrylic shields centered around the drive foils, as well as additional Au surrounding it.

The efficiency of zinc's conversion of energy to its 8.95 keV x-ray line is roughly 0.002 [91]. With four secondary beams of 425 J each and spot sizes of 800 μm centered on a 200 μm foil, this would result in 1.48×10^{14} x-ray photons. These photons are spread over the spherical emission behind the foil with only a fraction passing through the pinhole of 314 μm^2. This reduces the count to roughly 1.24×10^{10} photons. These

photons are emitted from the foil in a spherical cone of half-angle 16.7 degrees due to the taper. At a distance of 240 mm, the resulting cap spans $\sim 10^{10}$ μm^2. This yields a final intensity of $\sim$1.25 photons / μm^2. The number of usable photons is further reduced by the need for filters. The filters protect the imaging surface both from physical debris and from undesirable photon energies which may either pass through the target without obtaining information, or be emitted from elsewhere in the system which may harm or expose the film. These filters may reduce the number of photons at the energy of interest, yielding final photon estimates of 0.6 to 0.3 photons/μm^2. The optical densitometer used to scan the film has a pixel size of 22 μm square, yielding 290 photons/pixel in the scanned image. Spatial resolution in the target is practically limited by the size of the pinhole. Based on the magnification and scanning resolution quoted above, the scanner-side resolution is approximately 1.1 μm. However, the 20 μm pinhole creates a resolution element of $\sim$14 μm, or uncertainty in measurements of $\pm$7 μm. Sharper resolution can be obtained, but at the price of shrinking the area through with photons pass, and therefore lowering the quantity of signal.

3.3.1 High-energy background

X-ray radiography is a technique that has become very common in high-energy-density laser experiments. While the technique has advanced over the last decade, the inclusion of x-ray transmission test wedges (referred to as 'step wedges' in the next chapter) on the radiographed targets has shown still large amounts of background, despite improved contrast and resolution. Some preliminary backlighted characterization experiments suggest that the Ta pinhole substrate itself could contribute a higher energy background component through bremsstrahlung emission. This emission is dominantly in the energy range of 60 to 80 keV, consistent with its production by suprathermal electrons produced during the laser-plasma interactions.

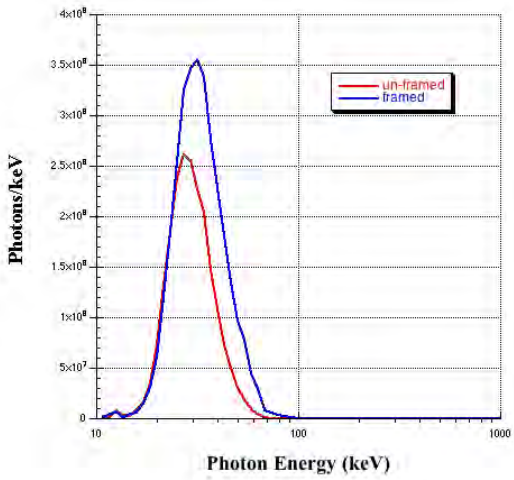

Figure 3.4: ITS output of BXMS data. Un-framed refers to the standard backlighted target used during the reverse shock experiments. Framed refers to the test experimental backlighter target shot encased in an acrylic.

In the characterizing experiment, the same backlighter target with Zn metal foils and 50 μm to 20 μm tapered pinholes were used. The targets were hit with a total energy of 2.25 kJ from five beams in a 1 ns pulse. Distributed phase plates were employed, giving a nominal spot size diameter of 704 μm, for a laser irradiance of $\sim$6 $\times 10^{14}$ W/cm^2. The primary diagnostic was a multichannel filter-stack detector for measuring the high energy x-ray bremsstrahlung radiation [15]. The bremsstrahlung spectrometer (BXMS) was oriented in the direction normal to the pinhole opposite the laser-irradiated side. In this configuration, it should only diagnose the signal that would reach the film if x-ray radiographs were being produced. BXMS uses k-edge and differential filtering with image plate dosimeters. The multichannel filter-stack detectors provide spectral information from 12 to 700 keV. The Monte Carlo electron/photon transport code INTEGRATED TIGER SERIES 3.0 (ITS) [37] was used to model the instrument, giving expected response for each image plate to x-rays in 80 logarithmically spaced energy bins from 10 keV to 100 MeV. Lead collimators and shielding prevented fluorescence-produced x-rays from materials inside the target chamber from affecting the signals recorded by the image plates. It is the fluorescence

of the filter materials themselves that the ITS model accounts for in analyzing the response of the diagnostic. The instrument has been absolutely calibrated, and the ITS model of the instrument has been validated experimentally [14]. An ITS simulation was also performed to model the target response to electrons in 150 logarithmically spaced energy bins from 0.01 to 100 MeV, providing an x-ray spectrum for each energy bin. By combining the response of the target to electrons and the response of the filter stack to x-rays, the best fit to a two-temperature electron distribution in the target was determined for the measured dose. Also, a calculation of the expected Kα signal was performed by injecting this two temperature electron distribution into the target, and using the Kα cross sections and photon transport models incorporated in ITS to determine how many Kα photons would be emitted in the direction of the detector. These data can be seen in Figure 3.4. 'Unframed' corresponds to the standard target, while 'framed' is a test backlighter target set into an acrylic framed target. The same relative sizes and distances are maintained with the addition of the frame. The same 200 μm diameter metal foil microdot is centered over the pinhole and fixed onto the CH. With this design, however, the front surface of the target has 1 mm of acrylic before the Ta substrate. The design theory to encase the pinhole substrate in the thick acrylic frame was an attempt to mitigate hot electron interaction with the substrate [1]. Looking at 3.4, however, the high energy background was within the same order of magnitude as that from the bare Ta target. As hot electrons are created during the laser plasma interaction and are expected to move in 4π sr, it can be suspected that a proportion of them make it to the front surface of the target to produce the harder x-rays via bremsstrahlung. In the standard target, these electrons would interact with the Ta substrate, producing the additional signal seen. In the framed target, it appears that interaction of such electrons with the 1 mm of added material made up any difference in bremsstrahlung emission.

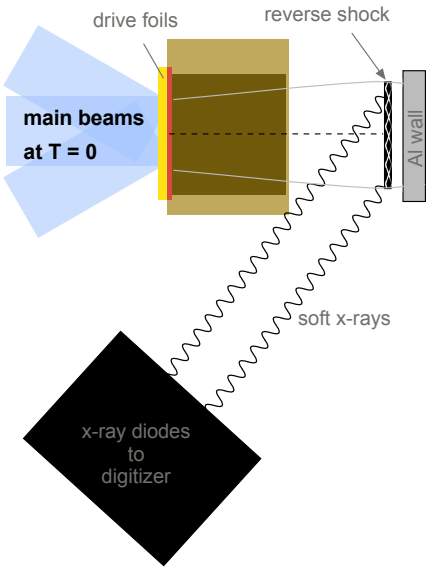

Figure 3.5: Cartoon of general μDMX geometry. The diagnostic is positioned such that it can record x-ray self-emission. Although not explicitly depicted in the cartoon, it observes the emission from the laser ablation surface as well as from the shock.

3.4 Other diagnostics

While the primary diagnostic throughout each experimental campaign was x-ray radiography, a few other instruments were used to contribute to data analysis. The Omega laser chamber is a 3.3 m diameter spherical structure with hardware ports at various (r, θ, ϕ) locations. There are 6 port locations that allow diagnostics to be inserted while the remaining options are all fixed. This limits the availability of instrument use on a given campaign or determines part of the target design. The following diagnostics were used on at least one of the four experimental campaigns.

3.4.1 μDMX

One additional goal at the onset of this experimental work was to record a 'light curve' from the radiative shock front. Simulations suggest that emission from the shock front could be on the order of 10's to low 100's of eV. Unfortunately this soft x-ray range of emission can be attenuated by target materials, which is why it is not

Table 3.1: μDMX spectrometer channels used

Channel	Element	Energy (eV)
1	Al	$38 - 68$
2	B	$131 - 182$
3	Mylar	$228 - 283$
4	Ti	$350 - 444$
5	V	$417 - 504$
6	Fe	$572 - 697$
7	Ni	$689 - 841$
8	Cu	$35 - 1199$

observed in the driven radiative shock case with a shock tube. The reverse shock geometry with the absence of superstructure near the shock formation offered the possibility. An absolutely calibrated broadband soft x-ray spectrometer with a high temporal resolution ($\sim$100 ps) called μDMX [11] was used. The detector in this spectrometer is a coaxial x-ray diode coupled with a fast single shot oscilloscope. The emitted x-ray spectrum is measured in 18 broad bands from 50 eV up to 20 keV. The softer bands $>$ 1.5 keV combine mirror and filter responses coupled with the coaxial diode response to improve hard x-ray rejection. The cathode for each channel is chosen so that no material x-ray transmission edges are present in the primary spectral region of interest, and each channel's spectral sensitivity is defined by K and L edge filters. The measured the x-ray power emitted by the plasma is recorded in time to provide signal versus time information, the effective 'light curve' of radiation temperatures. Only the channels listed in Table 3.1 were implemented.

Due to the placement of μDMX in the chamber, each version of the target had to be made such that there was a clear line of sight from the spectrometer to the shock region. This is the reason for only 3 acrylic legs holding the Al foil in the final design. The perspective to target also allowed the spectrometer to record the emission from the initial drive foil irradiation. This gave relative timing measurements between flow

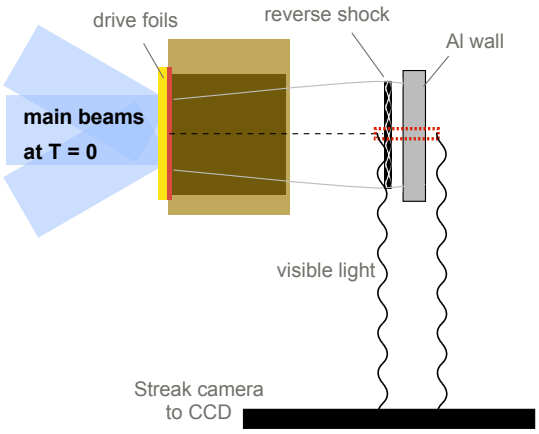

Figure 3.6: Cartoon of the SOP geometry. The diagnostic records optical self emission in 1D and streaks it in time

creation and collision, in turn giving an estimate of the average velocity of the flow.

3.4.2 X-ray pinhole camera

X-ray pinhole cameras (XRPHC) are routine diagnostics on the OMEGA target chamber and are typically used on every target shot where the UV intensity is sufficiently high ($> 10^{14}$ W/cm^2) to generate x-ray emission from the laser target. They are in fixed locations around the chamber. Similar to the x-ray radiography, laser-drilled pinholes in thin Ta substrates provide the desired x-ray imaging. The pinhole diameters are currently 10 μm, with a typical target-to-pinhole distance of 17 cm and a 68 cm pinhole-to-image distance, giving a magnification of 4 [61]. The pinhole cameras have an electronic readout using charge-injection devices (CID's) that provide near-instantaneous images of target x-ray emission. This allows checks on beam locations on the target immediately after the laser has fired. Given the location of the target in the chamber, one XRPHC looked directly at the laser spot of the main target and gave a relative intensity of the x-ray flux stimulated there.

3.4.3 Streaked Optical Pyrometer

In the earlier campaigns of this experiment, an optical pyrometer was used to detect the thermal emission from the final 500 μm of the experimental target (at the Al wall) over the full time scale of the experiment, depicted by Figure 3.6.

This produced absolutely calibrated, time-resolved emission. The diagnostic consists of an image-relay system such that the self-emission passes through a series of mirrors, long or short-pass filters, and lenses that are used to focus the image on the input slit of a streak camera recording on a charged-coupling device (CCD). The final digital output from these experiments using a 3×3 binned CCD is a 682×690 array [65], where the dimensions correspond to a spatial view along the length and width of the slit streaked over the set experimental time. This can give the velocity of emitting regions.

CHAPTER IV

Experimental Data from Normal-Incidence Reverse Shocks

This chapter shows results from experiments observing the development of the normal-incidence radiative reverse shock. The general experimental setup described in the previous chapter by Figure 3.1(a) has been successfully fielded during parts of four separate shot days over the last three years on the Omega laser. Success of these shot days primarily depended on target quality and availability, diagnostic understanding, and laser performance. As mentioned in Section 3.1.1, evolution of the target design occurred over the course of these shot days, and the final target design incorporating no walls at the interface was only fielded on the final day in July 2012.

The primary discussion presented in this chapter is from un-gated x-ray radiography data. Two methods of inferring shock compression are shown. Supplementary information from secondary diagnostics plays a role in extrapolating results. Conclusions throughout this chapter are suggested with interleaved discussion of the secondary diagnostic data. In addition to the Sn drive foil target, a comparison test target was also shot with Cu, producing a reverse shock in a Cu flow. Simulations of both experiments were performed using the CRASH radiation hydrodynamics code [86] and will be discussed briefly as well.

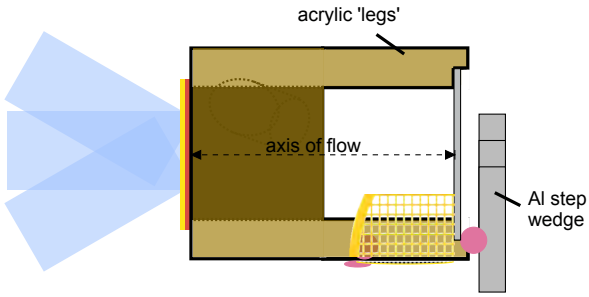

(a) View of $\hat{X}$-$\hat{Z}$ plane

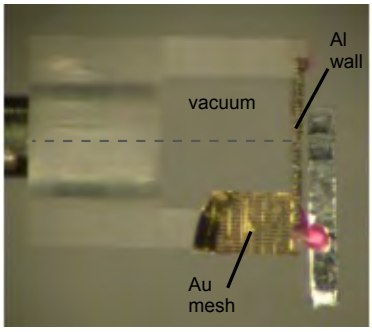

(b) View of $\hat{X}$-$\hat{Z}$ plane

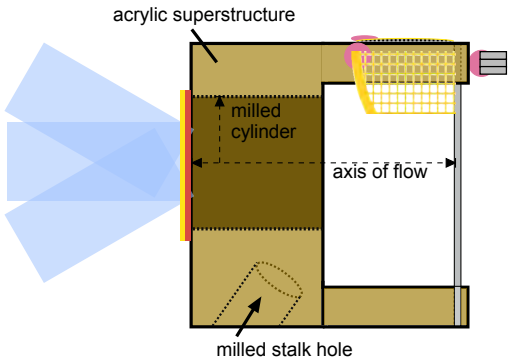

(c) View of $\hat{Y}$-$\hat{Z}$ plane

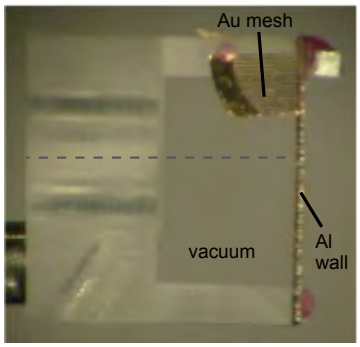

(d) View of $\hat{Y}$-$\hat{Z}$ plane

Figure 4.1: Orthogonal views of main target body, each of which is an x-ray radiography line of sight. In the cartoon images of (a) and (c), blue rays represent the laser coming from the left which irradiate the drive foils, shown in yellow and red. (b) and (d) show the corresponding built target bodies. All pink dots are glue. The conical shield around the laser spot is not shown.

4.1 Data measurements

As discussed in Section 3.3, the aim is to diagnose density distribution within the reverse shock, and in the surrounding medium, from two orthogonal views by point projection x-ray radiography. In a single experimental shot, data from two views corresponds to three total targets in the chamber: 2 backlighters and 1 reverse shock target. Backlighter metals were chosen such that the He-α x-rays should produce a good contrast in attenuation between (un-shocked) accelerating flow and the dense shock. Prior to the experimental campaign, this decision is made by using a cold

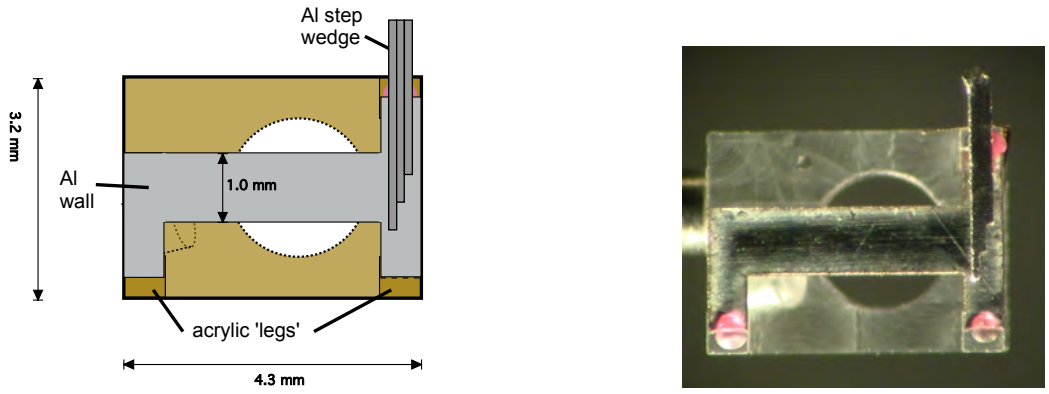

(a) View of $\hat{X}$-$\hat{Y}$ plane

(b) View of $\hat{X}$-$\hat{Y}$ plane

Figure 4.2: View of main target body along the axis of flow, or target axis. The Al obstacle does not full span the cross-sectional area of the milled target cylinder and the acrylic 'legs' that hold the Al onto the target are far from the center of the cylinder. Again all pink dots are glue.

opacity library to calculate the amount of radiation a material absorbs at a specific density and thickness. Density profiles from 1D HYADES runs, such as Figure 2.1, are used to scope the experiment. Figure 5.2 shows each diagnostic view of the target, orthogonal to both the Al obstacle and the axis of flow. Figures 4.1(a) and 4.1(c) show cartoon depictions where drive foils and beams are added for perspective. Figures 4.1(b) and 4.1(d), respectively, show the corresponding constructed targets.

It is important to note that although both target views appear to have the Al wall spanning the left edge of the target, it does not do so at the area of collision in this radiograph. This illusion is an artifact of needing to attach the Al wall to the acrylic target structure, which happens along the same line of sight as the radiograph. This can be realized by examining Figures 4.2(a) and 4.2(b) which show the view along the axis of flow, the third orthogonal target plane. These images illustrate that the Al wall is a strip that does not cover the entire cross-sectional area of the milled cylinder. If the flow expands to the extent of the target cylinder, then unshocked Sn can move around the Al wall. This should be noticeable in the radiograph with the perspective of Figure 4.1(a), where the Al wall has 1 mm height (in the $\hat{X}$ direction). It is also important to note that along the line of sight of Figure 4.1(a), the Al wall

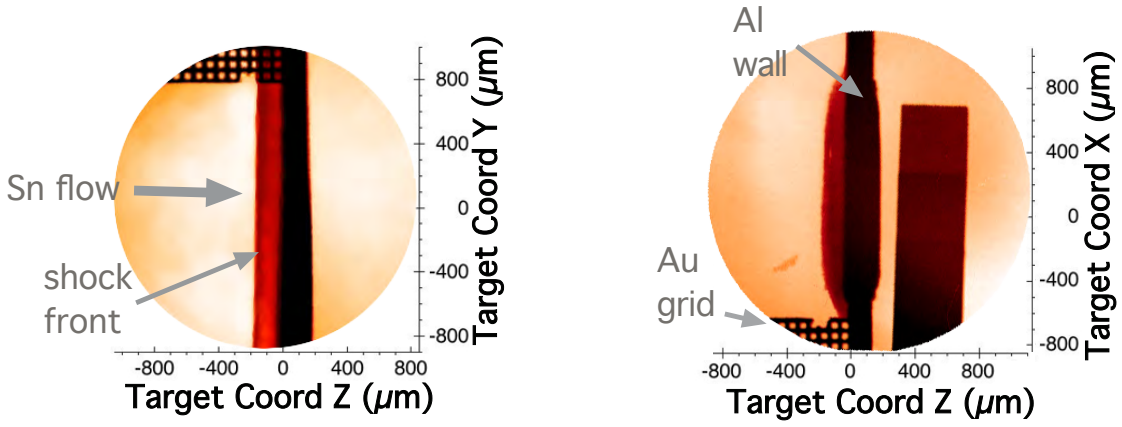

(a) View of $\hat{Y}$-$\hat{Z}$ plane

(b) View of $\hat{X}$-$\hat{Z}$ plane

Figure 4.3: Simultaneous radiographs taken at 34 ns.

depth is ∼4.3 mm. Again, this can be seen by referring to Figure 4.2(a). Along the line of sight of Figure 4.1(c), the Al wall will only be 1 mm. In both cases, the ≥1 mm Al wall dimensions are opaque to the He-α x-ray backlighter energies.

Gold grids can also be seen in both radiography views. These are added to the target to serve as a spatial fiducial in the data because Au will be opaque to very high x-ray energies and should always be seen in the radiograph. Experimental targets are destroyed under the HED conditions and therefore not recovered after the shot. Thus, all data images are calibrated using information from pre-shot target characterization. Careful measurements give the location of edges of the gold grid mounted on the target, as well as the features cut into the grid at regular intervals (seen in Figure 4.3), relative to the Al foil and the axis of flow. The Au grid also serves as a calibration of the magnification of each image. Additionally, three 115 μm steps of machined Al, referred to as a step wedge (seen in Figure 4.7), are attached along one of the lines of sight. This is used to identify x-ray source background and is discussed further in Section 4.1.2.

A pair of experimental radiographs is shown in Figure 4.3. The ∼2 mm field of view in the target plane is centered roughly around the Al wall, the darkest vertical

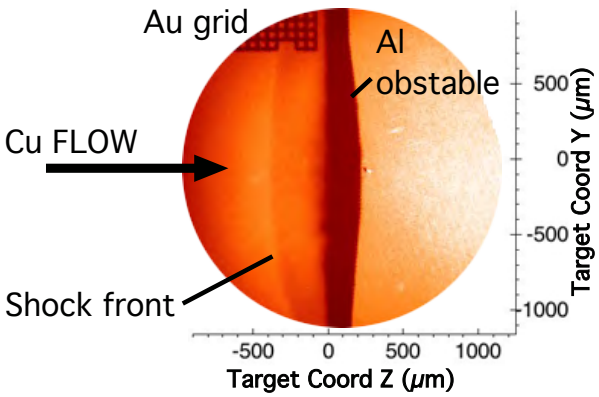

Figure 4.4: Radiograph at 39 ns of Cu flow shot

band that spans the diameter of the image. It should be noted that the color scale is not fixed between images. As the Sn flow comes in from the -$\hat{Z}$ direction, the reverse shock forms to the left of the original Al wall position, Z = 0 in the target coordinates. In both images, the shock front is roughly located at Z = -150 μm, while the shocked Sn layer thickness is less than 150 μm. In Figure 4.3(b), the shock only forms in front of the 1 mm height of the Al wall. Evidence of material moving around the wall can be seen much like a bow shock in the $\hat{X}$ direction. The thin dense layer of shocked Sn is harder to distinguish in this image because the material depth is at least 2 mm for the shock. This means that any material behind the dense layer will absorb more x-rays than in the radiograph of Figure 4.3(a). Here the reverse shock forms along the entire field of view and x-rays are attenuated only through roughly 1 mm of depth. From this radiograph, the shock layer thickness is roughly 40 μm, over an average of the data from a window ΔY = 250 μm high.

4.1.1 Cu comparison

In an effort to compare the effects of radiative cooling on the compression of the shock layer, an identical target body was shot with a plastic/Cu drive foil instead of plastic/Sn. Recalling from Chapter II, for strong shocks the initial post-shock temperature, T, is proportional to Au_s^2.

In attempt to isolate the effect of the material, i.e.A, the Cu thickness was scaled to 4 μm so that the areal mass driven would be the same, producing roughly the same velocity. Since $A_{Cu} \sim 0.5\ A_{Sn}$, the Cu shock should not be able to reach as high of a temperature. Consequently, it should be less radiative and produce an observably different shock structure. The radiograph in Figure 4.4 shows data from the Cu shot, which has a noticeably different profile. With the Cu flow moving in from the -$\hat{Z}$ direction, the shock front is roughly 400 μm from the Al wall, which is further extended from the wall than that seen in the Sn case. Also, the shocked layer appears to have a uniform transmission over that width. Further analysis of this is discussed in Section 4.1.2. but this suggests that the shock width is roughly the same as shock front position, $|Z|$.

A distinguished difference between radiative shocks and non-radiative shocks in the laboratory is the compression. Shown in Chapter II, as the temperature decreases via radiative cooling, the density increases behind the shock wave. As the shock strength increases, so does the compression ratio. On the contrary, a non-radiative strong shock in an ideal gas where $\gamma = 5/3$, is limited by $\frac{\gamma+1}{\gamma-1}$ to a compression of 4. Processes that increase the internal degrees of freedom of a gas will lower the polytropic index γ, and thus increase the initial compression. Since the compression across a radiative shock can be $\gg 4$, the easiest way to identify the radiative cooling effects on shock dynamics from x-ray images is to determine compression ratio. The following two sections each detail a method for doing this.

4.1.2 Geometric analysis

The first method of calculating compression uses only spatial measurements taken from the radiographs. This is why it is referred to as "geometric" analysis. The estimation of the shocked layer compression can be done geometrically, because the lateral movement of the flow is small. The basic idea is that the width of the shock,

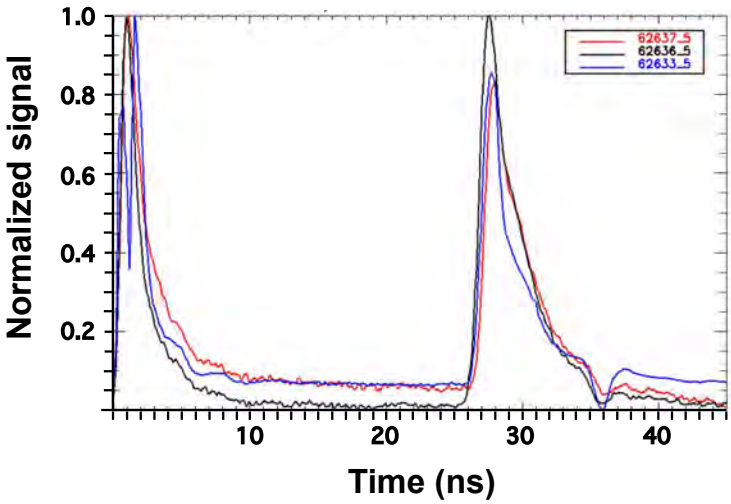

Figure 4.5: Normalized μDMX data for three individual shots taken on 470 eV channel

W_{shock}, will be the length of the material that flowed into the shock, L_{flow}, divided by the shock compression, ϵ. Thus compression, $\epsilon = \mathrm{L}_{flow}/\mathrm{W}_{shock}$. The length L_{flow} is the incoming flow velocity times the duration over which the flow accumulates in the shocked layer. Because the stream has to cross the vacuum gap over the length of the target body, the time of the collision must be subtracted from the time of the radiograph for its respective analysis. Based on the length of the target and the data, the average flow velocity is about 150 μm/ns and the shock formation occurs at 27 ns. Thus

$$\epsilon = \frac{150[\mu m/ns] \times (t_{radiograph}[ns] - 27[ns])}{W_{shock}[\mu m]}. \tag{4.1}$$

Over the entire data set of radiographs for Sn shots taken from 29 ns to 40 ns after the main beams, a calculated a range of minimum compression was 10-45, significantly higher than the adiabatic limit for strong shocks of 4. The term "minimum compression" refers to a maximum W_{shock} measurement, in which the value was taken to be the separation of the shock front from the initial wall position. For data that had distinguishable thin dense layers near the shock front, the compression range

was closer to 20-45. Similar analysis of the Cu shot suggests that it is nearly at the non-radiative limit, between ∼4-5. This is a promising result for future experiments that may attempt to alter the radiative regime of the shock system.

In consideration of uncertainty, the relative timing of the collision is confirmed using the x-ray diode spectrometer, μDMX, that is positioned to obliquely observe both the drive foil ablation and the shock ∼30 degrees from its normal. It collects soft x-ray emission in time giving a spatially integrated "light curve". This data shows immediate emission from the drive foil plasma which occurs when the laser first turns on and the radiation that occurs at the collision of material with the Al obstacle. Normalized data can be seen in Figure 4.5 for three individual shots. While μDMX data was not recovered on every shot, those for which it did had relative times of 27 ns ± 500 ps. Although the error may be significant for radiographs taken close to the collision time, most data was taken at times where $\Delta t > 5$ ns, where Δt is the time difference between the radiograph exposure and the collision. In fact, the shots that recorded radiographs without μDMX data were taken at $\Delta t > 8$ ns. It is also important to note that any tilt along the radiograph line of sight will decrease the inferred compression [22]. This is true because any tilt out of the plane of the radiograph has the asymmetric effect of only increasing the apparent width of the layer. The correction to the compression ratio in order to account for tilt is

$$\epsilon = \frac{150[\mu m/ns] \times (t_{radiograph}[ns] - 27[ns])}{W_{shock}[\mu m] + h_{shock} \tan|\beta|}. \tag{4.2}$$

where h_{shock} is the height of the shock and $|\beta|$ is the absolute value of the shock inclination angle. As mention previously, dual radiography can help compare the line of sight for each radiograph because they are orthogonal to each other. This can reveal measurements of β. For these normal-incidence experiments, observed thicknesses of the Al from radiographs reveal that any such tilt was small. This concept is revis-

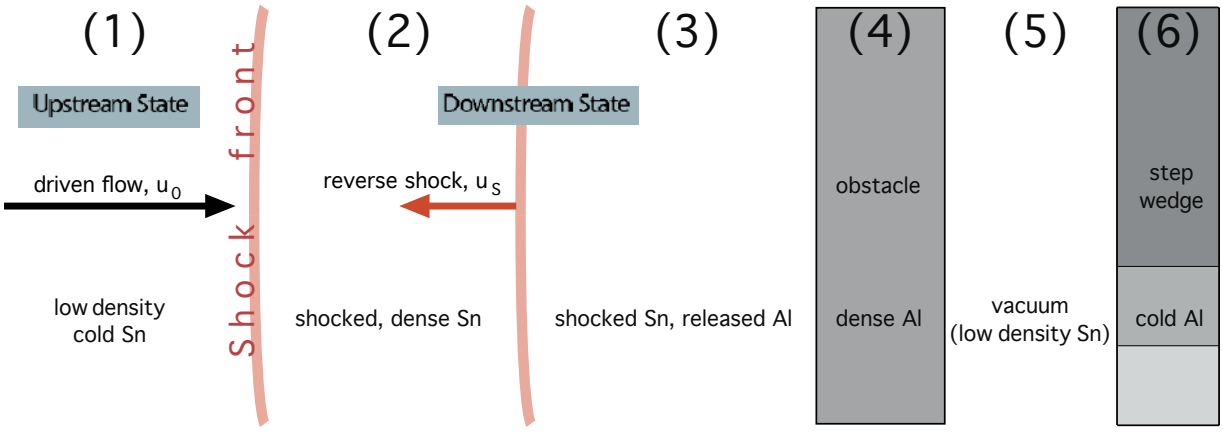

Figure 4.6: Cartoon of the reverse shock system defining the separable areas of interest. The driven Sn flow is moving left to right with speed u_0 in area (1). The shock (red boundary) is moving right to left with speed u_s to define area (2). Area (3) is the area between the dense layer of the radiative shock and the Al wall which data suggests is likely a combination of Sn and Al released from the wall. Beyond this, (4) is the Al wall, (5) is the target exterior which should be vacuum, and (6) is an Al step wedge.

ited in Chapter VI where there is observable confirmation that the oblique incidence targets have components that tilt out of the plane of the radiograph. This was most likely due to the structure of the target but can also arise from misalignment.

If there had been more tilt in the data, it would have similarly affected the second method of estimating compression ratios. This potentially important effect of misalignment and/or tilt out of the plane of the radiograph could change transmission through the dense material. Any tilt would mean that the x-rays from the backlighter would penetrate less material along its line of sight, making the assumed edge to appear more transparent. This, in turn, would affect the mass density profiles that are extracted from the radiographs.

4.1.3 Radiograph mass-density analysis

Mass attenuation along the line of sight in an x-ray image can be expressed by the Beer-Lambert law as

$$I = I_0 e^{-\mu m/A} \tag{4.3}$$

where I is the measured pixel intensity, I_0 is the x-ray source intensity, μ is the x-ray attenuation coefficient in units of area per mass, m is the integrated line of sight mass, and A is the pixel area in the image. With a background intensity level I_b and multiple x-ray frequencies, ν, passing through multiple materials i the general formula becomes

$$I = \sum_{\nu} I_{0,\nu} \prod_{i=1,2,3,\ldots} e^{-\mu_i(\nu) m_i/A} + I_b. \tag{4.4}$$

In order to estimate the mass density in the shocked region, the above equation must be simplified with two assumptions. First, the backlighter material, Zn, is assumed to emit a monochromatic spectrum. Second, the assumption is made that only Sn and/or Al will intercept the x-rays from the x-ray source in the diagnostic view. Figure 4.6 shows a simplified version of Figure 2.2 that categorizes the shock system into four sections: (1) unshocked Sn flow, (2) thin dense shocked Sn layer right across the shock front, (3) the area between the dense Sn shell and the Al wall and (4) the Al wall. In (1), (2) and (4), it is reasonably assumed that there is only one material along the radiography line of sight, while in (3), there is likely some combination of Sn and Al. For purposes of calculating I_0 and I_b, two other areas are considered: (5) space beyond the Al foil where there is no target material prior to the shot and (6) the Al step wedge. Including these assumptions, the above equation becomes

$$I = I_0^* e^{-\mu_i(\alpha) m_i/A} + I_b \tag{4.5}$$

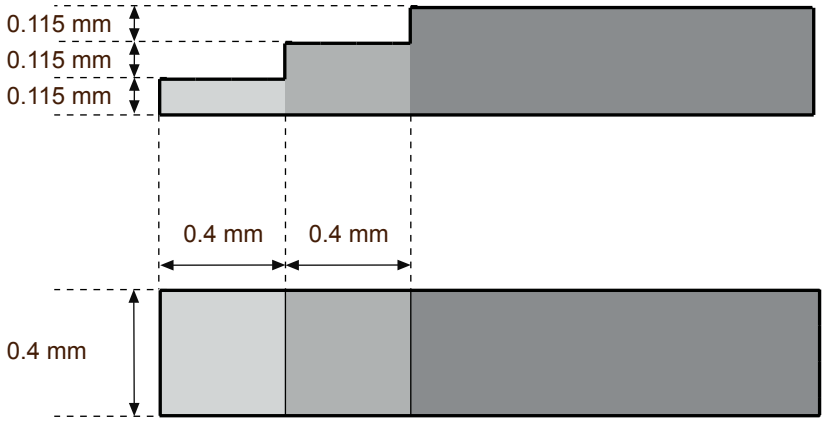

Figure 4.7: The dimension of the Al step wedge that serves as an x-ray calibration feature.

for areas (1), (2) and (4) with the appropriate material i, and

$$I = I_0^* e^{-\mu_{Sn}(\alpha) m_{Sn}/A} e^{-\mu_{Al}(\alpha) m_{Al}/A} + I_b \tag{4.6}$$

for area (3), where α refers the He-α line. Since I_0 is a measured value from the x-ray radiograph, it is represented as I_0^* which will include any attenuation from other materials whose contribution is approximated as constant. For example, I_0^* is found by taking the average intensity of pixels in area (5), which would be vacuum prior to the shot. During the time of the radiograph however, it is likely that low density target material, such as the unshocked Sn flow diverted around the Al wall, would have moved into that area. This Sn attenuates very little of the x-ray source so it is ignored.

The background intensity I_b includes all sources of non-directional exposure and unattenuated high-energy x-rays. A discussion of known sources of background is included in Appendix B. It can be measured if the image includes an object that has known transmission for the x-ray source. The Al step wedge (shown in Figure 4.7) is attached to the target so that it is in the field of view of the radiograph but should not have any interaction with the shock system. This can be seen in the radiograph of Figure 4.3(b). The exponent, $\mu(\alpha)m/A$, equal to the optical depth, τ, can also be

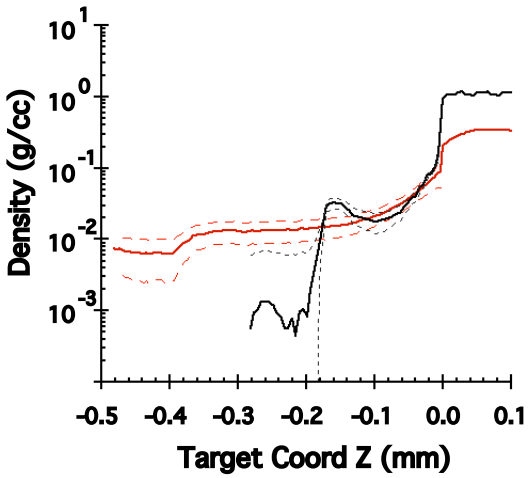

Figure 4.8: Extracted density profiles from experimental radiographs for shock in Sn (black line) and Cu (red line). Dotted bounds of the same color show range of error associated with the large background and assumption of a monochromatic x-ray source.

represented as $\mu(\alpha)\rho L$ where ρ is the material density and L is the material thickness. With three 115 μm steps, L can be represented by $0.0115(n-1)$, where n is the number of the step. Given the solid density of Al and a constant mass attenuation coefficient for the x-ray source energy

$$I = I_0^* e^{-\mu\rho 0.0115(n-1)} + I_b \tag{4.7}$$

can be solved for I_0^* and I_b. Applying these values to Equation 4.5 for I_0^* and I_b, and rearranging, the expression for mass density in a region with one material of depth x is

$$\rho_i = -\frac{1}{\mu_i x} \ln\left(\frac{I - I_b}{I_0^*}\right). \tag{4.8}$$

When using Equation 4.8 to infer density profiles from a radiograph, the material depth x here can also be called the height in the respective $\hat{X}$ or $\hat{Y}$ target coordinate direction of the orthogonal radiograph. Figure 4.8 shows the inferred, relative mass density profile from a Sn shot and from the shot with Cu using this equation. Again, these profiles were obtained using an average of the data over a window 250 μm high

and through regions (1) through (4). The leftmost part of the profile corresponds to region (1), the incoming flow. The density increase near Z = -400 μm for Cu and Z = -150 μm for Sn represents the shock front. From these mass density profiles, the inferred compression ratio for Sn is $\gg 4$, suggesting the much denser layer as expected from radiative cooling. Comparatively, the compression in the Cu shot ranged from 3-4 times the incoming flow density. This is in good agreement with the geometric analysis to suggest that effect of radiative cooling can be seen between these two shots. The error in the density profiles is represented by dotted lines in Figure 4.8.

The evaluation of uncertainty here follows similar analysis detailed in [38]. The error is due to both the uncertainty in the measurement as well as to the assumptions in the model. The values of I_0^* and I_b are measured and therefore have some statistical error associated with them. The value of I is the single value of a single pixel and does not have any statistical error but may reflect the statistics of finite photon numbers. Although it may be measured, as mentioned above, x in Equation 4.8 is taken to be a constant over the ΔZ width of the shocked material. Since the mass-attenuation coefficient is dependent on x-ray energy, the error due to the approximation of a monochromatic backlighter source can be represented by

$$\delta I_\mu^2 = \sum_{\nu,i} \left(\frac{dI}{d\mu_i(\nu)} \delta\mu_i(\mu) \right)^2 \tag{4.9}$$

where $\delta\mu_i(\mu) = |\mu_i(\mu) - \mu_i|$. The value of δI_μ^2 is less than or equal to

$$\sum_{\nu} \left[I_0^* \rho_{i,max} x e^{-\mu_i(\nu)\rho_{i,max}x} \right]^2 \left[\delta\mu_i(\mu) \right]^2 \tag{4.10}$$

where $\rho_{i,max}$ is the maximum density of material i. In the areas of interest, regions (1) through (3) from Figure 4.6, $\rho_{i,max}$ can be approximated by the solid density of the materials. This error is added to a measurement error δI_0^* of the mean pixel value in region (5). Combining Equation 4.10 with a standard error calculation, the

mean-square error in the density becomes

$$\delta\rho_i^2 = \left(\frac{\partial\rho_i}{\partial I_0^*}\right)^2 \left((\delta I_0^*)^2 + \delta I_\mu^2\right) + \left(\frac{\partial\rho_i}{\partial I_b}\delta I_b\right)^2 \tag{4.11}$$

$$= \left(\frac{1}{\mu_i x}\right)^2 \left(\frac{(\delta I_0^*)^2 + \delta I_\mu^2}{(I_0^*)^2} + \frac{\delta I_b^2}{(I - I_b)^2}\right) \tag{4.12}$$

The profiles shown in Figure 4.8 were calculated using mass attenuation coefficients corresponding to Sn or Cu, as appropriate, over the all regions (1)-(4). This means that the density of the Al wall of region (4) is not accurate. However, the abrupt edge of the Al wall is still visible by the steep rise and plateau in density on the right side. The exponentially decaying profile to the left of this edge can be interpreted as expanding Al plasma of region (3). The details of material(s) in this region are difficult to evaluate more specifically, e.g. mass ratio, due to the 2D nature of this diagnostic.

4.1.4 Expanding Al

"Preheating" is always concern in HED laser experiments. The laser interaction with the plasma can cause unwanted energetic electrons or photons that can penetrate the target materials prior to the desired experimental physics occurring [63]. This early heating can change the initial conditions of the experiment and thus lead to the misinterpretation of data. In the reverse shock experiment, it is possible that Al plasma from the obstacle can be released before the shock formation by radiation from the Sn flow itself or by either photon or electron preheat. Such a release of material could lead to a misinterpretation of the thickness of the shocked Sn layer. If the density of the Al happened to be such that the absorption of the diagnostic x-rays were equal in the Sn and the Al, the inferred layer would appear thicker. Even if this occurred, it would not invalidate the conclusion that the Sn had reached densities far above those that non-radiative shock would reach. 1D HYADES simulations done

with varying Al density profiles also found that the dynamics of the reverse shock were not affected, but only its position.

One indiction that preheat is likely in some of the shots performed on this campaign is seen in x-ray pinhole camera (XRPHC) data. One target modification not mentioned previously was the thickness of drive foils chosen. In order to attempt to maximize the flow velocity, discussed in Section 3.2.1, targets were produced with a 6 μm plastic, 4 μm Sn drive foil in addition to the 10 μm plastic, 5 μm Sn. All shots had the same irrandiance of $\sim 10^{15}$ W/cm^2. While there is not quantitative measurement of the x-ray flux, one x-ray pinhole camera (discussed in Section 3.4.2) had a nearly orthogonal view to the drive foil. Data from this XRPHC shows roughly 15% of the intensity when irradiating the thicker plastic layer than what was recorded for thinner plastic layer. This means that much more and likely harder x-ray flux was produced at the laser spot and presumably some of that flux would preheat the target.

While simulations suggest that the laser light itself should not reach the Sn, there are other causes of what might be considered laser burnthrough. One of these is if the heat front created by the laser reaches the Sn foil. If the buried surface between the plastic and Sn layer gets hot enough enough to produce x-ray emission, this could account for the data seen in the XRPHC. Ideally, in the opposite direction, any emission from this surface would be absorbed in the remaining Sn. If the emission reaches a few keV than these x-rays will be only partially stopped by the Sn foil whose L-edge is around 4 keV and could be deposited in the target components including the Al wall. A important characterizing experiment could be done to observe this heating by using diagnostics to monitor the rear side of the Sn without the Al wall present. This would be a worthwhile experiment to gain understanding of emission near the drive surface for not only preheat concerns but also background seen in the ungated radiographs which is discussed in Appendix B.

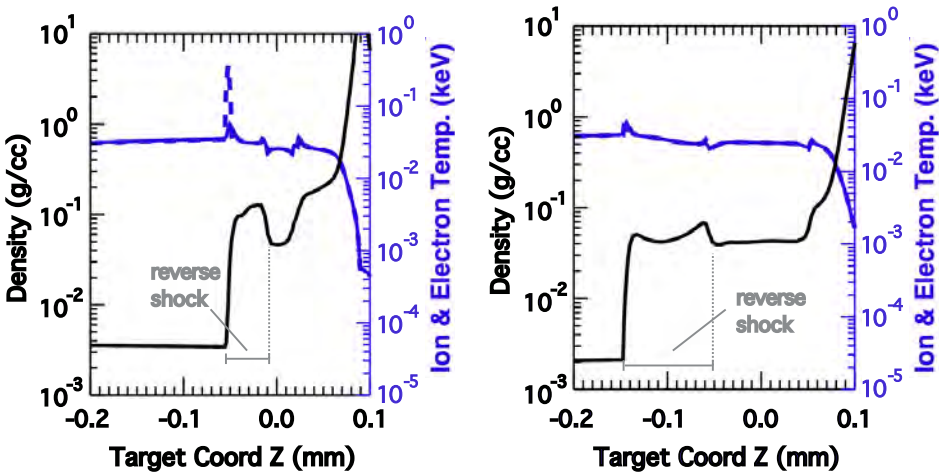

(a) Reverse shock in Sn (b) Reverse shock in Cu

Figure 4.9: Density and temperature (ion [dotted] and electron [solid]) profiles at target radius of 120 μm at same timestep of 2D CRASH simulations.

A final note for clarity should be made regarding the drive foil layer thicknesses. When the XRPHC revealed more x-ray flux at the laser-ablation surface for the thinner drive foils, the decision to use only 10 μm plastic/5 μm Sn, i.e. the thicker drive foils, was made in order to mitigate preheat for all later shots. However, the manufacturer was changed between experiments in order get better characterized foil thicknesses. The final campaign of experiments used a vendor that offered sub-micron tolerances for their deposited foils, which had not be qualified by the previous manufacturer. In these final experiments however, the XRPHC showed the same increased flux results of the thin foils for the 10 μm plastic/5 μm Sn foils. Post-experiment characterization of the earliest campaign drive foils using a scanning electron microscope (SEM) showed some 2 to 5 μm variations from the desired 10 μm plastic layer thickness. Additional plastic in the ablation layer would be the most plausible explanation for this reduction in x-ray signal and could clarify why multiple experiments intended to be shot with 10 μm plastic and 5 μm Sn showed very different results.

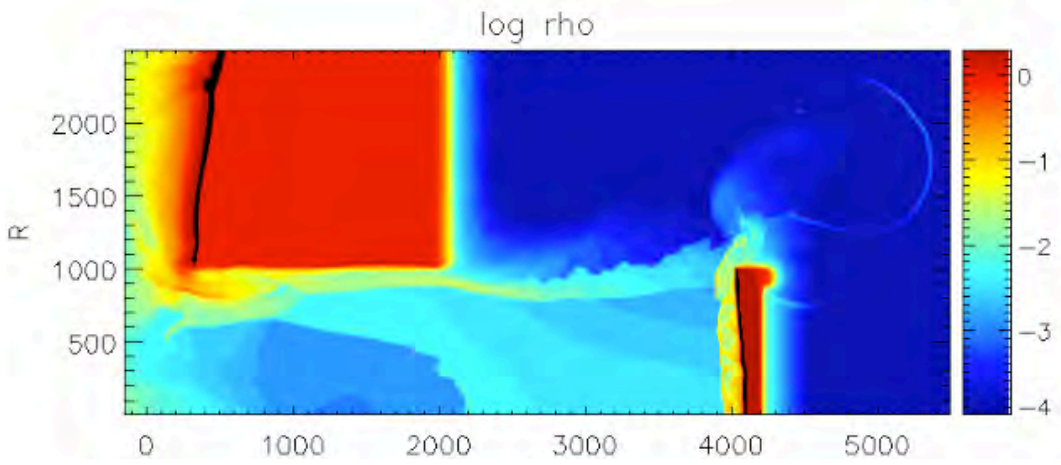

(a) 2D CRASH simulation of experiment with Sn drive with radiation

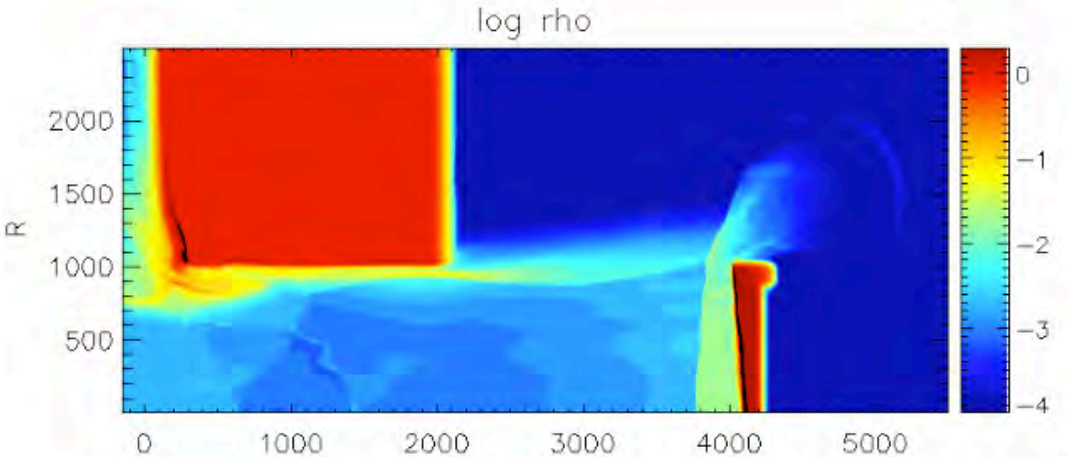

(b) 2D CRASH simulation of experiment with Sn drive without radiation

Figure 4.10: A comparison of the effects of radiation transport in experimental simulations with Sn.

4.2 CRASH simulations

In conjunction with these experiments, both 2D and 3D computational work was performed with an Eulerian, block-adaptive, radiation hydrodynamics code developed by the Center for Radiative Shock Hydrodynamics (CRASH) at the University of Michigan [86]. This model uses multigroup diffusion for the radiation transport model, which, along with electron heat conduction, is solved implicitly. It utilizes tabular equation-of-state data. The results shown here were initialized from the results of simulations of laser energy deposition in the system using the H2D code, an extension of the 1D Hyades model. The runs usually use an axially symmetric geometry about the center of the target cylinder using an R-Z coordinate system.

Figure 4.9 shows axial profiles at 120 μm radius for both the Sn and Cu experiments at the same time-step. The density profiles (solid dark line) show the respective shocks and the varying radiative cooling effects. One can see the same qualitative differences in shock front position from the initial Al wall at Z = 0 and the thickness of the shocked layer itself as with data shown in Figure 4.8. In the simulation results, the shocked Sn layer is less than half the width of the shocked Cu layer. The shock wave in Cu not cooling (as) radiatively, is less dense, and thus expands further from the wall. This is also seen by the temperature curves (blue lines) at the shock front position in the Cu case where the ions and subsequently electrons are not heated as much. For further validation, an identical CRASH simulation with Sn was run with no radiation transport. Figure 4.10 shows a direct comparison of 2D log density plots. The output in Figure 4.10(a) shows the compressed flat profile seen in the experimental data, while Figure 4.10(b) a shock more similar to that seen in the Cu experiment. In a third run, not shown, a simulation was run with Xe as the drive material because $A_{Xe} > A_{Sn}$. The result was even higher compression and less axial distance from the wall.

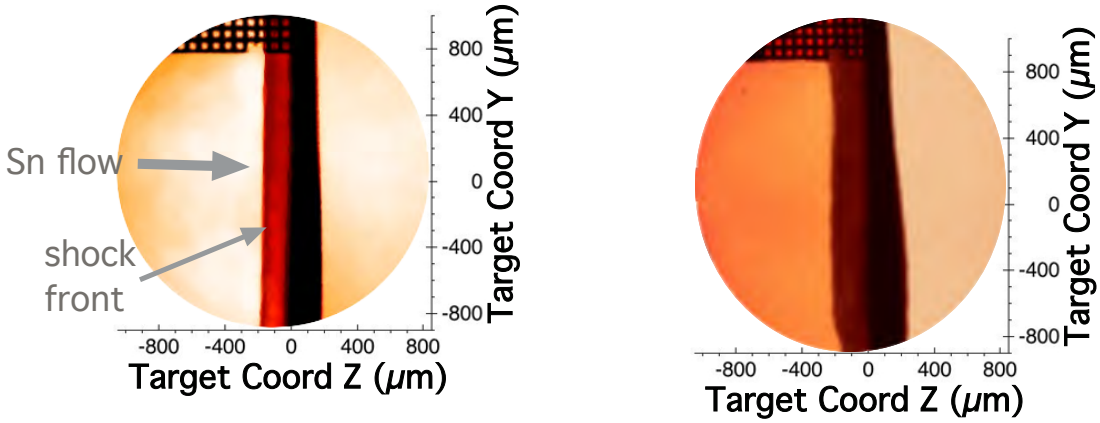

(a) Normal collision at T = 34 ns

(b) Normal collision at T = 39 ns

Figure 4.11: Time sequence of normal incidence radiative shocks

4.3 Time sequence of shots and SOP

An orthogonal pair of radiographs is captured once per experimental shot. The exposure of the film is determined by ∼1 ns pulse length and the timing of secondary laser beams that irradiate the Zn foils. If the reverse shock was moving significantly fast, there would be a blurring effect caused by the motion of the shock over the 1 ns length of the backlighter laser pulse. 1D simulations suggest that the reverse shock moves between 5 to 15 μm/ns during the strongly radiative phase when it first forms. Using point-projection radiography, it is only possible to estimate the reverse shock front velocity by imaging a time sequence of shock development over many individual shots. Given that the backlighter beams can be triggered at different times relative to the laser pulse on the main experimental target, it is possible to choose the Δt

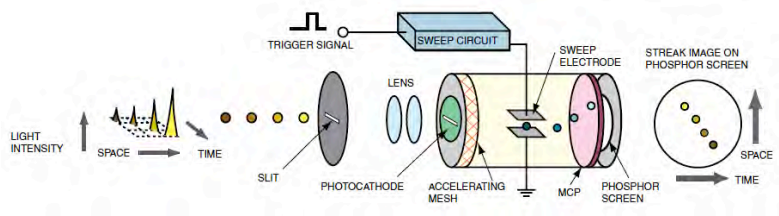

Figure 4.12: Cartoon of general streak camera setup.

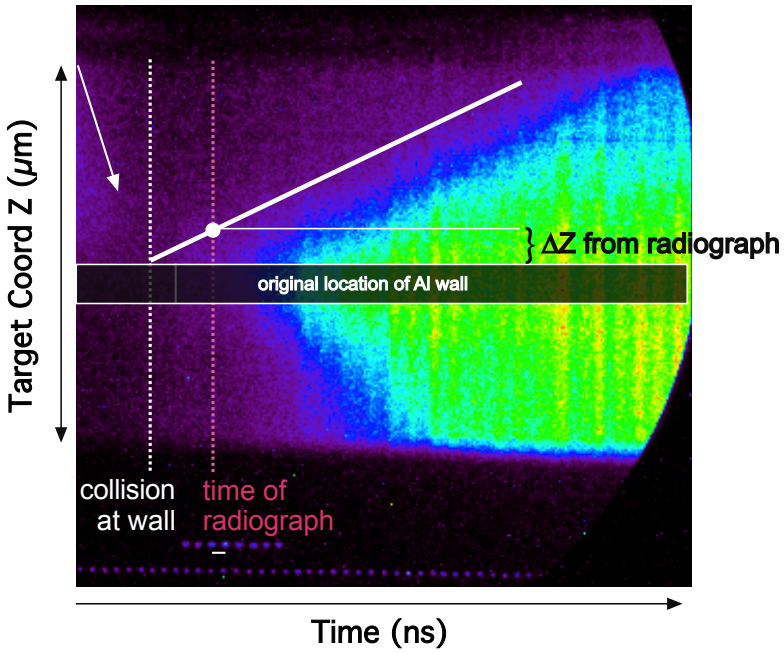

Figure 4.13: Time vs optical emission of roughly 1.0 mm at the end of the target body.

between radiographs. Figure 4.11 shows two Sn shots 5 ns apart. Figure 4.11(a), the same image discussed above, has the shock front location at Z = -150 μm, where Z = 0 is the initial wall position. Figure 4.11(b), shows Z = -237 μm for the shock position near the center of the image over a 250 μm window. This suggests an average velocity of $\sim$ 17 μm/ns. Given that the x-ray source is on for about 1 ns, any motion blurring should be under the resolution limit of the radiograph of 20 μm. Potential variations, including laser energy, target alignment and target alone from shot to shot provide uncertainty in shock position. These data were compared with data taken from the streaked optical pyrometer (SOP) discussed in Chapter III.

SOP records self-emission in the visible wavelengths from a 1 mm slice of the target along the axis of flow in $\hat{Z}$ direction and centered on Al wall, as was shown in Figure 3.6. This emission is processed by a streak camera, producing 1D spatial data resolved in time. A cartoon of this general process is shown in Figure 4.12. This output provides velocity data for an emitting region in the plane perpendicular to

diagnostic line of sight. The orientation of slit determines the spatial direction. Due to design of the target chamber at the Omega facility, the plane perpendicular to the line of sight of SOP has to be the same as a radiograph. Therefore while using SOP, only one radiograph is produced. Figure 4.13 shows raw data from the first experimental campaign. The vertical dimension is space and the horizontal dimension is time. The incoming flow is seen in the top left part of the image, along the thin diagonal white arrow. It impacts the wall (or wall material) at the time represented by the white dotted line and the shock forms. The red dotted line shows the timing of the corresponding radiograph for this shot. The circle represent the measured shock front distance from the wall on the radiograph. By drawing an estimated profile for the shock starting at the wall at the time of collision through the measured data, the slope of the white line would estimate a linear shock velocity. There is good agreement with the velocity of the optical emission region behind it. Over multiple shots, the average linear velocity ranged from 16 μm/ns to 25 μm/ns, within which the velocity calculated from the radiographic time sequence falls.

CHAPTER V

Oblique Radiative Reverse Shocks

Creating the radiative reverse shock was a proof-of-principle experiment. The nature of high-energy-density experiments as well as other applied research is to establish an experimental platform off of which one can build. While the normal-incidence reverse shock wave experiments have multiple avenues to still consider, some of which are discussed in Chapter VI, they are the starting point for developing a better laboratory astrophysics experiment. In attempt to move closer to conditions relevant to the cataclysmic variable, the first improvement to the experimental system was to make the flow obliquely collide with the wall. Astrophysical theory suggests a range of angles at the collision region none of which are 90 degrees [73]. Recalling the details of RLOF, as mass moves across L1 it is diverted [59]. Many of the astrophysical simulations mentioned in Chapter I chose $\beta = 60$ degrees at the stream-disk collision, where β is defined in the Figure 5.1. The motivation for the hot spot comparison still lies in understanding the dynamics in the shock system, or how mass moves into the accretion disk. This chapter details the progress of implementing oblique collisions with the experimental target and simulations for comparison. As with the target having a collision at normal incidence (henceforth known as the "normal target"), the first attempt had design flaws that affected the data in an undesirable way. Both this target and the data from it will be discussed. Next, a second target

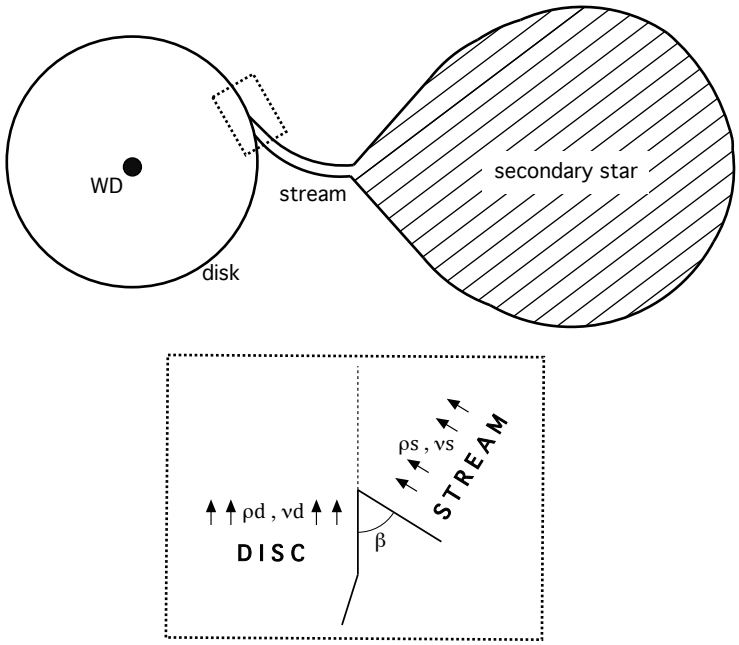

Figure 5.1: (*top*) General schematic of CV orbital plane, with dashed rectangle highlighting the 'hot spot' area of interest. (*bottom*) Basic geometry of stream-disk interaction where β is the angle between them at the collision.

construction is introduced. Before its data is presented, some details about oblique radiative shocks physics are reviewed. Simulations of the second experimental target suggest that a downstream shear flow may produce unstable growth. The latter half of this chapter discusses the experimental simulation data in the context of possible Kelvin-Helmholtz-like vortex growth. It concludes with the experimental data that may support the idea of vortex growth.

5.1 Oblique "strip" target

The evolution of the oblique collision target (henceforth known as the "oblique target") was similar to that of the normal target. The first attempt at producing an oblique reverse shock occurred at the end of a campaign day that shot the normal "strip" targets, discussed in Chapter III. The term "strip" in the context of this target design refers to the fact that the non-cylindrically symmetric Al obstacle did not cover the entire cross-sectional area of the milled acrylic. Although this remained

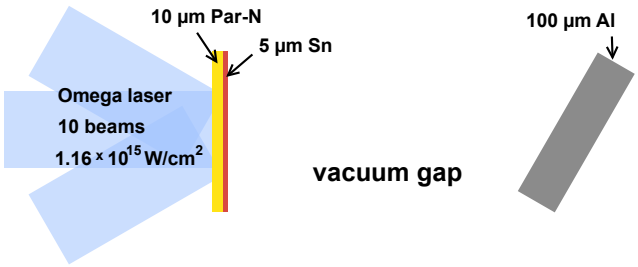

(a) Basic components needed for the oblique radiative reverse shock experiment.

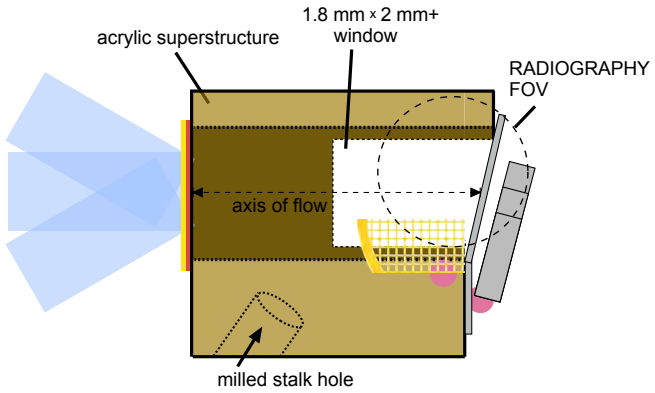

(b) View of $\hat{Y}$-$\hat{Z}$ plane

Figure 5.2: (a) Three foils that create the oblique reverse shock experiment. This basic design shows the similarly to the normal target case with only one rotational change. (b) The first attempted oblique target body from the perspective of the single x-ray radiographic line of sight. As is convention, blue rays represent the laser coming from the left which irradiate the drive foils, shown in yellow and red. All pink dots are glue. The conical shield around the laser spot is not shown.

true for the final target design, the "strip" designation was attached to the earlier target design and for ease of explanation, the same convention is maintained here.

Figure 5.2(b) shows the single radiographic view of the oblique strip target. Similar to the normal strip target, it consists of a 4.3 mm × 3.2 mm × 4.0 mm acrylic block superstructure, that has a 2 mm diameter (and 4.0 mm length) cylinder milled into it. A 1.8 mm × 3.2 mm × 2 mm window is cut out of the structure across which the Al foil is placed. In order to tilt it, the thinner edge of acyrlic extends past the 4.0 mm length of the rest of the target. Therefore the Al strip is attached across the uneven walls such that the angle off of normal is ∼12 degrees.

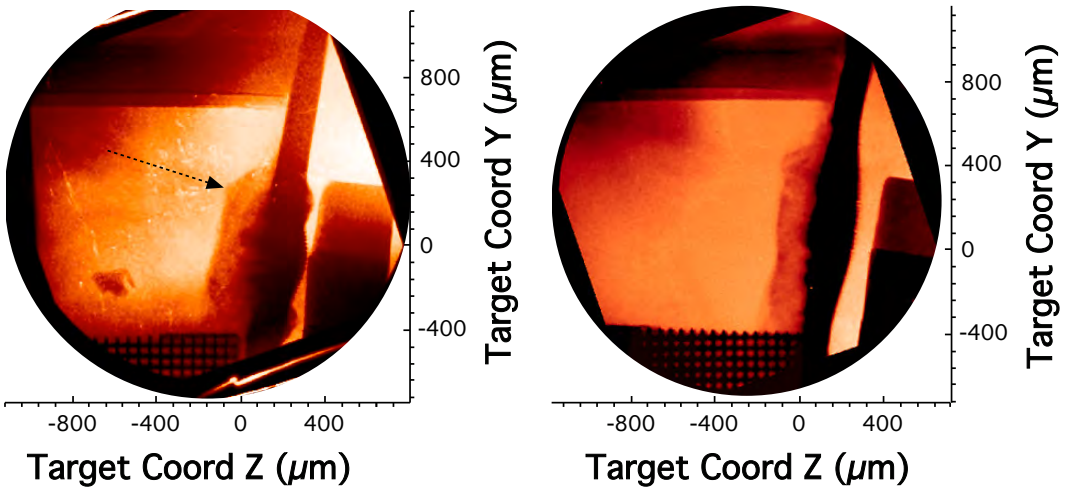

(a) Reverse shock in Sn with a 6 μm ablator (b) Reverse shock in Sn with a 10 μm ablator

Figure 5.3: Two radiographs of the oblique shocks in Sn in the presence of wall effects. The arrow in the left image points to what would be the point of interaction in the case of wall shocks.

5.1.1 Wall effects

Figure 5.3(a) and Figure 5.3(b) show radiographic images from two different oblique strip target shots imaged at different times. The acrylic wall can be seen at the top of the images, while the opposite edge is just blocked by the Au fiducial grid at the bottom. The x-ray calibrating step wedge can also be seen to the right of the Al obstacle. In each of these radiographic images the upstream flow is moving left to right and the reverse shock is just right of center. The radiographs both show a pinched radiative reverse oblique shock. The word "pinched" is used here to describe the fact that the lateral extent of the shock does not reach the walls despite the fact that the Al spans the entire $\hat{Y}$ direction. It is evident that some radial pressure source exists.

There has been a quite a bit of work done on understanding wall shocks in the driven radiative shock experiments discussed in Chapter I. The term wall shock refers to a secondary, radially converging shock initiatied at the target walls. In the driven case, the radiative shock is moving in the laboratory frame upwards of 100 μm/ns and

radiation flux from the front is heating the shock tube walls in front of it [25]. This flux ablates a layer from the wall creating an oblique polytropic shock that in turn sets up interesting shock interactions [23]. It is plausible that for the experiments seen in Figure 5.3, similar shock interactions could occur at the edges of the reverse shock. However, based on dynamic timescales, the wall shocks would not be created by the radiative flux from the reverse shock. It can be seen that the pinching, or $\hat{Y}$ height reduction, of the shock grows in time over radiographs. This suggests that the velocity of the wall shock, u_{ws}, is greater than u_{rs}, the velocity of the reverse shock. Two possible explanations for this are preheat [51, 50] and flow interaction with the wall. The effect may be the same in either case. Strong enough radiative preheat that reaches the acrylic walls could ablate material and drive a shock towards the axis of flow. This would work to confine the flow closer to axis. Similarly low density edges of the expanding Sn that reach the target walls may create rebounding shocks. Based on the corners of the reverse shock, denoted with an arrow in Figure 5.3(a), it is possible that some wall shock intersects with the reverse shock resulting in the deflected edge of the radiative reverse shock. These wall effects were also seen in normal collisions, but the impetus for changing the target design was to allow the stream to move in all directions for the oblique target.

5.2 "Leg" Target

Considering the astrophysical motivation, a primary objective was to monitor how or if the flow was deflected. Some astrophysical code simulations suggest that it is deflected up over the height of the disk [42] while others discuss the deflect along the motion of the turning accretion disk [3]. Given the strip design, deflected motion would be limited to the corresponding $\hat{X}$ direction (along the 1 mm dimension of Al) because of the location of the walls, discussed in the last section. Unfortunately, any deflection or motion around the Al strip in the $\hat{X}$ direction is not plausible to

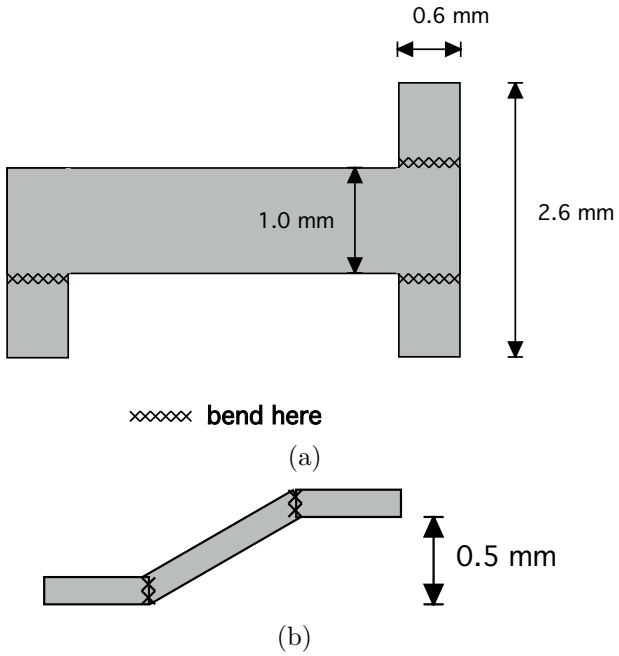

Figure 5.4: Two views of the Al obstacle that is used in the final 'leg' target design.

accurately diagnose given the single radiographic view. This diverted flow would be into or out the plane of the radiograph. Aside from the acrylic wall that would occlude radiography in the orthogonal view, a tilted Al strip means the orthogonal line of sight would not be edge on to the reverse shock. Therefore dual radiography was never attempted on any oblique target shots.

The updated oblique target again mirrors the evolution of the normal target. The drive foil is still attached to one side of an evacuated 2 mm diameter cylinder. The tube is milled out of a 4.3 mm $\times$ 3.2 mm $\times$ 2 mm acrylic block that has additional extensions or "legs" from three of the corners along the 2 mm height of block. These acrylic extensions provide attachment points for the Al obstacle. In order to tilt the obstacle, one of the legs has to differ in height. This height difference determines the angle of the oblique collision. Due to the fact that the legs are radially far from the central tube axis (by design), attaching a planar foil across them would require a significant height difference to reach larger angles such as 30°. (30° corresponds to a $\beta = 60°$ in Figure 5.1.) Machining acrylic legs longer that ~ 2 mm compromised their

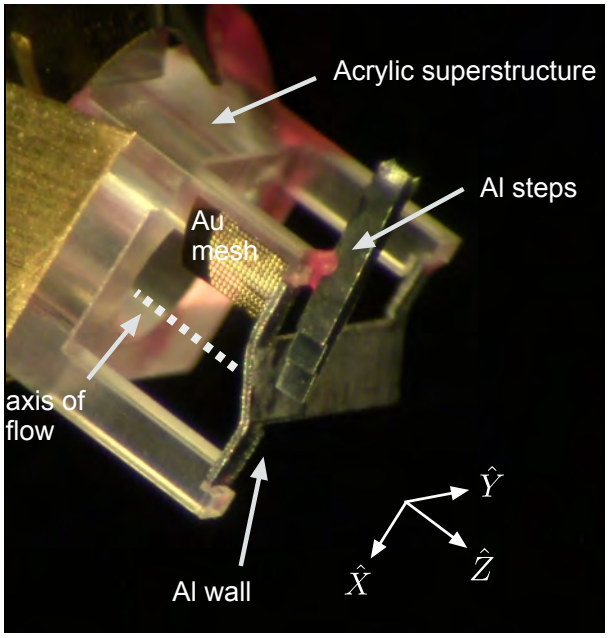

Figure 5.5: Target perspective is such that the laser ablation spot cannot be seen. The acrylic face holding the CH/Sn foil is tilted into the page and surrounded by Au conical shielding. The end of the milled cylinder through which the Sn flows can be seen. Sn plasma flows down the cylindrical axis (shown by the dotted line) towards the Al obstacle. The pink dots are glue. Al fits into counterbore still and butt right up against it.

sturdiness. In an effort to not add more mass for a larger target superstructure, the Al strip was designed such that parts of it bent. This can be seen in Figure 5.4. Given this design, the 4.0 mm length of the flow axis can be maintained without extending the legs too far. An image of the built target can be seen in Figure 5.5.

The fourth potential extension to the structure is nonexistent so that the line of sight of the soft x-ray spectrometer, μDMX, will not be blocked. Unfortunately, this current design structure was not sturdy enough and warping occurred. The foil became tilted with respect to the $\hat{X}$-$\hat{Z}$ plane. This was noticed during final characterization and also seen in the data, which will be shown later in this chapter.

5.3 Deflected Flow

With this design, the Sn flow will still move along the cylindrical axis, and impact the tilted Al wall about 4 mm away from the laser spot, as measured on the axis. Because of the design, some Sn will reach the tilted Al closer than 4 mm (in the -$\hat{X}$ direction). The interaction at the Al occurs within a ∼1.0 mm by ∼2.0 mm area of the strip. Now the single radiographic view is in the $\hat{X}$-$\hat{Z}$ plane, such that the 1.0 mm height of the Al can be seen in the data image. Therefore any deflection or motion around the Al strip in the $\hat{X}$ direction will be seen. Some theory of oblique shock waves provides insight into the cause of the deflections that were seen in the data.

Using the conservation equations across a shock (Equation 2.3), a simple derivation shows that the upstream velocity is bent away from the normal as it crosses the shock [28]. The normal velocity decreases but the transverse velocity does not, and this is the consequence. In other words, the shocked flow will be diverted by some angle θ, as shown in Figure 5.6(a). For a non-radiative or polytropic oblique shock, the system is usually described completely in terms Mach number and angle of incidence of the upstream flow, β. The description of an oblique shock changes however when the shock becomes radiative.

Something not discussed in the analytic evaluation of Chapter II (where the upstream pressure was neglected) is the difference in ionization, Z, across the radiative shock front. Doss et al. evaluates this in detail for a radiative shock system [23] with similar parameters to the experiments presented in this thesis. Some of their findings will be presented here. The first is the atypical behavior of the ionization being lower across the shock, which leads to the necessary caveat for understanding the oblique radiative shock.

A counterintuitive consequence of the ionization lowering in radiative shocks is that the sound speed will also decrease across the shock wave. In other words, the sound speed, $c = \sqrt{\gamma R(1+Z)T}$, will be less in the shocked material than in the

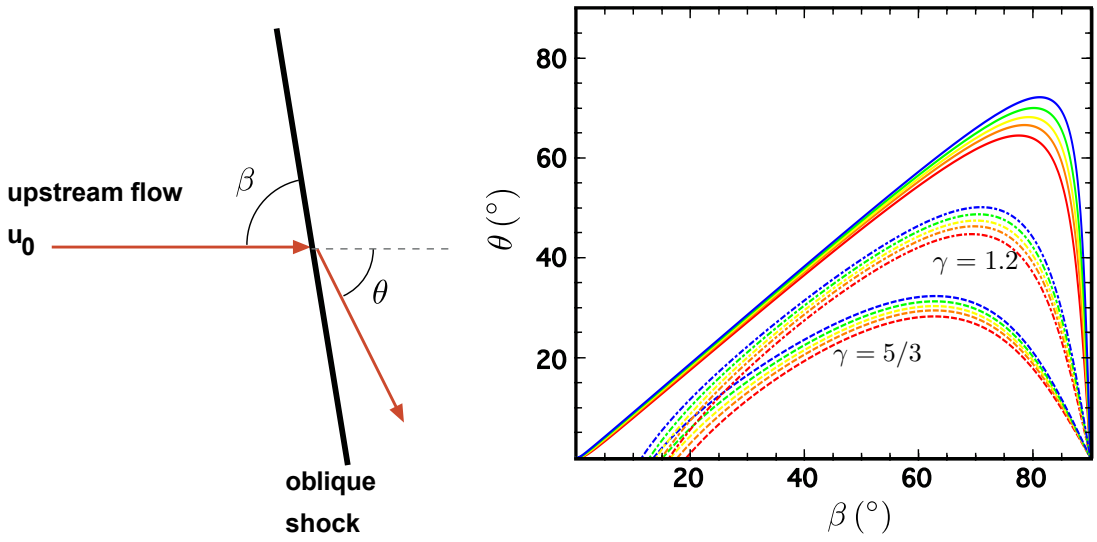

(a) Properties of an oblique shock wave

(b) Deflected flow plots

Figure 5.6: (a) In an oblique shock, the shocked flow will be diverted by some angle θ which can be described in part by β. (b) Solid lines represent the angle of deflection possible across an oblique shock when it is radiative. The colors correspond to a value for velocity where $u_0 = 80$ (red), 100 (orange), 120 (yellow), 150 (green), 200 μm/ns (blue). The dashed paths represent polytropic shocks with $\gamma = 1.2$ and 5/3.

upstream flow. It decreases by a factor of $\sqrt{(1+Z_f)(1+Z_0)}$ and will not vary simply at different angles. Therefore describing the oblique shock system in terms Mach number is no longer accurate, as it will also not vary simply at different angles. Instead upstream flow velocity, u_0, is considered.

Doss et al. shows that the angular deflection of flow through a oblique radiative shock is

$$\theta = tan^{-1}\left(\frac{(1-\eta)tan(\beta)}{\eta tan^2(\beta)+1}\right) \tag{5.1}$$

where η is the inverse compression ratio ρ_0/ρ_f, θ and β are defined in Figure 5.7, and the total post-shock velocity is

$$u_2 = u_1\sqrt{\eta^2 sin^2(\beta) + cos^2(\beta)} \tag{5.2}$$

assuming that strong radiation transport will equilibrate the final temperature of the

downstream fluid with that of the upstream fluid [28]. Given a high compression for a radiative shock, Equation 5.1 reveals that the radiative oblique shock has far higher maximum flow deflection than the non-radiative shock. Assuming the experimental parameter $\rho = 0.005$ g/cm^3 for an oblique reverse shock in Sn, this deflection given a range of flow velocities is plotted in Figure 5.6(b).

The solid color set of lines is the flow deflection in a radiative system for $u_0 =$ 80 (red), 100 (orange), 120 (yellow), 150 (green), 200 μm/ns (blue). These can be compared to the lines for non-radiative shocks where $\gamma = 1.2$ (dot-dashed) and $\gamma = 5/3$ (dashed) and Mach numbers consistent with the respective velocity. It is worth noting that in actuality, the radiative shock solution would approach the polytropic solution at low values of β where the normal component of the flow would be sufficiently slow, although this is not represented in the plot. Given a $\beta = 68°$ based on the target design and measurements of shock location in radiographs, the deflection θ ranges from $60°$ to $64°$ for the different flow velocities in the radiative case. Considering these and the experimental setup for the oblique targets, Figure 5.7 represents the radiative reverse oblique shock system. The original position of the Al wall is shown by the gray rectangle. The incident flow is from left creating a reverse shock and deflected flow that can move roughly parallel to the deflected Al wall surface. The Al here would be nearly static, and a shear layer with the high Mach number downstream Sn flow would be created. For clarity, a shear layer is defined as the transition region where velocity changes quickly in magnitude but remains long the same axis.

5.4 The potential for unstable growth

2D CRASH simulations of the experiment (discussed below) illustrate this supersonic shear layer in the reverse shock system. They also, however, show the growth of Kelvin-Helmholtz-like vortices. Kelvin-Helmholtz (KH) is an instability that occurs when two fluid regions flow past one another, with a sufficiently narrow transition

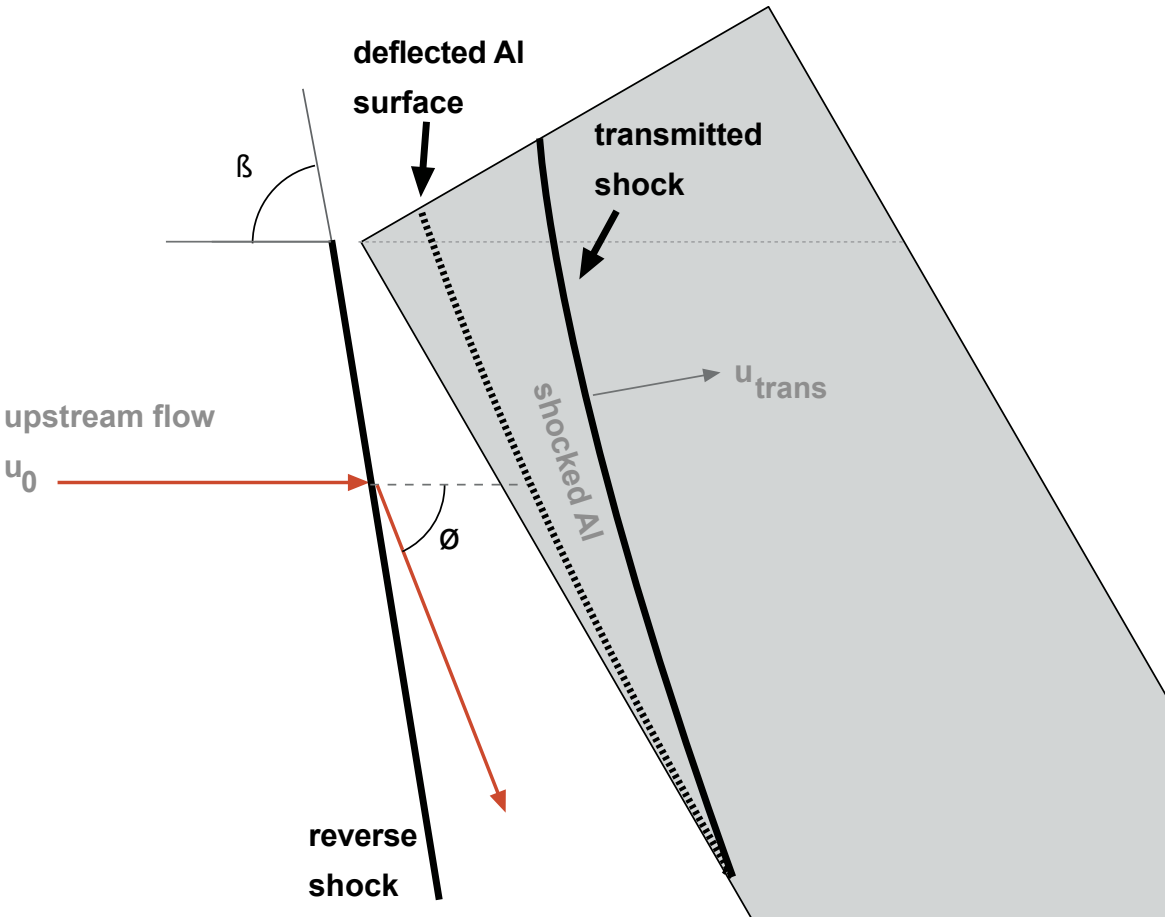

Figure 5.7: Basic geometry of the two shock system in the experiment. The gray block represents the Al wall and the upstream flow comes in from the left.

region at their mutual boundary, fluctuations at the boundary are unstable and will grow [28]. The small fluctuations on the shear layer grow into vortices and are often referred to as roll-ups. Many studies have been devoted to understanding the behavior of this instability under the influence of different physical constraints or typical of different environments. It is of particular interest in astrophysics where shear flows occur often. In considering Kelvin-Helmholtz in this experimental system, compressible effects [17], finite layer depth [2], and possibly radiative effects [9] would play a role in its growth. Only the potential radiative effects are considered below.

5.4.1 2D CRASH simulations of oblique target

A 2D CRASH model of the full oblique target was simulated and can be seen in Figure 5.8-Figure 5.10(c). The simulation is done in a cartesian coordinate system because it is not axially symmetric as a result of the tilted Al obstacle. The simulation was initialized from the results of another simulation of laser energy deposition in the system using the H2D code, which can be seen on the left where the drive foil has already been irradiated. Figure 5.8 shows the initial setup of the simulation where t = 0 corresponds to the time immediately after the laser pulse has finished.

The direction of the Sn flow along the cylindrical axis is the $\hat{Z}$-direction, while the lateral direction is referred to as the $\hat{X}$-direction here. The red blocks on the left side of the frame are the 2.0 mm long acrylic target body with cylindrical target axis removed from the center. The tilted Al wall can be seen on the right. Neither the acrylic or Al extensions holding the tilted foil are included as they should be far from the area of interaction. Out of ease, the Al is tilted to 45° in the simulation, while the experiments were tilted only up to 30°. Also due to the fact that vacuum cannot be implemented in the numerical simulation, the dark blue background is very low density plastic. Figure 5.9 shows the initial contact between the Sn flow and the Al at t = 31 ns. The collimation effects of the acrylic target walls can be seen. Small

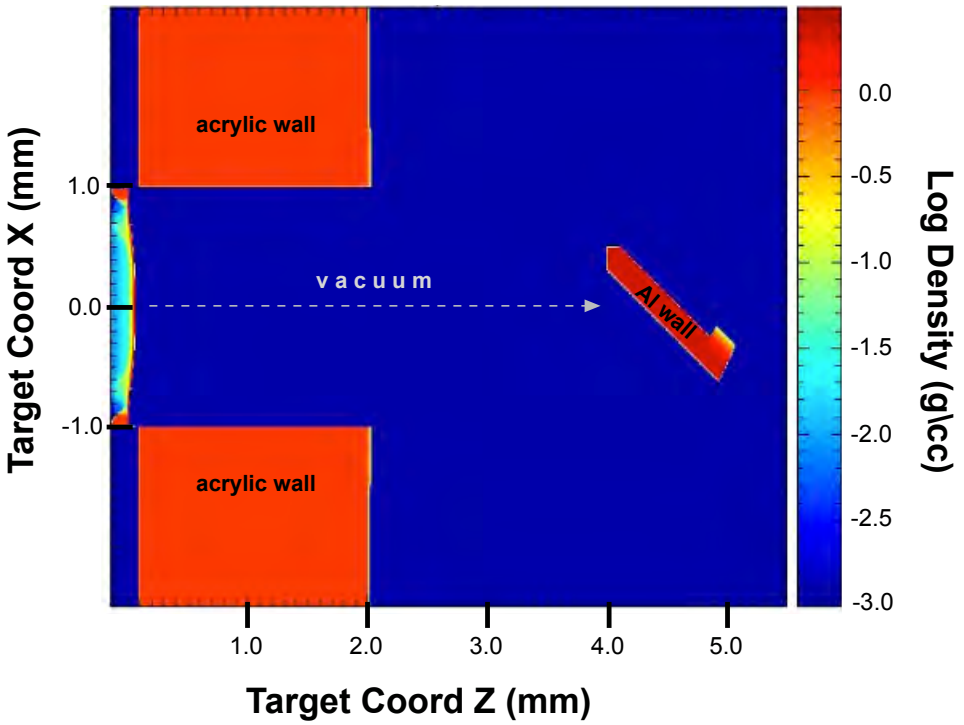

Figure 5.8: Initial frame of oblique target 2D CRASH simulation.

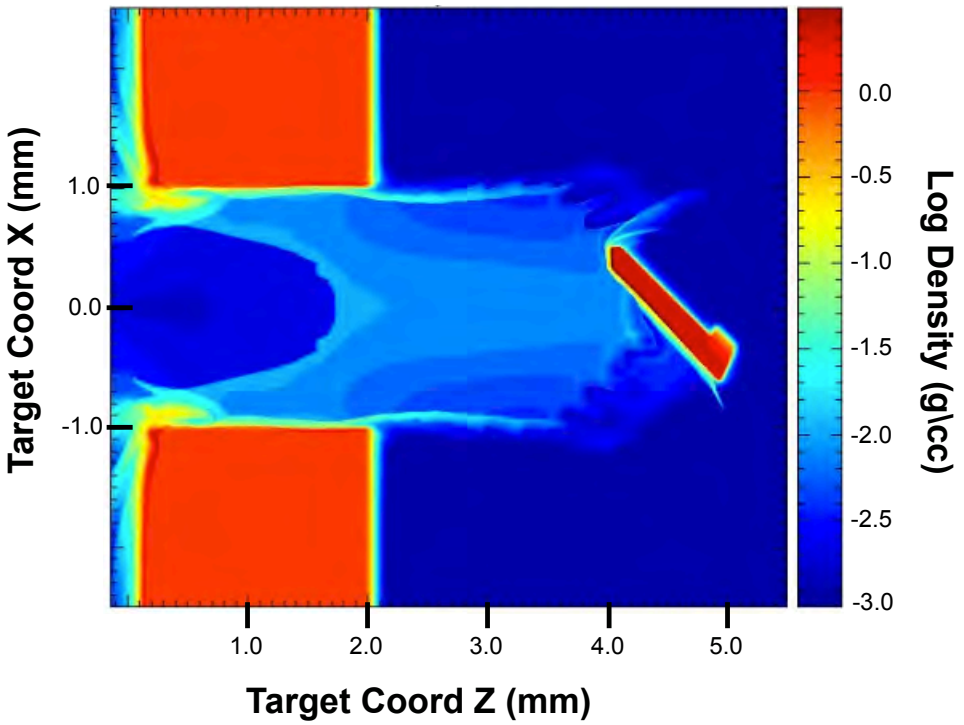

Figure 5.9: Initial collision of Sn flow in the oblique target 2D CRASH simulation.

dense layers at the vertical extents of the flow are due to rebounding shear motion with the acrylic wall. At the point of collision, early Sn is compressed against the Al wall.

As Sn continues to move down axis, one can see the shock form against the obstacle and then rebound into thin dense layer. The shear layer is also created and perturbation growth starts at roughly t = 33 ns. Parameters taken from the simulation show 80 μm/ns velocity in the direction of the shear flow which can be seen in Figure 5.10. This figure shows the evolution of the vortex growth in three time steps. The vortices are most clearly seen in the velocity plots.

Looking particularly at the two most well-formed vortices, a time sequence of perturbation amplitude was extracted. This information is plotted in Figure 5.11 for each vortex, where h is the peak to valley amplitude, λ is the perturbation wavelength, ΔU is the shear velocity, and t is time. For the purpose of comparing growth rates, a simple shear problem with a periodic perturbation was simulated in the supersonic regime with an imposed condition of radiation temperature similar to that seen in the experimental target simulation. Wavelength and initial amplitude were also chosen to be comparable to the experimental simulation values. The results from this secondary simulation are also plotted in Figure 5.11 to the far left and then fitted to a curve for the entire domain.

For the simple shear problem, the simulation produced perturbations that were standing structures locally increasing their amplitude. In the experimental case, there are traveling perturbations. While this may contribute to some error in extracting data, Figure 5.11 shows fairly different profiles between the two simulations. Modeling a more complete comparison, with characteristics such as finite layer depth, could offer more insight. Although the growth rate of the simple case doesn't well describe the experimental case, it does show an interesting result for Kelvin-Helmholtz theory. Traditional KH theory addressing compressibility effects on linear growth rate

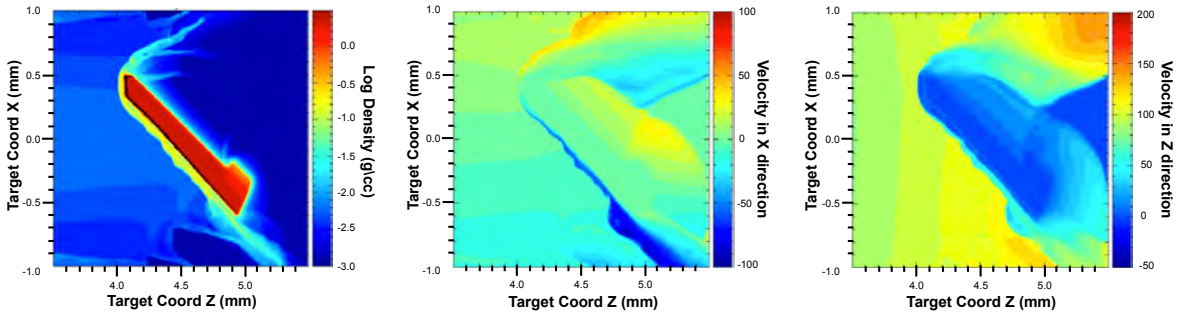

(a) Simulation at T = 40 ns

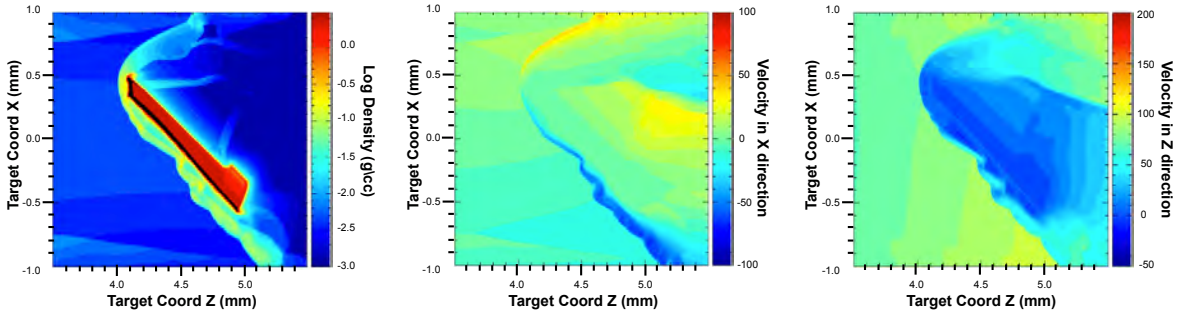

(b) Simulation at T = 49 ns

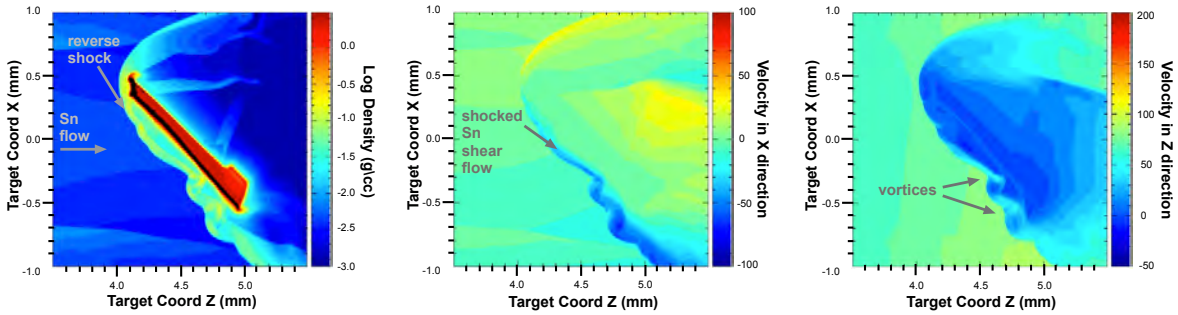

(c) Simulation at T = 53 ns

Figure 5.10: Three frames of CRASH simulation for oblique target, zoomed to region of collision. The columns represents the density, velocity in the vertical ($\hat{X}$) direction, and velocity in the horizontal ($\hat{Z}$) direction, respectively. Frame times were chosen to show vortex growth evolution.

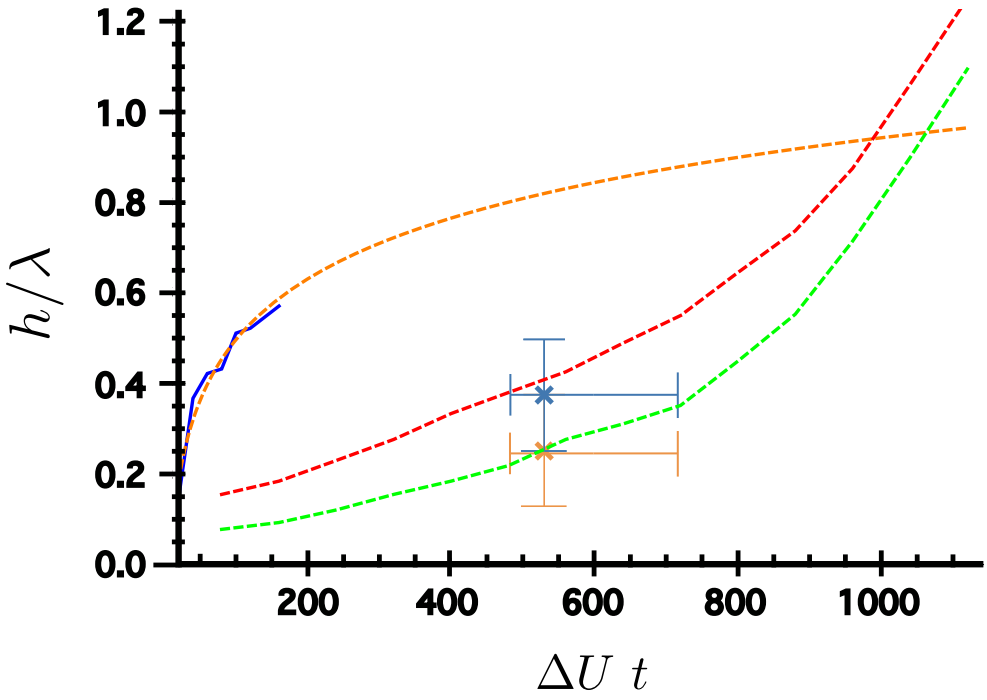

Figure 5.11: Ratio of perturbation height to wavelength λ plotted against the adjusted adjusted velocity difference.

suggests that for $M > 2\sqrt{2}$, the system will remain stable [17]. However, other work by Bodo et al. [9] suggests that this limit can be removed when radiative effects are present. It appears that the simple shear simulation demonstrates this, as [9] suggests comparable growth profiles. This result has spurred tangential computational work for high Mach number, radiation significant regimes and their effect on KH growth.

5.4.2 Experimental suggestions

This experimental target was shot only a few times, but the radiographs from these shots show some potential for agreement with experimental simulations. Figure 5.12 shows all of them in order of increasing time separation from the initial laser pulse, starting from the left. Figure 5.12(a) shows a zoomed section of the target where there appears to be stratified areas of material. Based on the density profiles from normal target shots, the length of the expanded Al is similar, around $\sim$100 μm. The Sn layer also shows some sinusoidal shape or fluctuation at the shock interface. The later time

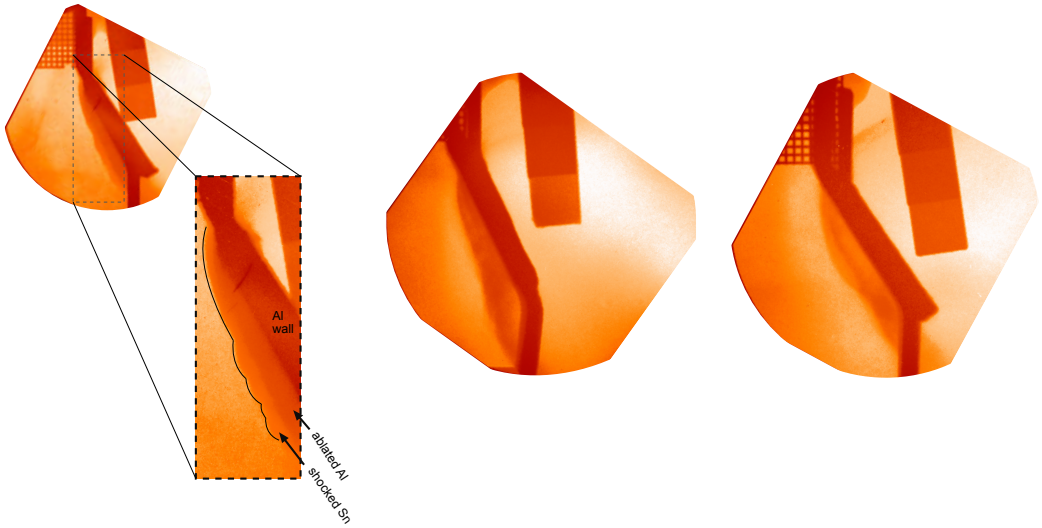

(a) Radiograph taken at T = 36 ns

(b) Radiograph taken at T = 40 ns

(c) Radiograph taken at T = 45 ns

Figure 5.12: Radiographs of 30° targets over 10 ns.

radiographs show interesting features as well. In the context of a KH roll-up in the simulation, the shape of the shock structure changes based on where the vortex is relative to the height of the wall. This also affects how the diverted shock flow moves at the bottom edge of the wall. In the Figure 5.12(b), the material appears to be arched near the bottom of the foil which if can be seen in the simulations above. In the Figure 5.12(c), there appears to be a clearly denser spot than anywhere else in the material structure almost in line with the foil's edge.

On the graph of Figure 5.11, two single data points were plotted from experimental data. These measurements were taken from the radiograph of Figure 5.12(a) and assumed an identical perturbation pattern at the internal boundary of the Sn with Al. The error bars shown on the plot express uncertainty in the length scale measurements from the radiograph data (for the vertical bar) and ±1 ns uncertainty in the time of radiograph relative to time of collision in addition to ±20 μm/ns for ambiguity of incoming flow velocity at that point, from which the shear velocity is calculated (for the horizontal). There is likely still uncertainty given the assumption

of similar interfaces and any target component tilt. As mentioned previously, some misalignment is noticeable in the radiographs. A clear example can be seen in Figure 5.12(c) where the two attachment wings of the Al are visible at the top center near the grid. The desired design with no tilt would expect those to be in the same line of sight. Overall, further advancements are needed to be made in the design of this target so that more data may address any potential vortex evolution.

5.4.3 Vorticity deposition

While the visual comparison of data and simulation is speculative, the experimental data spurred further simulations of the target set-up and steady regimes. A set of 2D simulations were completed that suggest the vortex growth is a product of vorticity deposition as opposed to true KH instability.

These additional simulations modeled a uniform, with respect to flow density, and steady flow (from a boundary condition) that impacts a tilted wall. These simulations were also made with comparable experimental values. The goal was to isolate any effect from the laser drive flow. The results tended to show the reverse shock system with no significant growth occurring until the density fluctuated. Considering this, it is likely that vorticity is being deposited at the shear layer. Further evaluation of the experimental simulation suggests that this may be observed during the initial compression of upstream flow at the oblique obstacle boundary. While this conclusion means the system isn't KH unstable, vorticity deposition is a real effect that will result in KH-like roll-ups as seen in the simulation and perhaps experimental data.

5.5 Implications for the CV and conclusions

The experimental data obtained during the course of this thesis work shows promising and interesting results for reverse radiative shocks. When considering the data application to the CV system, it is important to emphasize that only preliminary

conclusions can be drawn from the presented work. This is due to the finite mass and timescale of HED laser experiments and the many unknown parameter values of this system. The motivation for the hot spot comparison lies in understanding how stream mass moves with respect to the accretion disk. Thus, any conclusions focus on how shocked (and unshocked) Sn moves across the reverse shock. Preliminary analysis of the data presented in Chapter IV and this chapter would suggest that the stream could both overflow the disk height and be diverted around its edge with the potential existence of instability growth.

As specified in Chapter I, certain parameters were set with the target design. In the strip target design, the scale height ratio is defined as the ratio of the flow's vertical extent (or cylindrical diameter) over the height of the Al wall. Comparing this to the CV system, the Al obstacle can represent the disk such that the 1.0 mm length of the strip would correspond to the total height of the accretion disk. As discussed previously, the flow can expand radially such it will span 2.0 mm. In the normal-incidence case, a strongly radiative shock produces a bow shock type structure that could allow both unshocked and shocked stream material to move around the obstacle. This is similar to some astrophysical simulations [3] suggesting that efficient radiative cooling produces shocked material that is still a coherent stream moving around the obstacle.

The geometry comparison to the CV is not as simple for the oblique target case. In the CV system, the central (flow) axis of the stream is in the radial plane of the accretion disk, meaning that the center of the stream will collide with the middle of the accretion disk's height. This can be seen in Figure 1.4. The oblique angle of the collision is defined by the angle between the central axis of the stream and the radius of the accretion disk. If it was a normal collision, this angle would be 180°. In the normal-incidence experiment, the normal vector of Al wall (in the -$\hat{Z}$ direction) would represent the radius vector of the accretion disk. This is directly opposing the

axis of flow. With the oblique target, the normal vector of the Al is no longer in that same plane. Given this geometry, the 1.0 mm height of the Al wouldn't correspond nicely to the disk height.

Under this basic analysis, any movement around the tilted Al in the positive $\hat{X}$ direction isn't considered to have much meaning in comparison to the CV. However, any deflections in the -$\hat{X}$ direction can be thought to represent diverted flow around the disk's edge. There is clear evidence shown in this chapter that the stream material is diverted away from the obstacle as opposed to around it in the -$\hat{X}$ direction. With the suggestion of a shear flow, instabilities become a possibility. This is also observed in some astrophysical simulations under the consideration of efficient radiative cooling [73]. In order to make stronger comparisons to the CV, future research should focus on the interface between the shocked stream and the obstacle. Some specific suggestions are given in the next chapter.

CHAPTER VI

Conclusions and Future Directions

The work put forth in this thesis has shown the development of a new HEDLA experimental platform for radiative reverse shock waves. This includes substantiating the CV system as motivation with the potential for scaleable experimental data, presented in Chapter I. The theory of radiative reverse shocks is examined in Chapter II, where relations for the post-shock temperature, pressure, compression, as well as the initial (upstream) flow velocity, are derived as a function of the shock strength. The derivation considers the reverse shock to be formed in a fast moving upstream flow that is impeded by a wall, which summarizes the basic experiment. In Chapter III, the experimental process of creating both the flow and the collision is detailed by the target design. The target is configured for x-ray radiography, which is also discussed at length in the chapter, as a primary diagnostic technique. While both Chapters IV and V review experimental data with compelling comparison to 2D simulations, there are many details that should still be explored. The first section reviews all of the individual work that I accomplished in order to compose this manuscript. It is followed by some of my suggestions and outline of future experiments. It concludes with a summary of experimental findings.

6.1 Personal contributions

For the completion of the work described in this thesis, I preformed many tasks throughout the experimental process. This work was not a continuation of previous experimental efforts, however, it did implement various techniques, diagnostic and other, that have been used in laser-produced HED experiments. The idea for this work bore out of conversations that I had with a (computational) astrophysicist about various stellar systems that were of interest in the astrophysical community and largely unexplored. From the list of phenomena compiled from the discussions, I explored potential experimental design theory for each by running 1D HYADES simulations. From many 10s of simulations that I did, the radiative reverse shock seemed to be the most intriguing as well as potentially achievable.

Given the CV system, I derived the scaling presented in ChapterI. The ratio of accretion disk density to stream density and the ratio of disk scale height to stream scale height are physical parameters that distinguish the system. The Mach number of the flow characterizes the shock physics. The dimensionless parameter R_{rad} is similar to the Boltzmann number [64], and different variations of it have been used to characterize radiative shock waves [69, 27]. The cooling parameter, χ, is often used to describe radiation hydrodynamic systems. I took values from a collection of publications on stream-disk interactions to calculate the parameters for the hot spot region.

During the design of the target itself, I did more 1D and 2D HYADES simulations to probe the experiment for the most desirable parameters. In order to successfully create and diagnose a radiative reverse shock, a flow of enough material must be sustained moving fast enough into a shock wave to produce a radiative phase. For laser-driven HED experiments one limiting factor for the amount of mass involved in the fluid flow is the deposited laser energy on the target. The amount of mass limits the flow velocity. In turn, this dictates the time scale of the desired experimental

system conditions. I performed 1D simulations that tested various plastic ablator thicknesses as well as Sn thicknesses in order to drive the most desirable flow. I also ran numerous material simulations for both the drive foils and the obstacle to suggest a strongly radiating reverse shock.

In order to hold these foils in the target chamber and optimize diagnostic use, I designed the target in full. With each different campaign, I continued to adapt the target design to further optimize the experiment and data collection. A catalog of each design can be seen in Appendix A. I had some involvement in constructing the targets in the laboratory, and full responsibility for characterizing the completed targets. This requires extensive measurements to be taken under microscopes, holding the target with a motorized stage with micron-precision movement. These pre-shot measurements are necessary to calibrate the resulting x-ray radiographic images.

I was also responsible for the execution of the experiment at the Omega laser facility as the Principle Investigator (PI). This includes specifying all laser conditions and desired diagnostic setups. These specifications are shown in Appendix C. As the PI, I communicated with the facility staff to implement the experiment as changes are made throughout each campaign day. Changes to laser beam timing and diagnostic timing are often changed with every new target. I often made these decisions by looking at the data as it becomes available on a shot to shot basis, in order to collect the most complete set. After the experiment, I calibrated and analyzed the primary data in more depth, which is shown for both SOP and x-ray radiography in the previous chapters. The majority of my data analysis was done using a scientific programing language, IDL, and Java-based image processing program called ImageJ.

In order to compare data more extensive 2D simulations, I guided a few students and staff in the execution of the CRASH simulations shown in the previous chapters. This required that I detail the system for the simulation and then analyze the output. Many iterations of CRASH simulations were done in order to evolve the code output

to a more comparable representation of the experimental data based on my evaluations. I also guided CRASH simulations that were not shown but aimed to explore the production of the Kelvin-Helmholtz instability in similar regimes to that of my experiment. My analysis of one of these simulations is shown in the previous chapter.

Another contribution to note is my involvement in secondary experiments that attempted to characterize the background seen in the x-ray radiographs. I was responsible for these supplemental experiments testing backlighter target designs. This is presented in Chapter III with the designs shown in Appendix A. This data showed unexpected results given the addition of a thick acrylic frame to a backlighter target. It suggested that there is a definite high-energy bremsstrahlung contribution coming from the target with or without this additional shielding, and further work is being done to further characterize the spectrum. For these experiments, I contributed in the same way by running 1D simulations, designing the targets, characterizing the targets and overseeing the implementation at the Omega laser facility as PI.

6.2 Looking Forward

Overall, the ultimate advancement given present capabilities of this experiment would be to field it on a laser facility such as the National Ignition Facility (NIF) at Lawrence Livermore National Laboratory (LLNL) in Livermore, CA [40]. With 192 lasers, the facility can achieve > 1.6 MJ of UV light on millimeter scale targets. This would greatly increase the capability of creating a longer observable reverse shock by being able to drive more mass over a longer period of time. At the Omega laser, however, there are still many conceivable paths to explore. This section starts by considering potential diagnostic uses that could lead to a more complete description of the reverse shock system. This is followed by another subsection that suggests possible adaptations to the experimental design itself for the purpose of better accessing the astrophysical CV system. It concludes with comments regarding the compelling

physics of the oblique collision experiment and the continuing need for simulation as well.

6.2.1 Diagnostic potential

First and foremost, all experiments can benefit from being diagnosed in a more quantitative way. HED experimental platforms often have countless avenues to explore, but the success of those research avenues are limited by the existence or availability of different type of diagnostics. This experimental approach to radiative shocks opens many doors for experimental diagnostic use because the shock is relatively slow compared to the upstream material, and it is not encased in a shock tube. Two aspects of the system that with further characterization would greatly advance this work are the properties of the stream and a radiation temperature measurement.

While the process of creating a supersonic flow from the bilayer foil has been done previously [39, 32], there is little supported data about the stream other than average velocity. Simulations play a large part of estimating the properties during the expansion. A brief attempt to use Thomson scattering was made during this experimental work. Thomson scattering is a technique that probes the characteristics of a plasma with a coherent light source at a certain wavelength by collecting the scattered photons. This technique has the potential to give information about electron temperature, ion temperature, and electron density of the probed plasma. Because the target and laser were not optimized for this diagnostic, it did not have success on the shot day. However, the technique has the potential to be used because the stream is not fully enclosed in a target body. Understanding the temperature and ionization of the stream over the diagnosable time scale would not only provide a more complete comparison to radiative theory for early times but also a better understanding of the total shock evolution as density and velocity change at later times.

The second improvement for this experiment, radiation temperature measure-

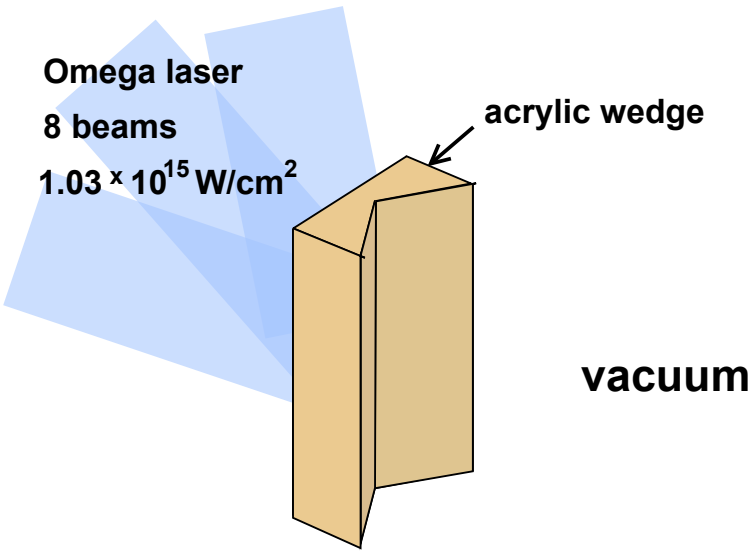

Figure 6.1: Basic schematic of plasma sheet target. Laser is incident on rear surface of machined acrylic wedge.

ments, was also attempted with the use of μDMX with incomplete results. 1D and 2D simulations predict the soft x-ray emission from the shocked material itself to be a few tens of eV. While some of the data collected during this thesis work supported this, there were inconsistent results that likely were affected by the acrylic target structure, and thus not detailed in this thesis. Targets were also not optimized fully for this diagnostic but showed the potential for promising results if they were in future experiments. This type of data would also improve understanding of the shock's radiative phase.

6.2.2 Astrophysical consideration

In an effort to continually move toward the CV system in the laboratory, there are a few relevant advancements that might be considered or are in the process. First, it would be ideal to have a second plasma flow to represent the accretion disk. The experimental challenge of maintaining scaled densities might be difficult, but the diagnosing of a two shock system seems more probable. The presence of the transmitted shock is only mentioned briefly in the context of simulations in this work. While

there will be a transmitted shock in the Al wall, the ability to diagnose it was not a priority or an option with radiography. The Al obstacle was too thick to achieve reasonable contrast for observing this shock. It will be opaque to achievable x-ray source energies used for point-projection radiography, as the conversion efficiency of laser energy to K-shell transitions falls off quickly with increasing atomic number. Some newly fielded experiments on the OMEGA laser aim to create a potential secondary flow by creating a plasma sheet. The basic target design is shown in Figure 6.1. The idea is to irradiate the back surface of a machined wedge shape to funnel the plasma flow onto the central axis, similar to how some experimental jets are formed [6]. If multiple beams irradiate down the spine of the v-shape, the idea is that the jet will be vertically extended into a sheet. Ongoing CRASH simulations support the development of this experiment as it was just implemented for the first time in May 2013. The ultimate goal would be to drive an extended flow as in the experiment presented in this thesis and have it collide with another, still denser, flow of the plasma sheet.

In addition to or perhaps in combination with secondary flow experiments, a simple target change may be made to evaluate dynamics at different scale heights. The experiment presented in this thesis was similar to the top image in Figure 6.2, where the ratio of the stream height to "disk" height was ~ 2. Testing a system where the height of the obstacle is greater than the vertical extent of the stream (as in the bottom image of the same figure) may provide insight for the questions of penetration depth in connection with dual shock formation.

6.2.3 Oblique collisions

As mentioned in the previous chapter, the most beneficial future direction for the oblique collision experiments is collecting more data with more structurally sound targets. Experimental observation was the motivating factor for this work to consider that there may be unstable Kelvin-Helmholtz-like growth and an effect due to radi-

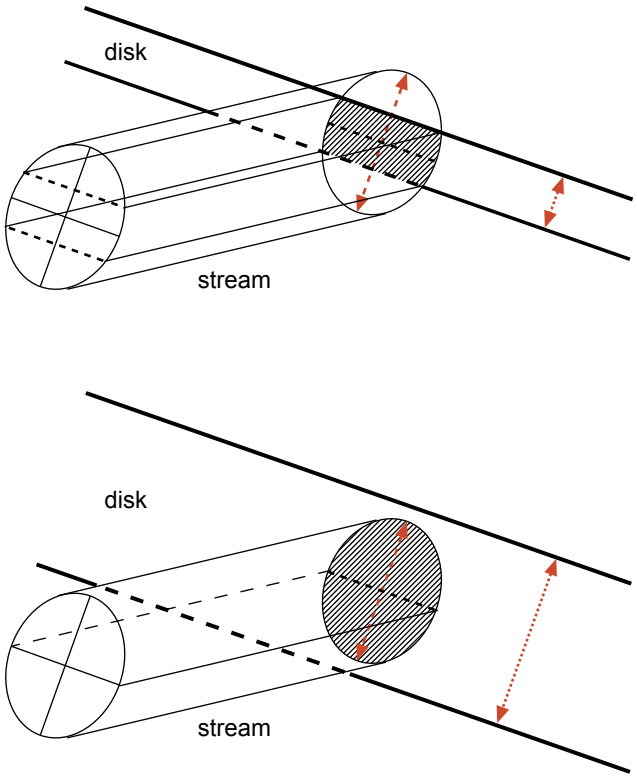

Figure 6.2: *(top)* Ratio of stream to obstacle scale height > 1, as in the present experiment, shows the possibility for stream material to overflow. *(bottom)* Ratio of stream to obstacle scale height < 1.

ation on that growth. 2D simulation work will be used on the immediate timescale to advance the theory and consideration of vortex growth. However, more and better imaging of the evolution of the material interface is needed to draw some supported conclusions. For this reason, the characterization of preheat may be a particularly useful to characterize here. The material in the shear layer is that which would experience the effects of the preheat the most, and it may play a role in seeding any unstable growth.

In combination with experimental simulation, there is a need for better astrophysical codes to simulate the hot spot system with a more accurate treatment of radiative cooling. Only very preliminary steps have been taken to achieve this with the AstroBEAR code [13] developed at the University of Rochester. This would give a more easily accessible or direct comparison of astrophysical system to experimental

system, and the question of instability formation might also be addressed.

6.3 Summary

This thesis has presented experiments that aim to address radiative reverse shock waves in the context of cataclysmic variable dynamics. The astrophysical process of accretion in a non-magnetic CV involves mass donation from a secondary star in a supersonic stream that impacts the edge of a disk formed around a white dwarf. Both astrophysical data and simulation suggest this is interaction has many ambiguities as a radiation hydrodynamic system. This led to the experimental platform in this thesis, where important non-dimensional physical parameters suggest that laboratory HED experiments may offer insight into the CV system.

There has been significant progress made over the course of this work in order to establish this experimental platform. The target was improved from each shot campaign to the next, attempting to best access the CV system under the limitations of laboratory work and diagnostic capability. The target specifications for each campaign are shown in Appendix A, including fabrication tolerances within which all targets are individually characterized prior to the experiment. This is necessary in order to spatially calibrate the resulting x-ray radiographic images produced on each shot. Appendix B shows a catalog of radiographs over each campaign, not presented in the main text. This includes discussion of experimental issues during the course of the shots. Appendix C shows the Omega laser facility details needed to execute each experiment, including the laser conditions and diagnostic specifications. These documents give the reader a complete overview of the facility's setup and full requirements for running the reverse shock campaigns. An additional experiment was completed in conjunction with this work to better characterize high energy background seen in radiographs and attempt to mitigate it. Although shielding techniques did not prove to be successful at decreasing the background, a thermal bremsstrahlung energy range

was found. The targets used in this campaign are also shown in Appendix A.

The reverse radiative shocks presented in this thesis started as a proof-of-principle experiment, in attempting to establish the new platform. The normal incidence collision has shown that a thin dense layer of radiatively-cooled material can be produced by driving a supersonic flow into a static (or nearly static) wall. The shock evolution is shown to be dependent on how radiative it is based on the initial post-shock material temperature. The formation of this shock can also be affected by the flow's interaction both with the sides of target superstructure and any preheated, expanded wall material. However, these conditions are not directly measured, so there is much experimental work that can be done. 1D and 2D simulations show qualitative agreement with formation and evolution of the reverse shock seen in the data under the various conditions.

When the collision is no longer normal incidence, the possibility for instability growth arises. An oblique shock will produce a diverted flow of shocked material than may act as a finite layer of shear motion. Simulations suggest that Kelvin-Helmholtz-like growth occurs at the shear interface with released Al from the obstacle. In order to make strong comparisons to the CV, future research should focus on this interface between the shocked stream and the obstacle. There is evidence in the current experimental data that could show similar growth to the simulations. Much more experimental data over various times is needed to explore this further.

APPENDICES

APPENDIX A

Target documents and specifications

This thesis assembles data taken at the Laboratory for Laser Energetics using the Omega-60 laser facility over four experimental campaigns: August 5, 2010; June 15, 2011; September 8, 2011; and July 19, 2012. Over the these four days, there have been 9 different main target bodies, 3 independent backlighter target configurations with 2 different backlighter metals, 4 types of drive foils, and 2 separate of obstacle materials. These numbers only apply to the experiments that were shot with the direct objective of contributing to this radiative reverse shock research. Every experimental day has additional targets that are not used and at least one target for outside objectives. This appendix categorizes the targets designs that were used on a given shot day. The campaign of September 2011 used similar targets to the June 2011 campaign so only documents for additional shielding and backlighters are shown.

A.1 August 5, 2010 - Type A: Bucket target

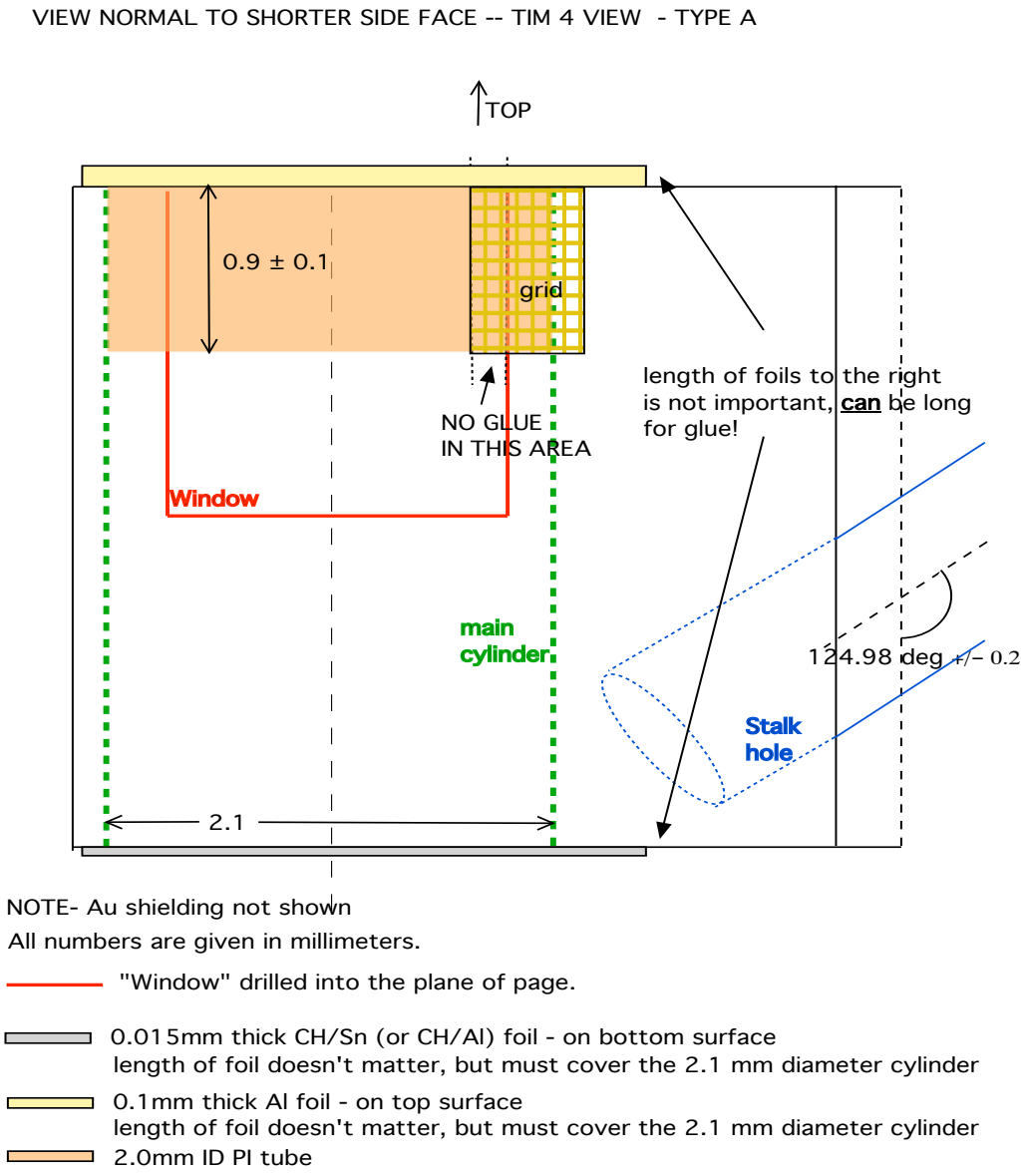

Figure A.1: Single view of radiography

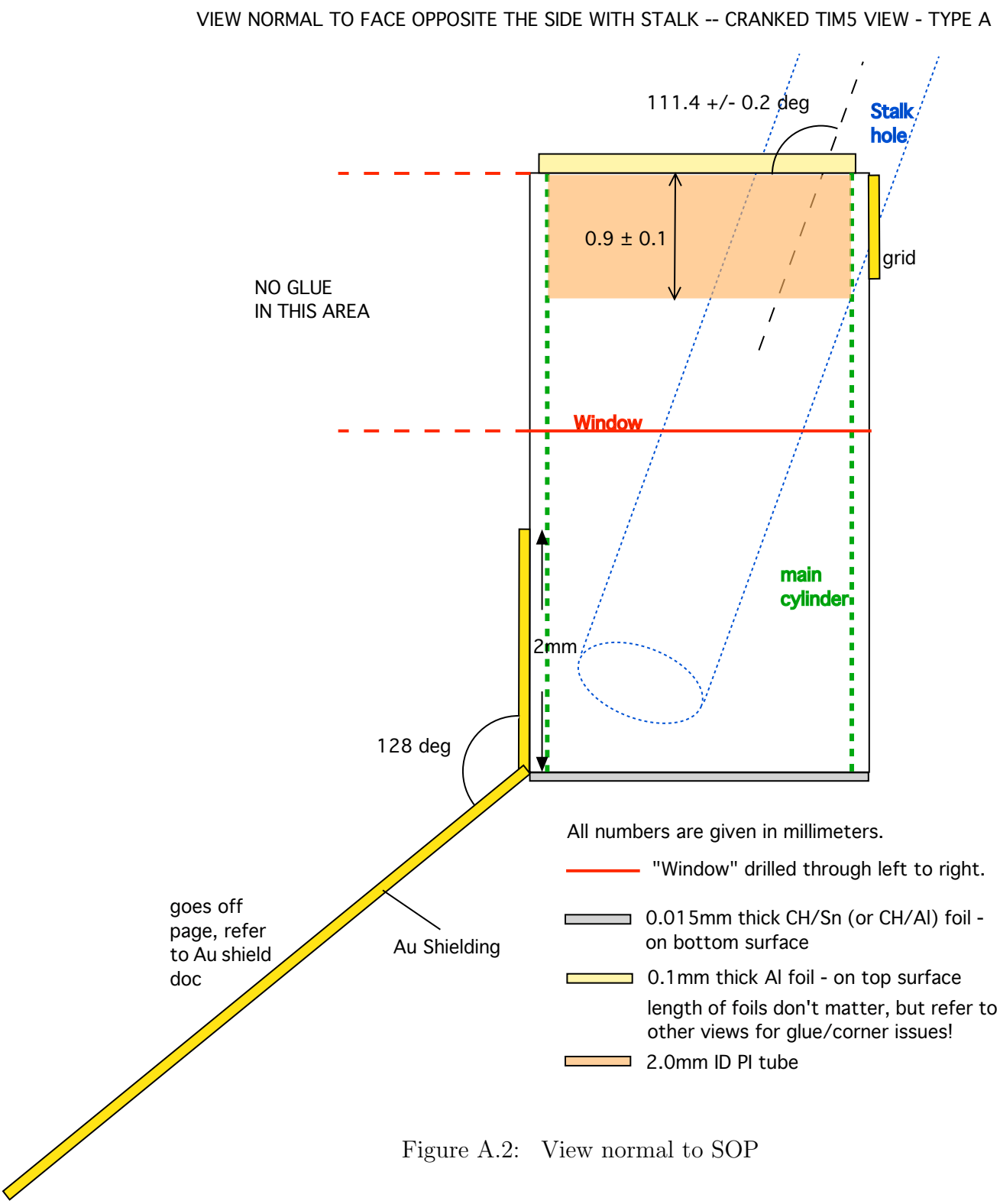

Figure A.2: View normal to SOP

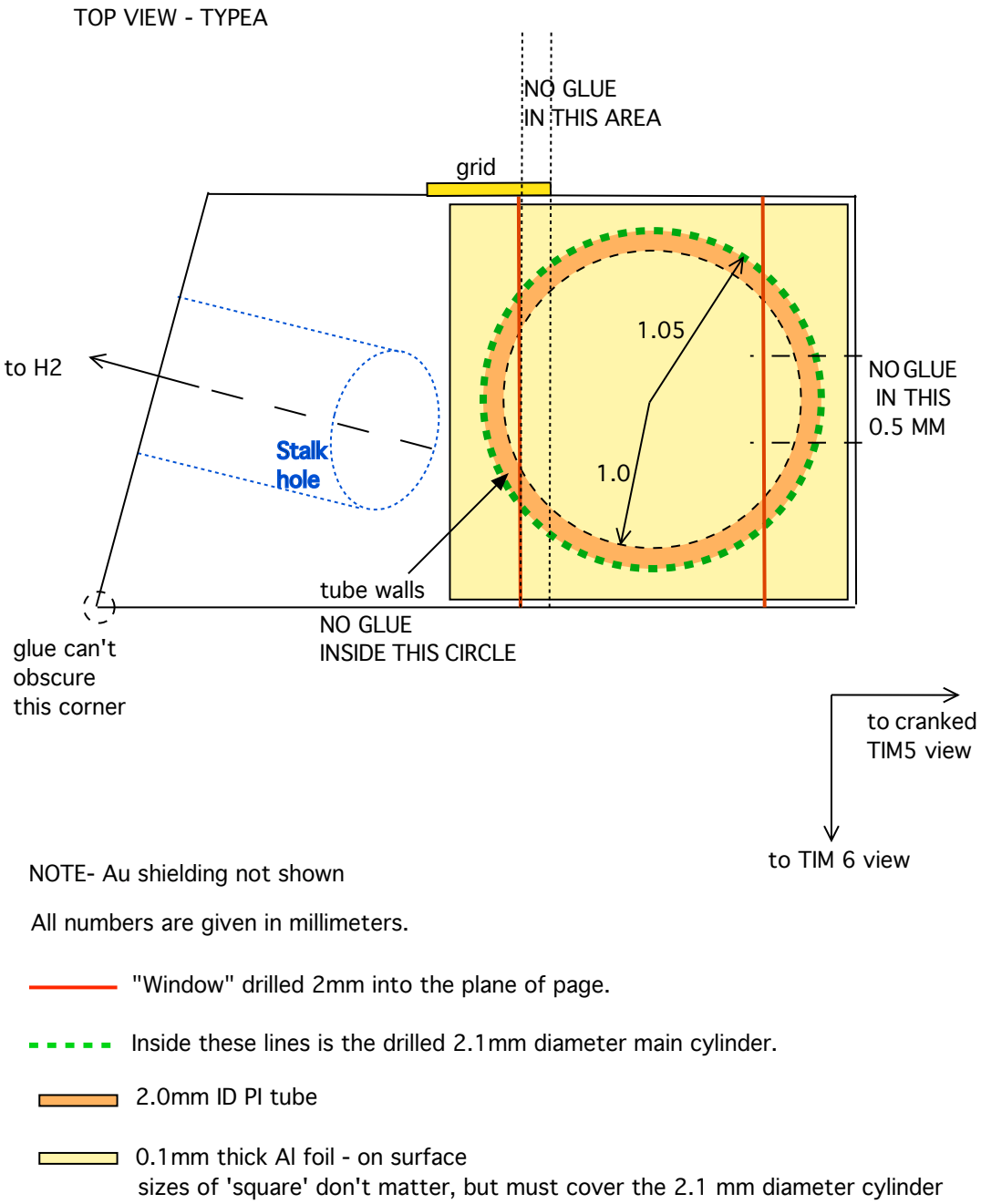

Figure A.3: View normal to Al wall

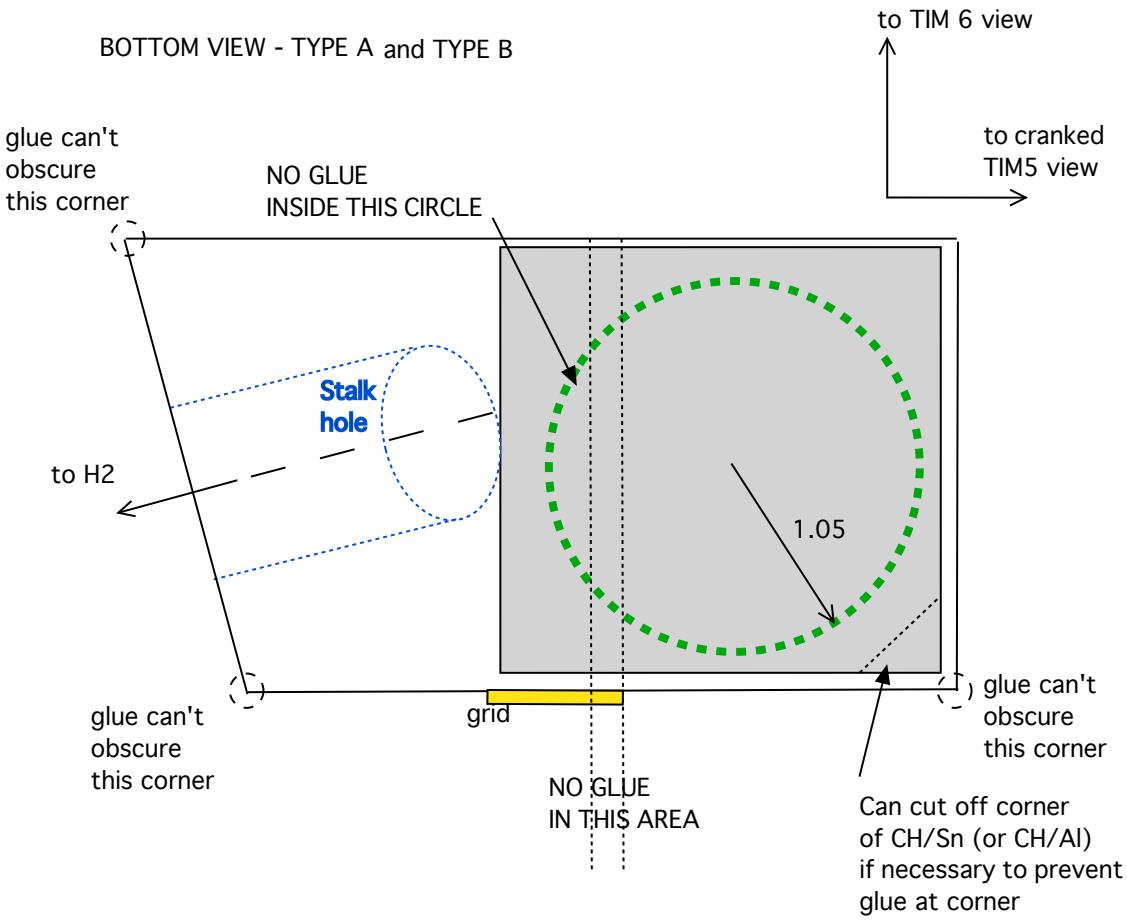

NOTE- Au shielding not shown

All numbers are given in millimeters.

"Window" drilled 2mm into the plane of page.

Inside these lines is the drilled 2.1mm diameter main cylinder.

0.015mm thick CH/Sn (or CH/Al) foil - on surface
sizes of 'square' don't matter, but must cover the 2.1 mm diameter cylinder

Figure A.4: View normal to drive foil

A.2 August 5, 2010 - Type B: Strip target

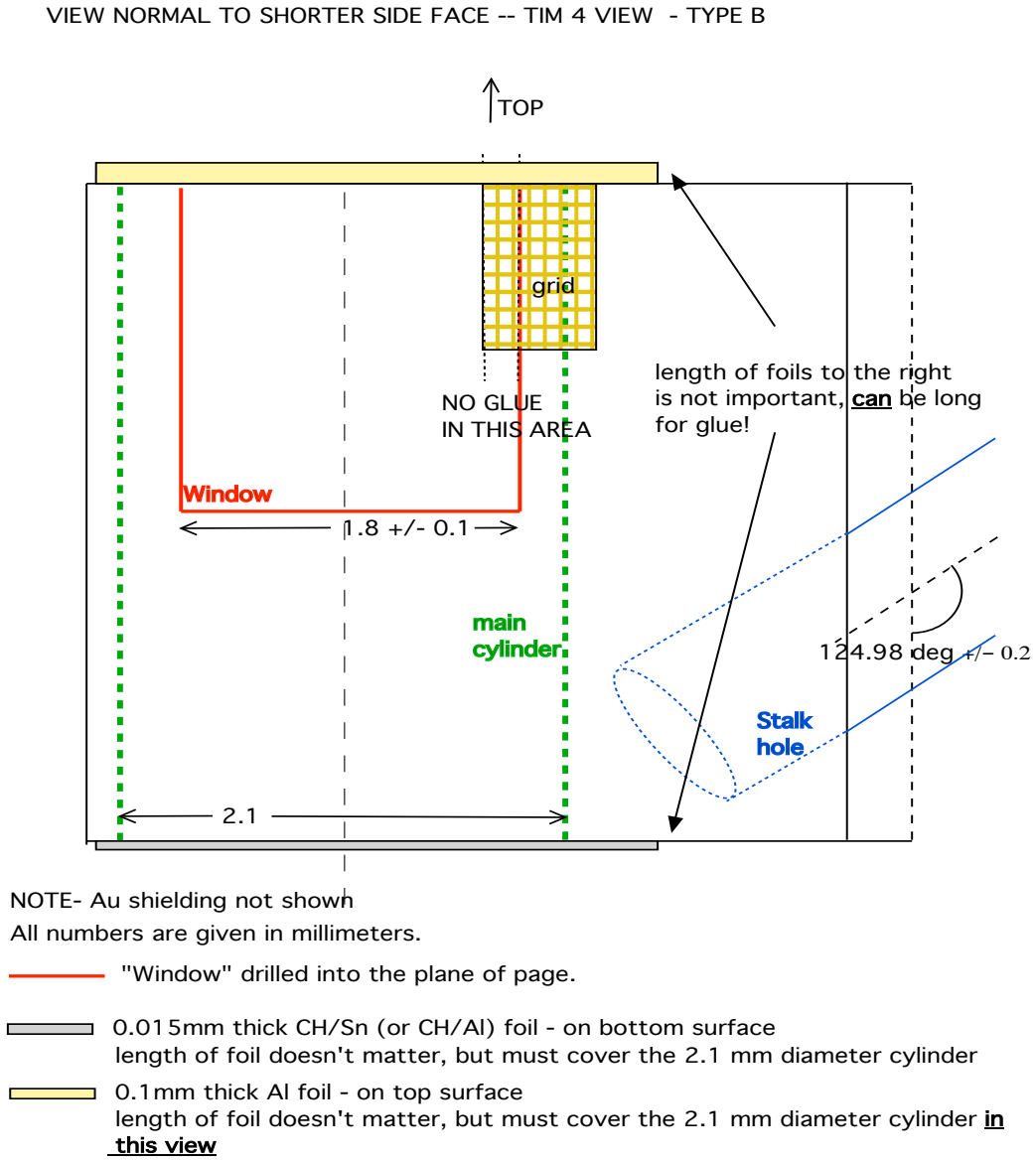

Figure A.5: Single view of radiography

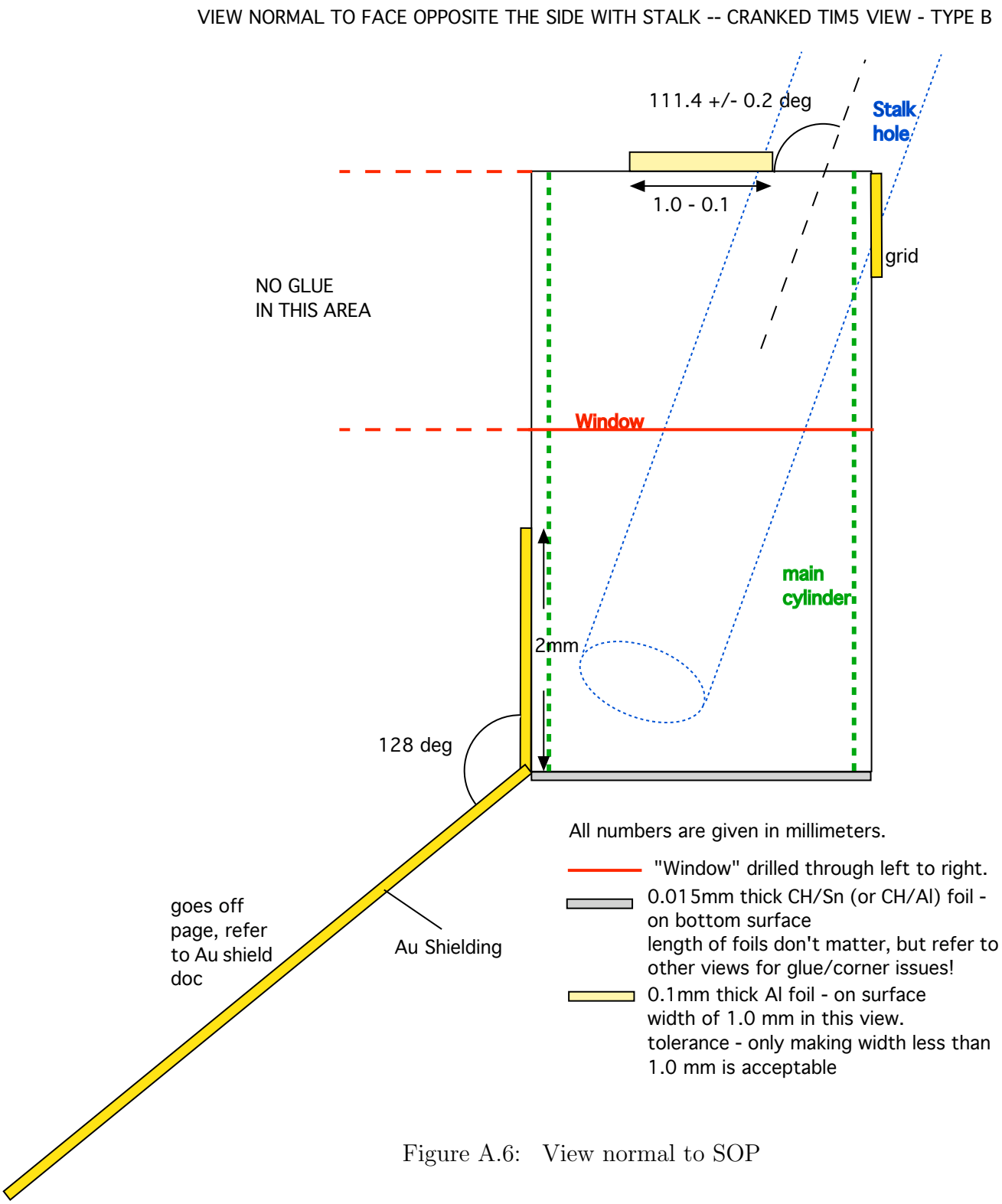

Figure A.6: View normal to SOP

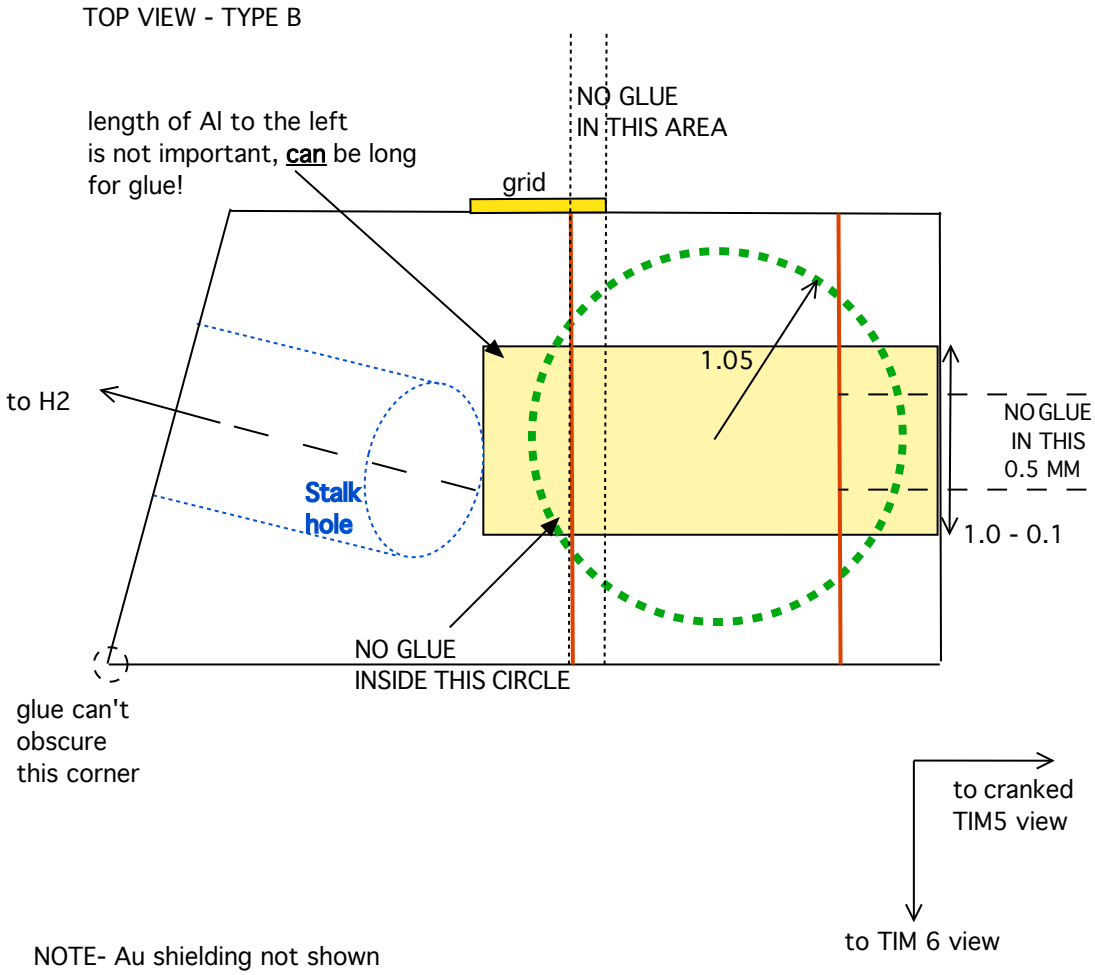

NOTE- Au shielding not shown

All numbers are given in millimeters.

"Window" drilled 2mm into the plane of page.

Inside these lines is the drilled 2.1mm diameter main cylinder.

0.1mm thick Al foil - on surface -- width of 1.0 mm by unknown length tolerance - only making width less than 1.0 mm is acceptable

Figure A.7: View normal to Al wall

A.3 June 15, 2011 - For Thomson scattering: RevRad1TS

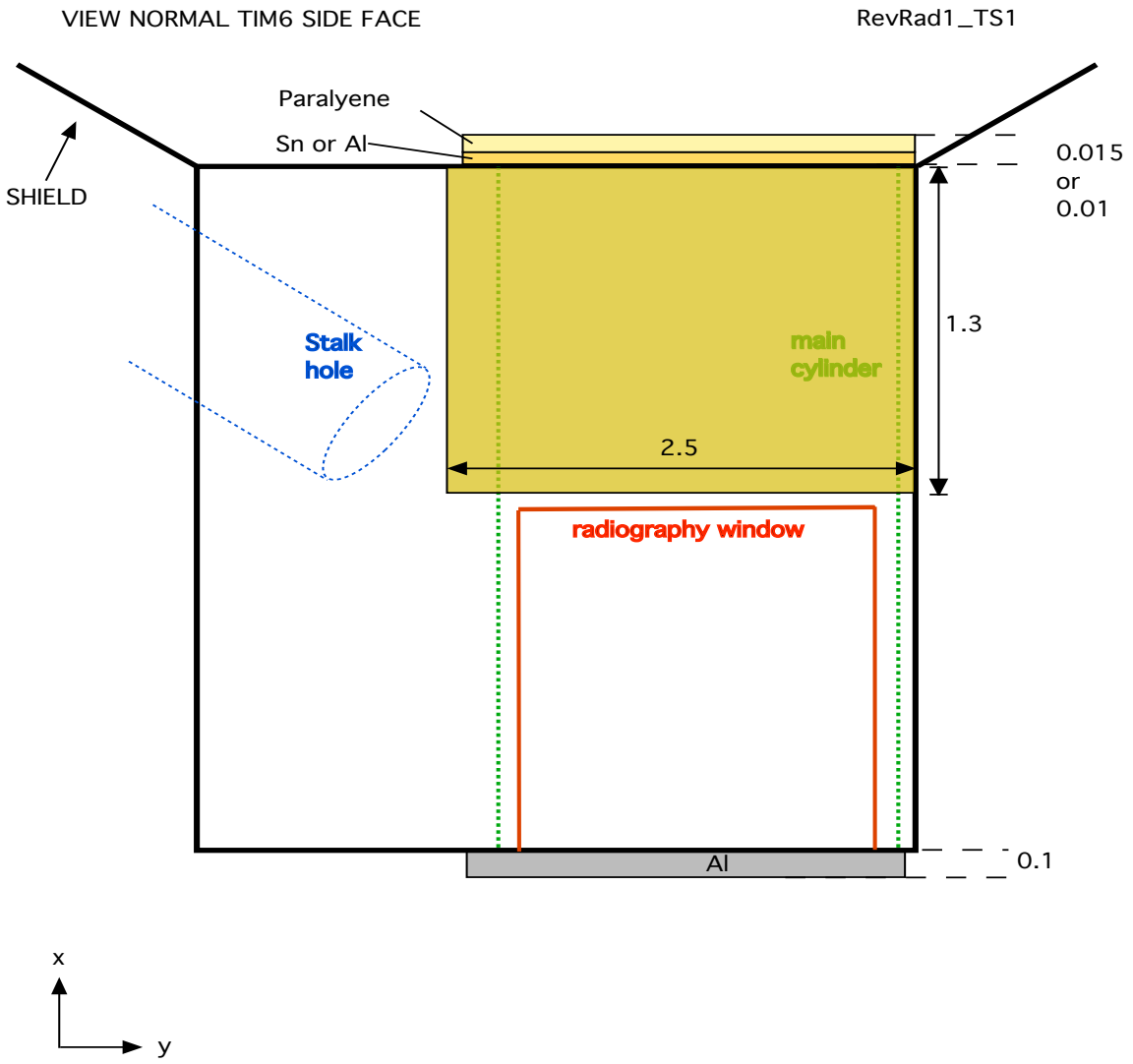

Al wall (single gray square) size in (-)y-direction doesn't matter, but must cover the 2 mm diameter cylinder.

All numbers are given in millimeters.

Figure A.8: View 1 normal to acrylic target body side

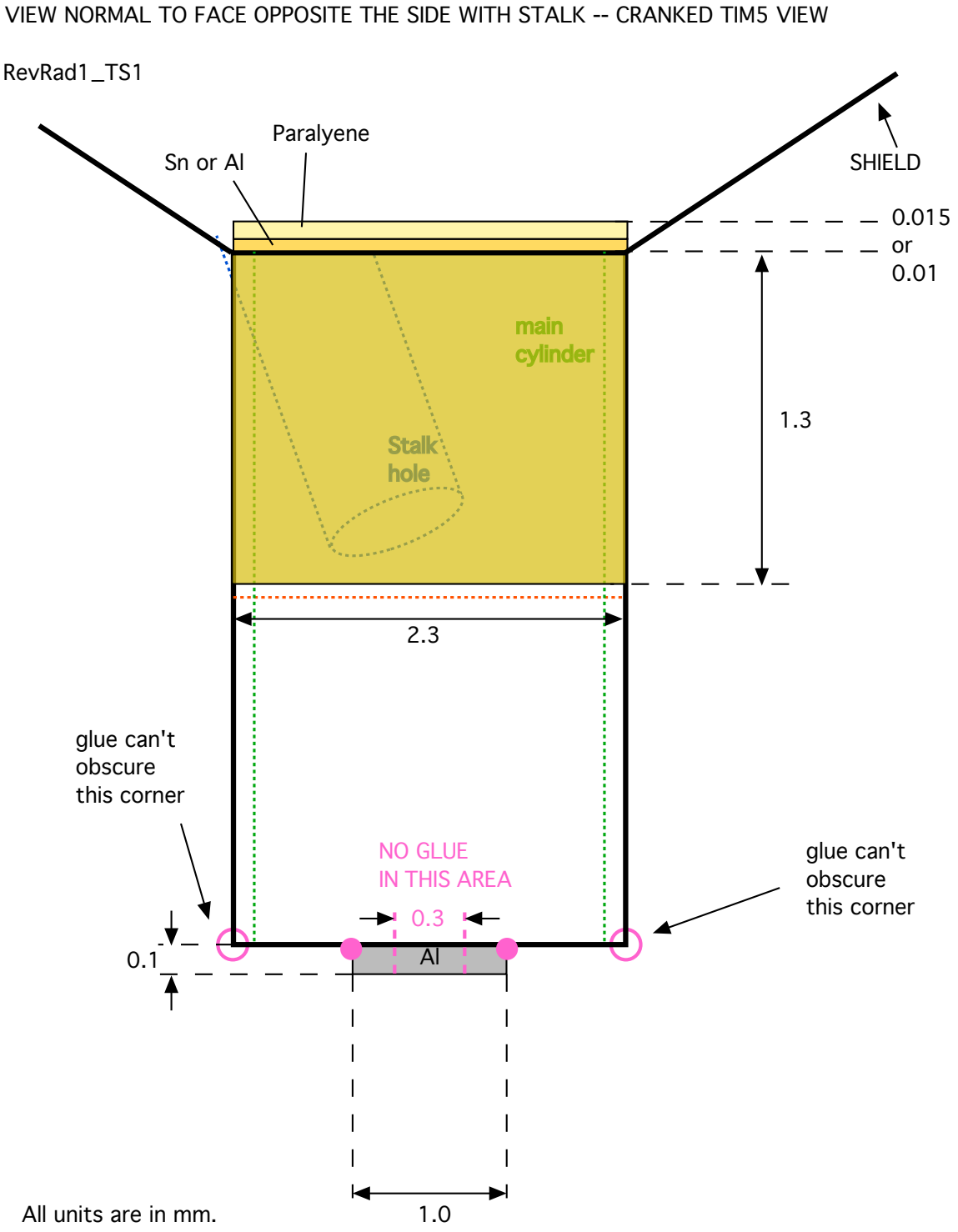

Figure A.9: View 2 normal to acrylic target body side

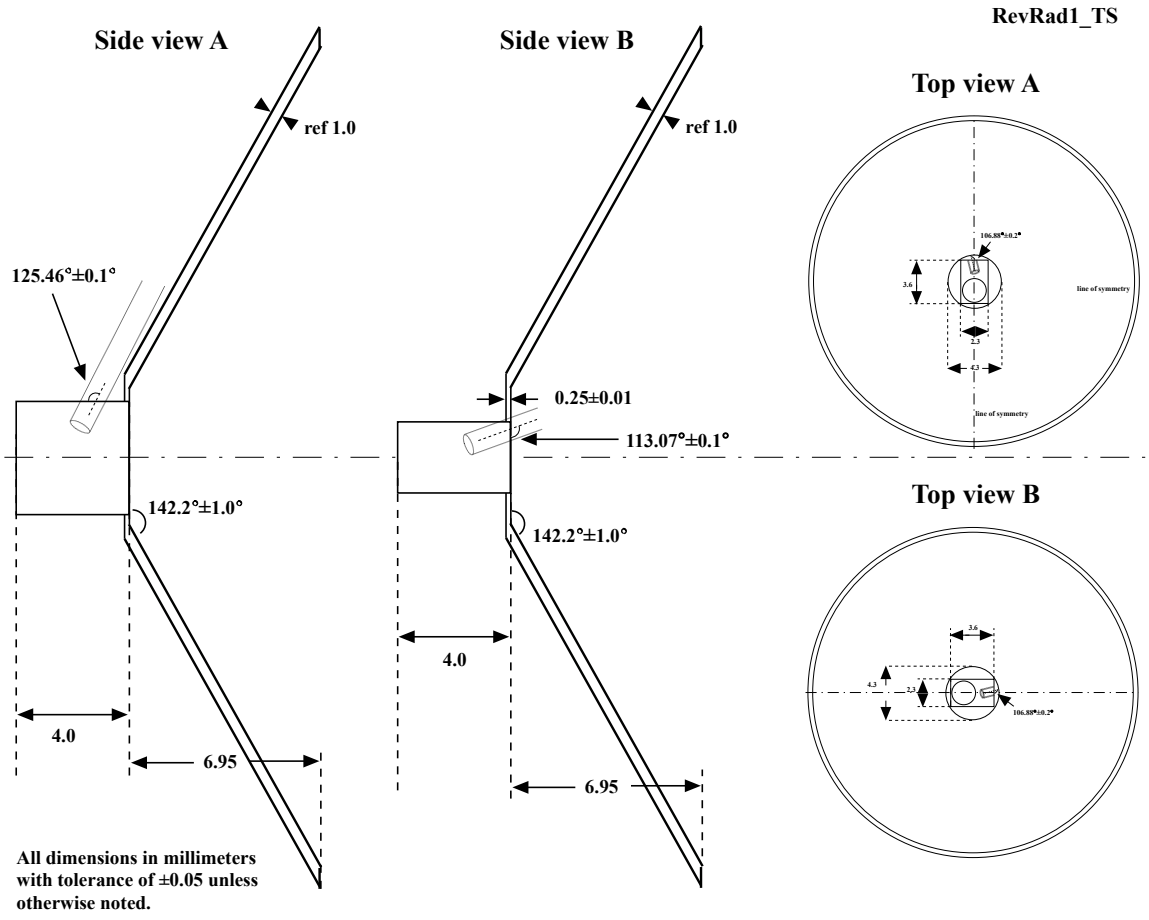

Figure A.10: Acrylic machining parts: target body and shield

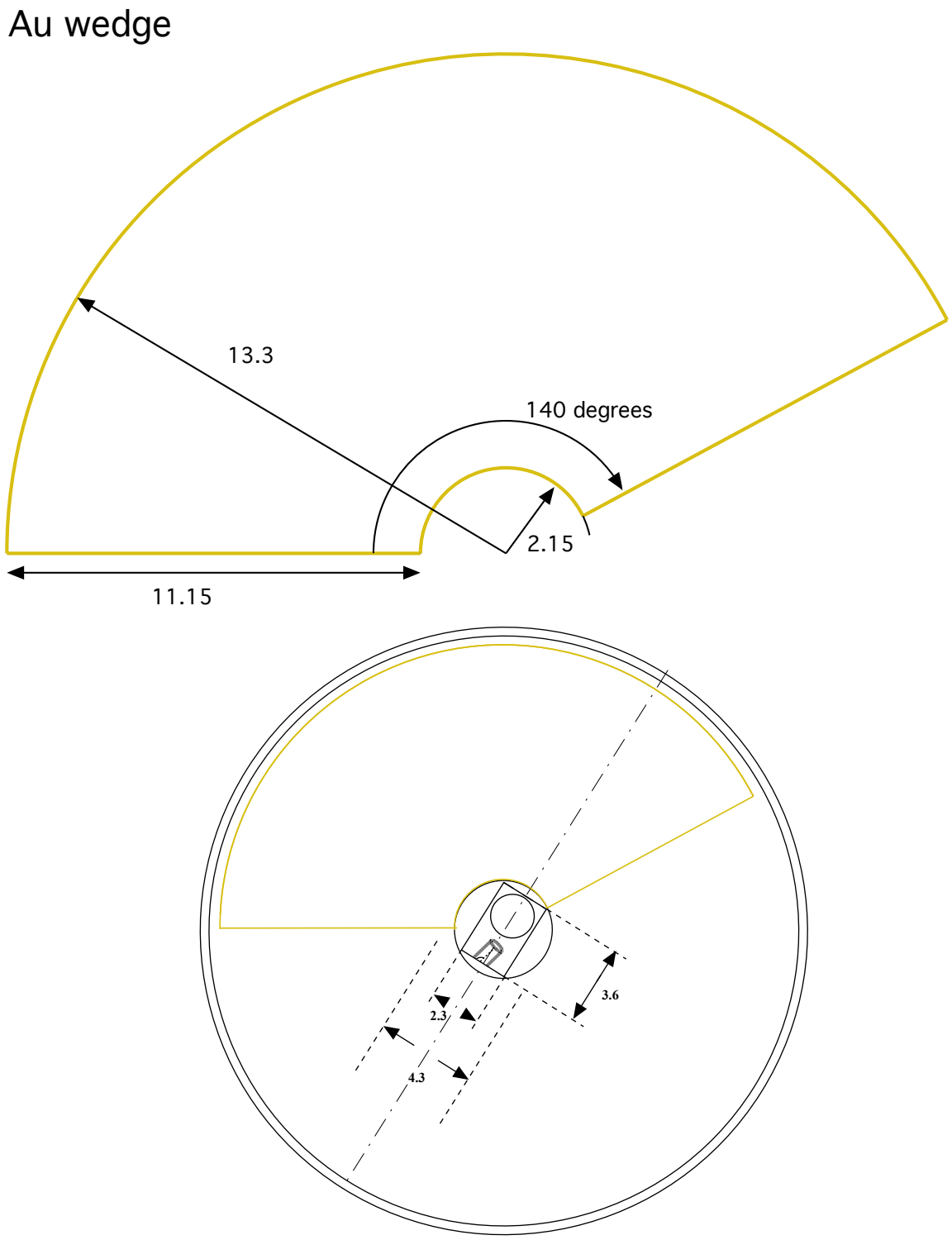

Figure A.11: Gold wedge placed around acrylic shield

A.4 June 15, 2011 - For Radiograph, normal incidence: RevRad2XRR1

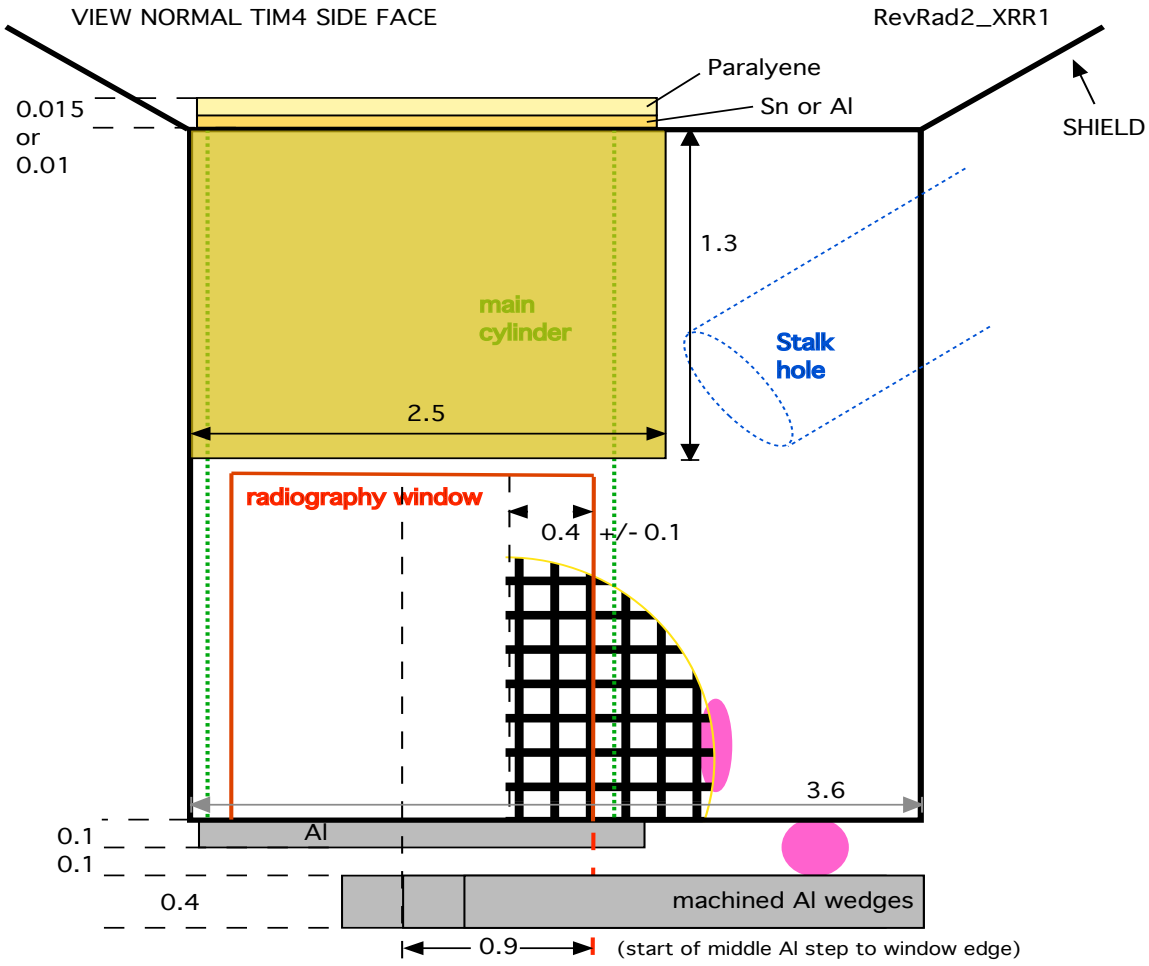

Figure A.12: Single view of radiography

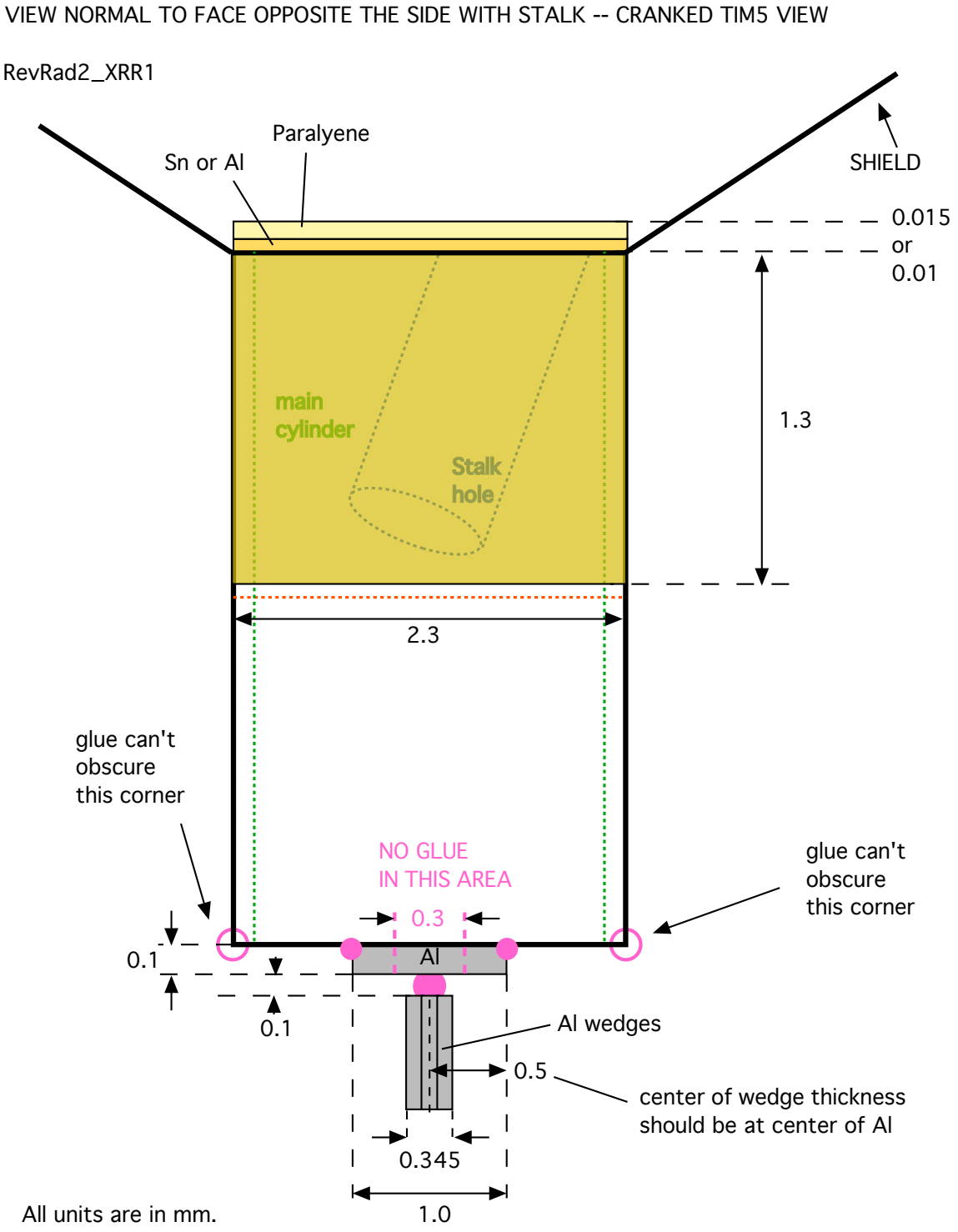

Figure A.13: View normal to SOP

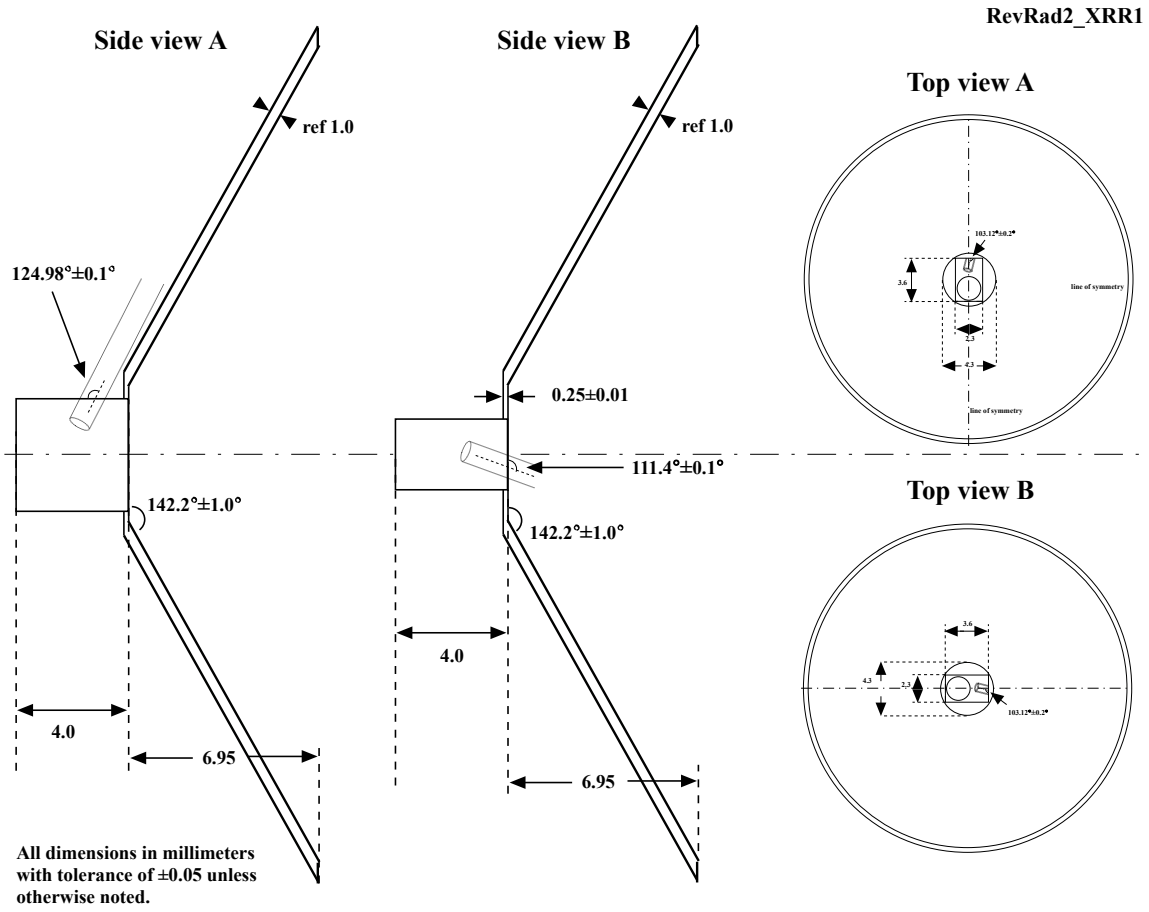

Figure A.14: Acrylic machining parts: target body and shield

A.5 June 15, 2011 - For Radiograph, oblique incidence: RevRad2XRR2

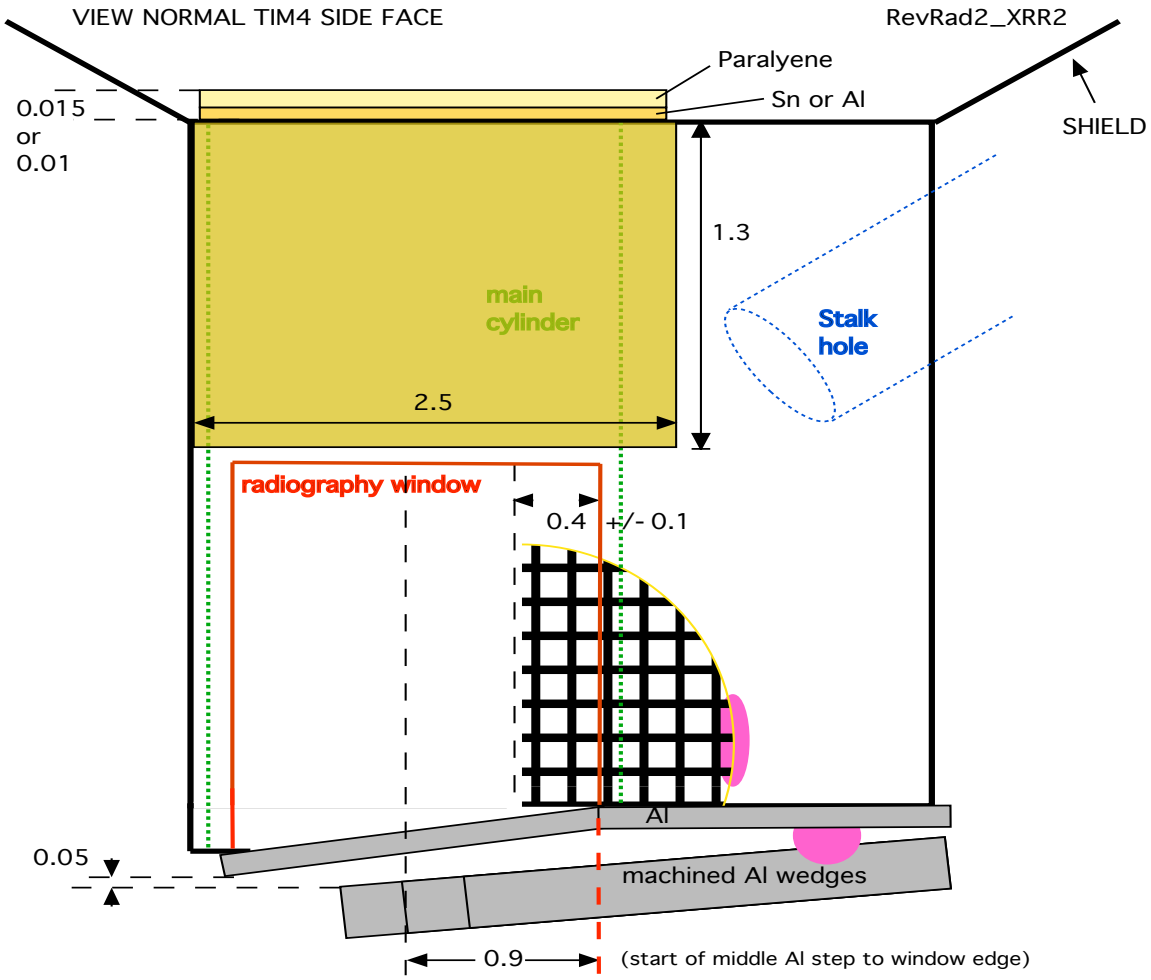

Figure A.15: Single view of radiography

BOTTOM VIEW - (COLLISION SIDE)

RevRad2_XRR2

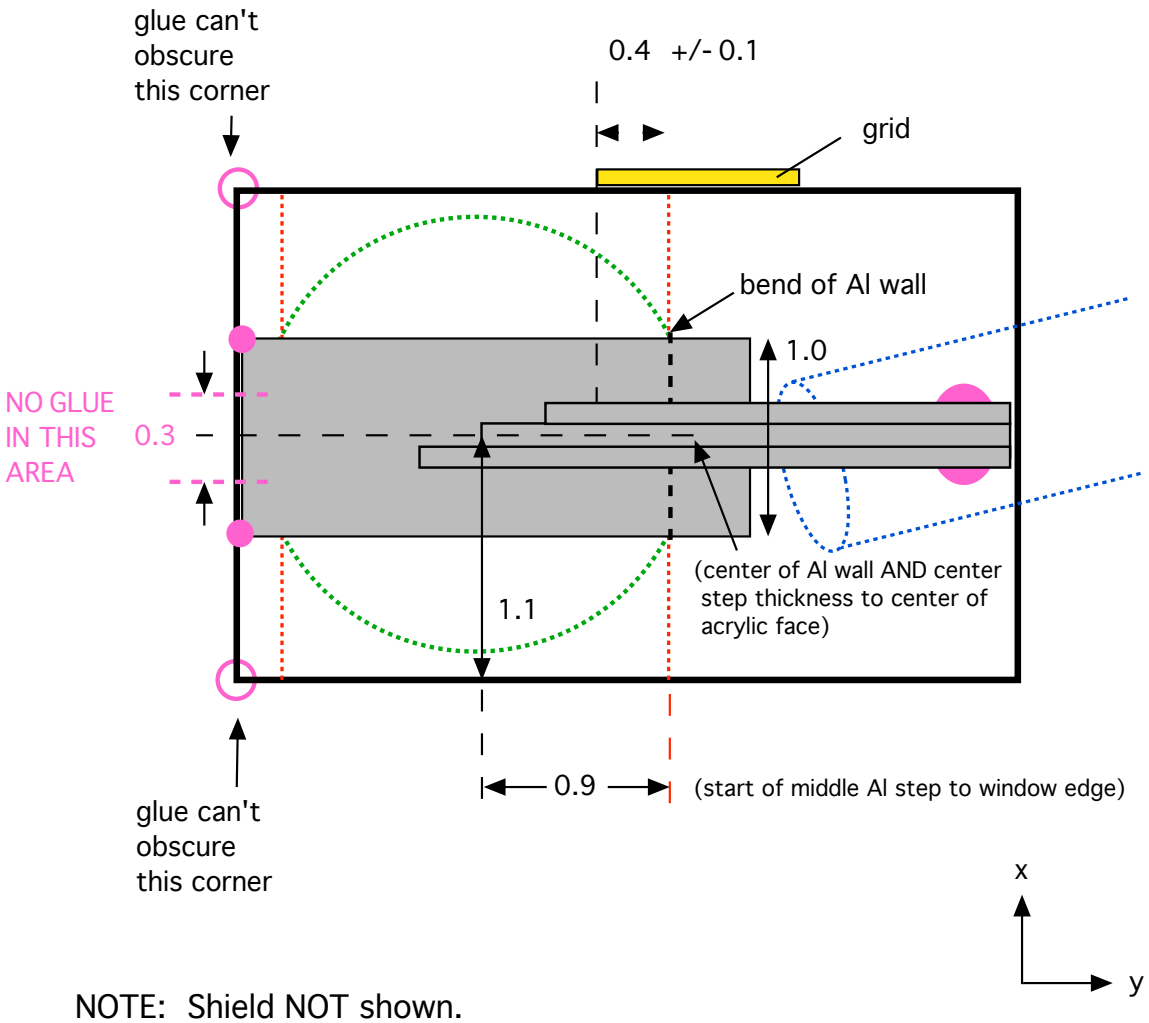

NOTE: Shield NOT shown.

NOTE: All Al (wall and steps) are at an angle into and out of this page

Al (gray square) size in y-direction doesn't matter, but must cover the 2 mm diameter cylinder.

All numbers are given in millimeters.

Figure A.16: View normal to Al wall

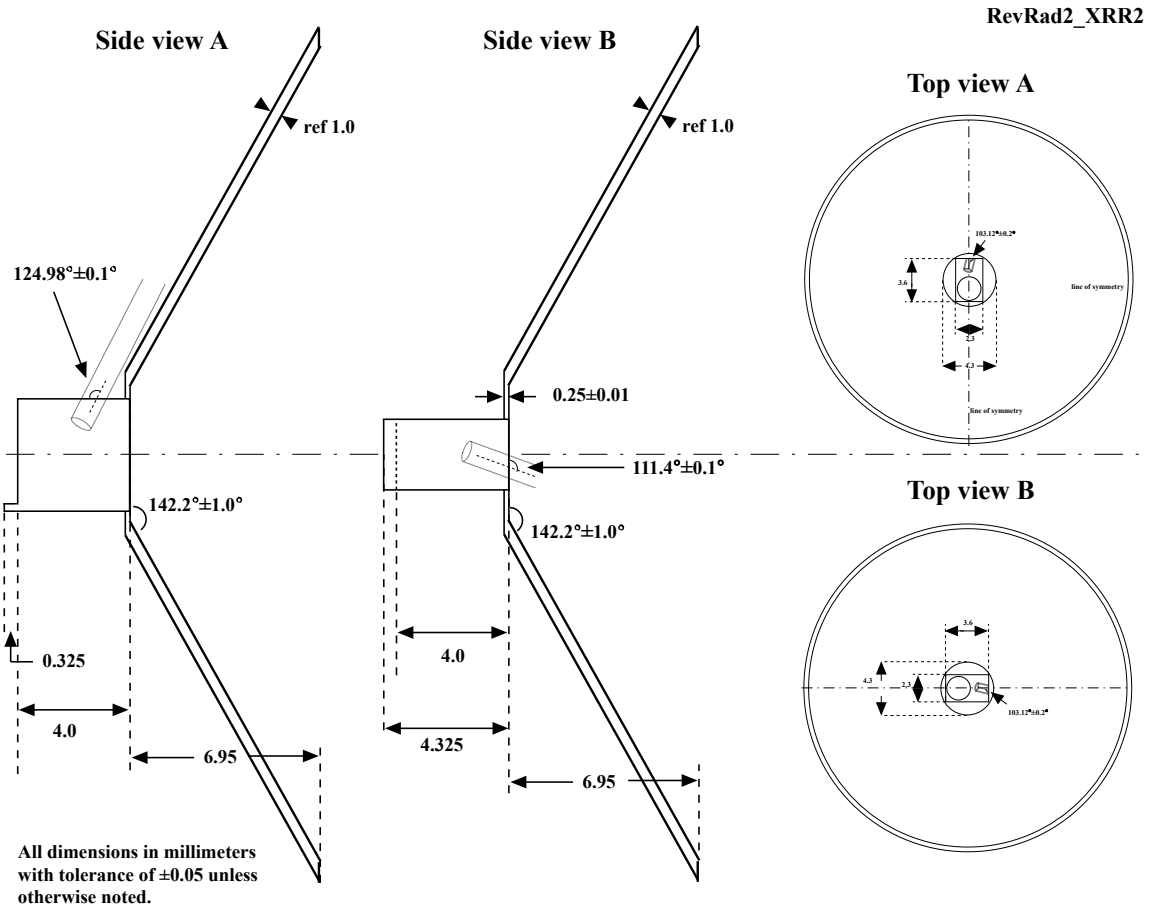

Figure A.17: Acrylic machining parts: target body and shield

A.6 September 8, 2011

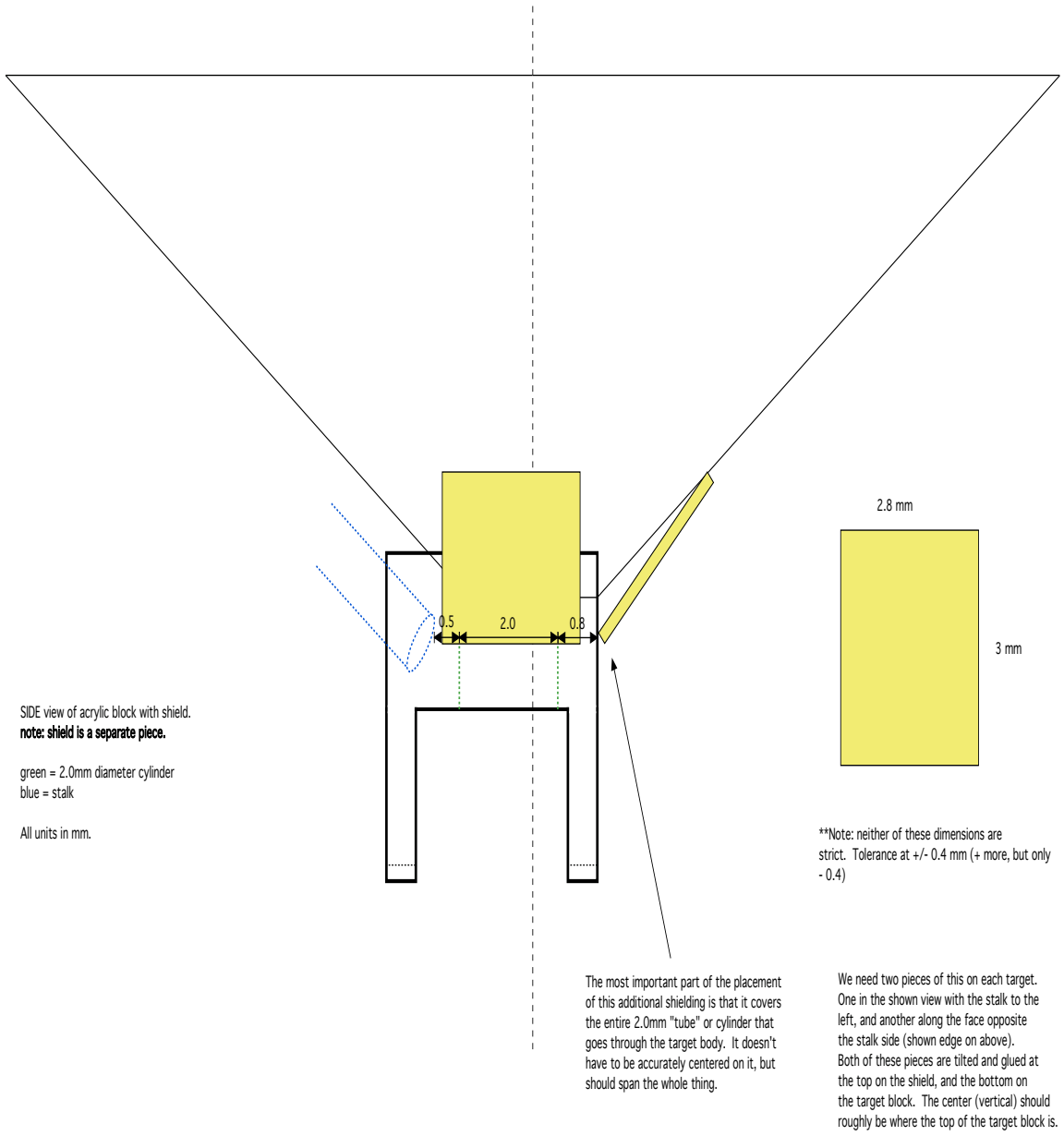

Figure A.18: Additional shielding added to target from June 15 campaign

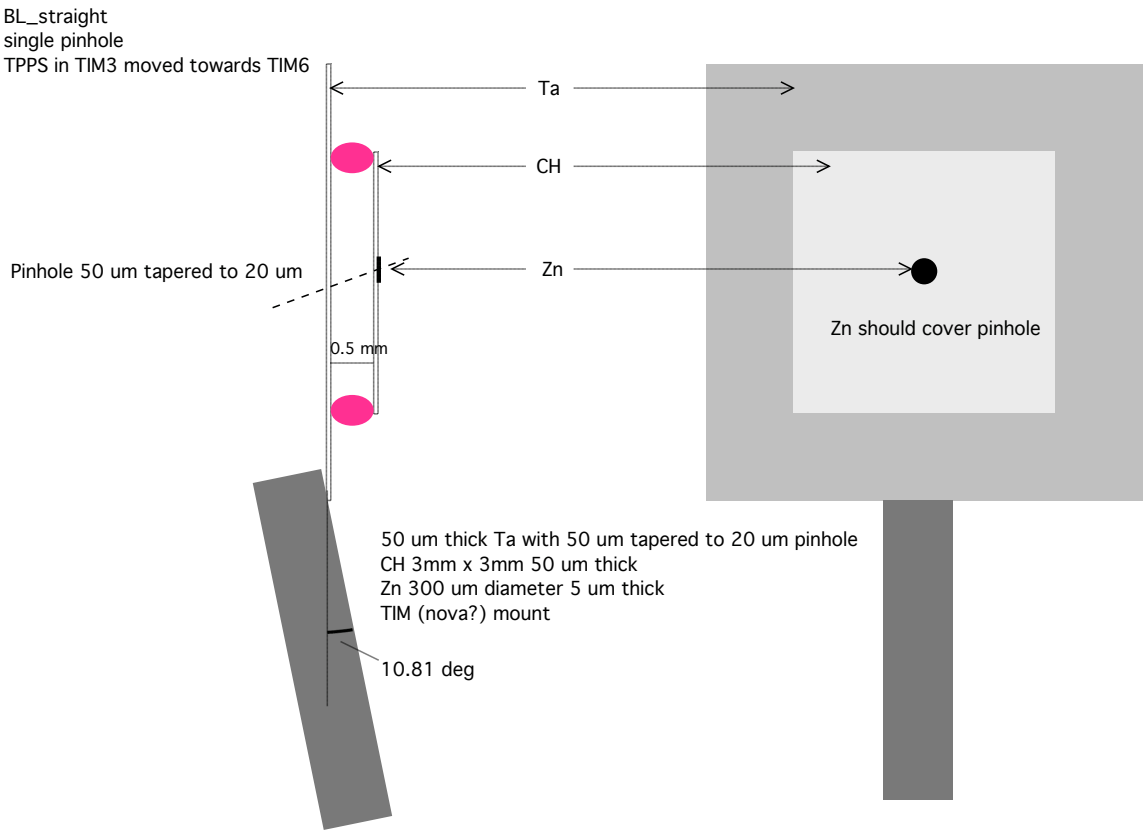

Figure A.19: Normal backlighter target design

BL_tilted
single pinhole
TPPS in TIM3 moved towards TIM6

50 um thick Ta with 50 um tapered to 20 um pinhole with 20 deg tilt!!
CH 3mm x 3mm 50 um thick
CH 7.7mm x 8.2mm
Zn 300 um diameter 5 um thick
TIM (nova?) mount

View normal to Ta and CH
(Ta inset in acrylic bore, CH on top of frame)

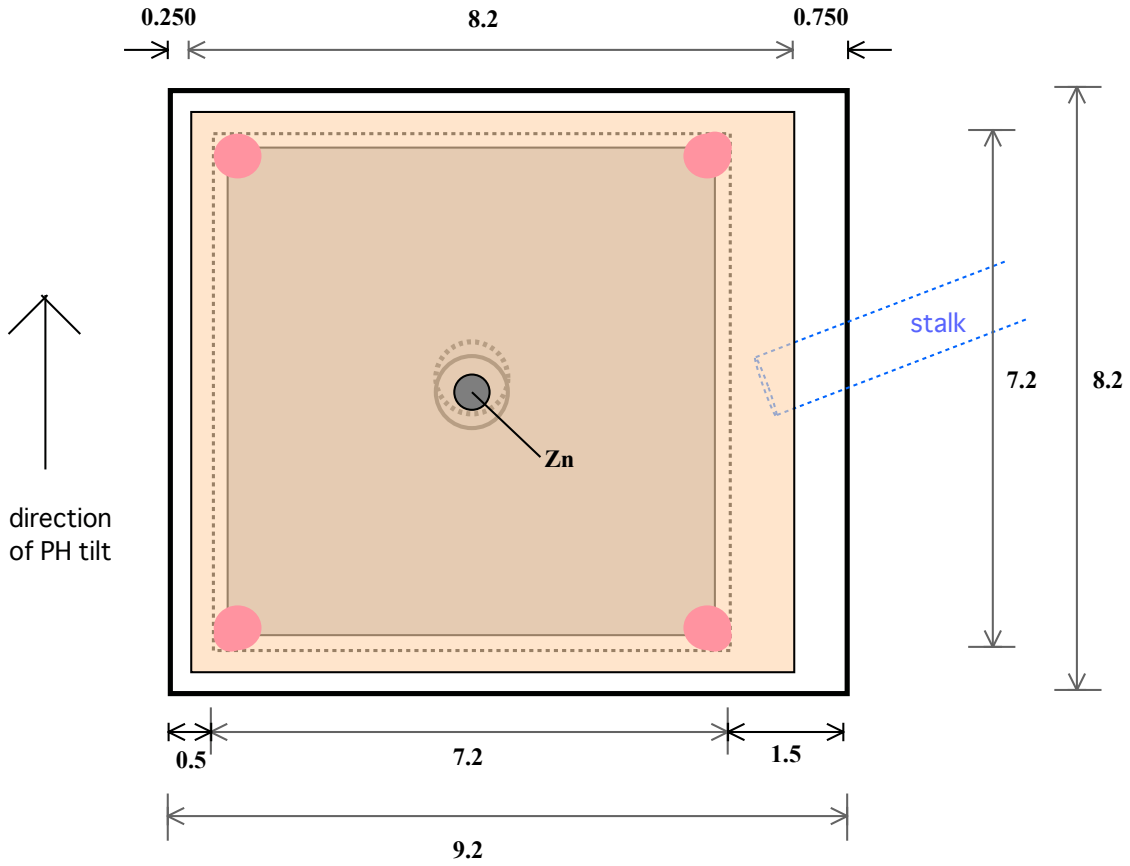

NOTES: 20um side of pinhole is face up in this view.
Ta placed in bore so that the pinhole is centered!
Zn centered over pinhole.

All dimensions in millimeters with tolerance of ±0.05 unless otherwise noted.

Figure A.20: Tilted and framed backlighter target design, view 1

BL_tilted
single pinhole
TPPS in TIM3 moved towards TIM6

50 um thick Ta with 50 um tapered to 20 um pinhole
with 20 deg tilt!!
CH 3mm x 3mm 50 um thick
CH 7.7mm x 8.2mm
Zn 300 um diameter 5 um thick
TIM (nova?) mount

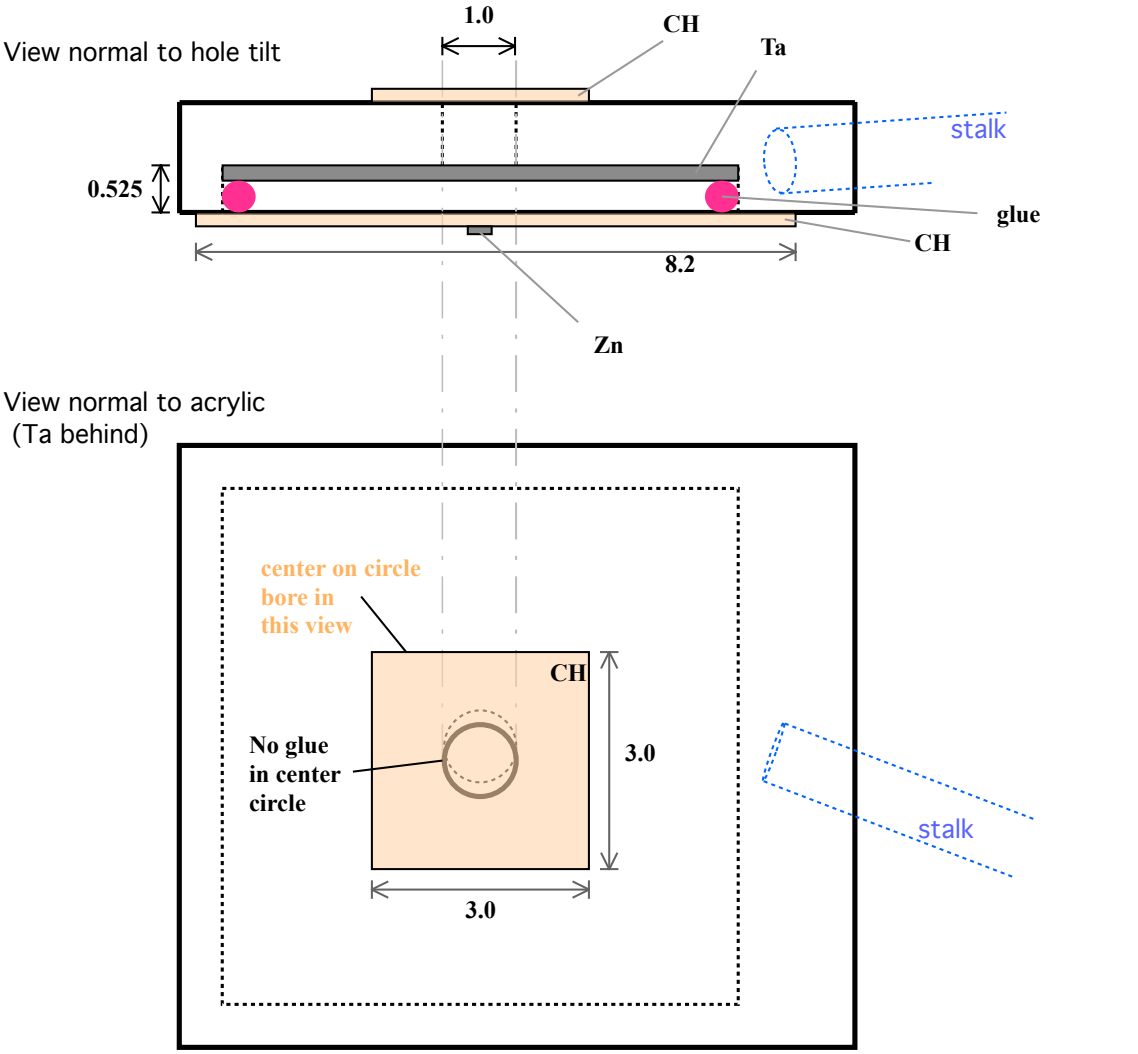

All dimensions in millimeters with tolerance of ±0.05 unless otherwise noted.

Figure A.21: Tilted and framed backlighter target design, view 2

A.7 July 19, 2012 - 15° tilt

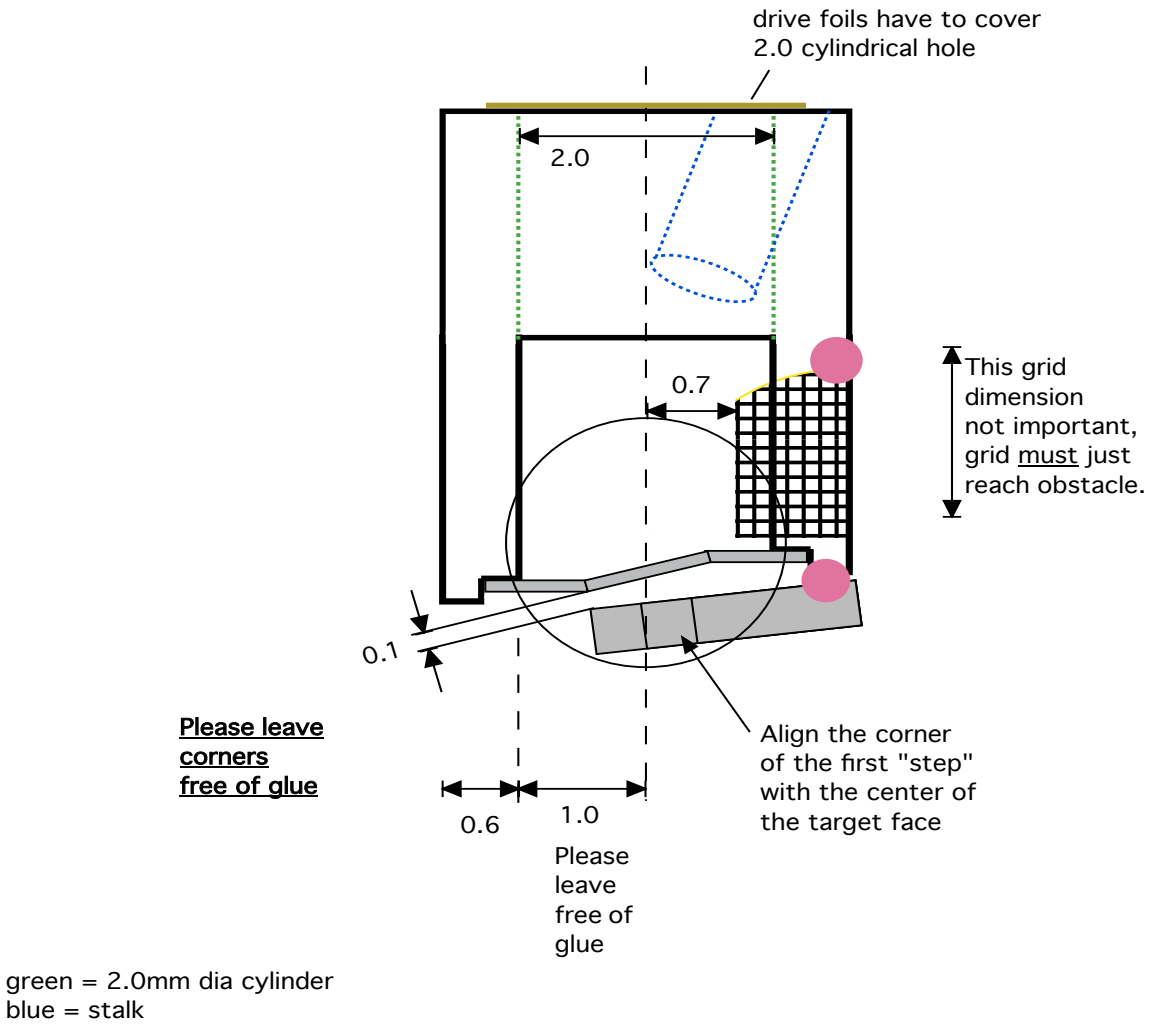

Figure A.22: Single radiography view for 15° Al tilt

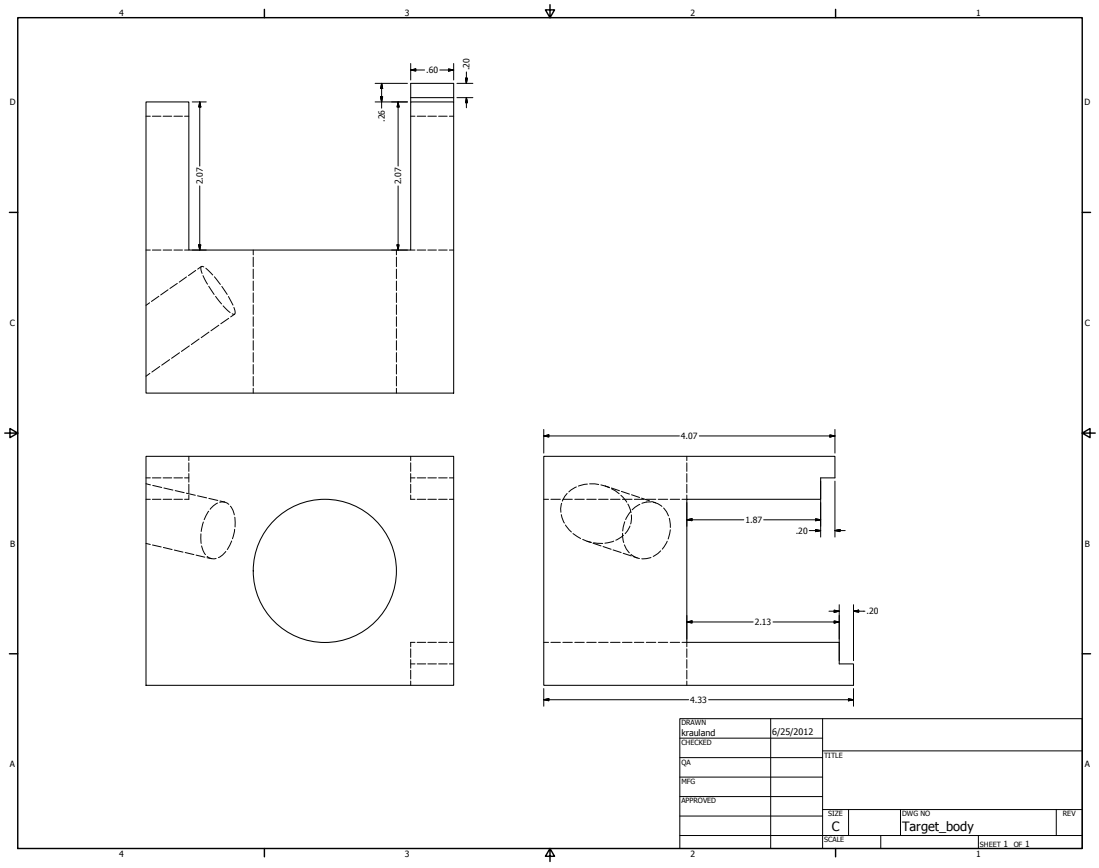

Figure A.23: Acrylic target body for 15° Al tilt

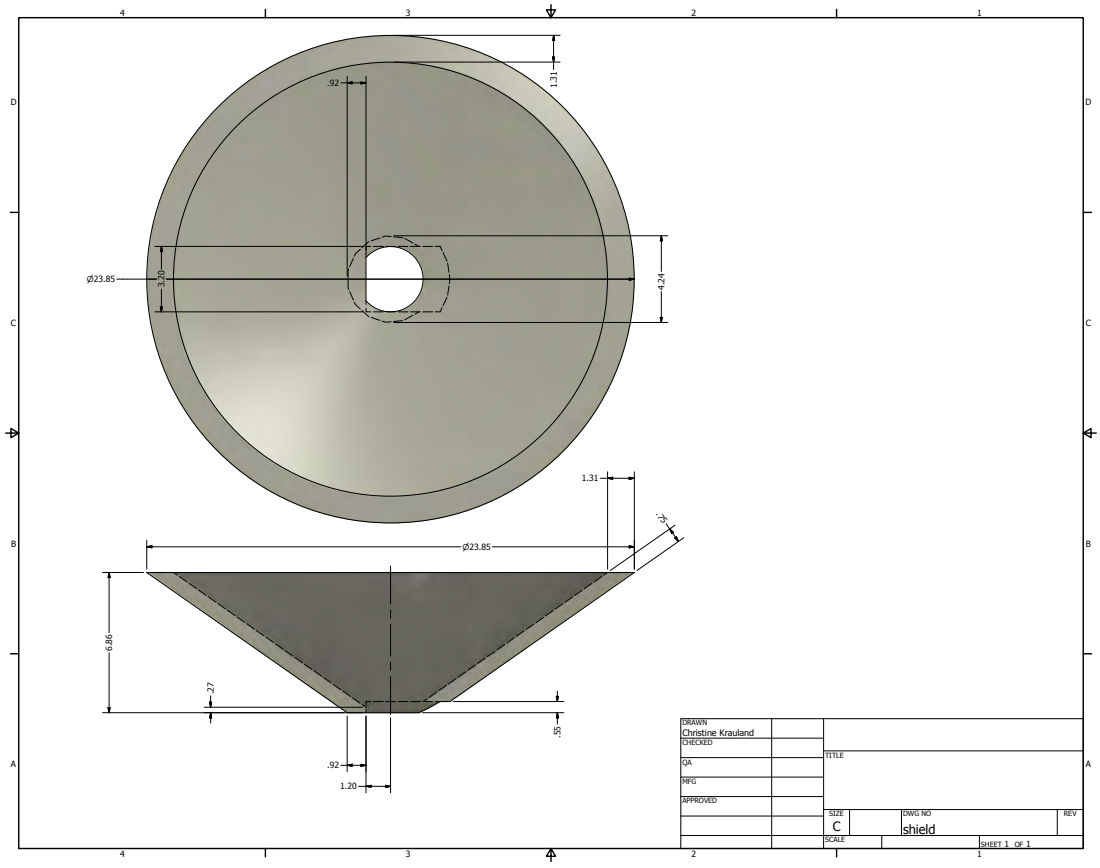

Figure A.24: Shield design for all target in this campaign

A.8 July 19, 2012 - 30° tilt

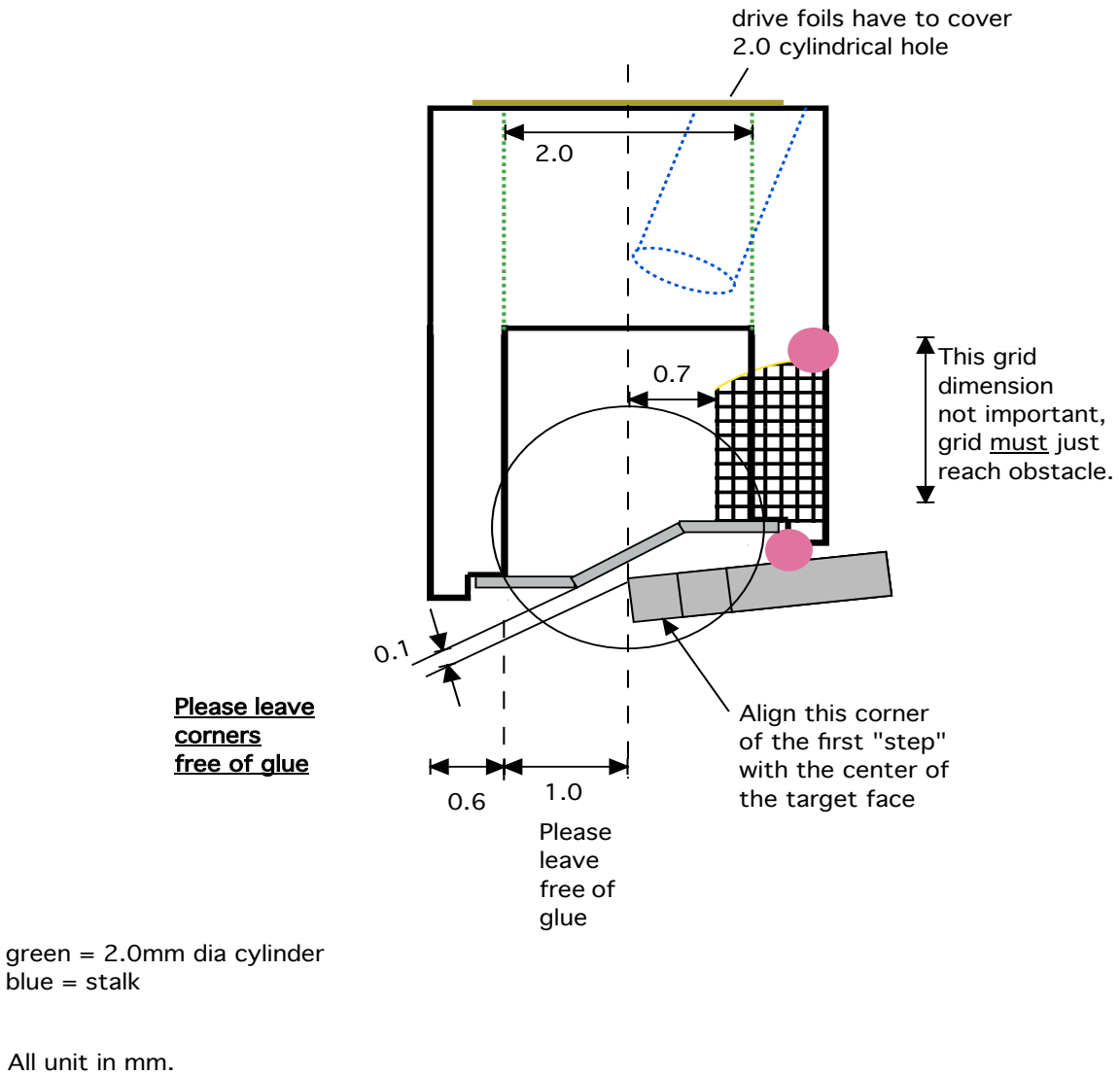

Figure A.25: Single radiography view for 30° Al tilt

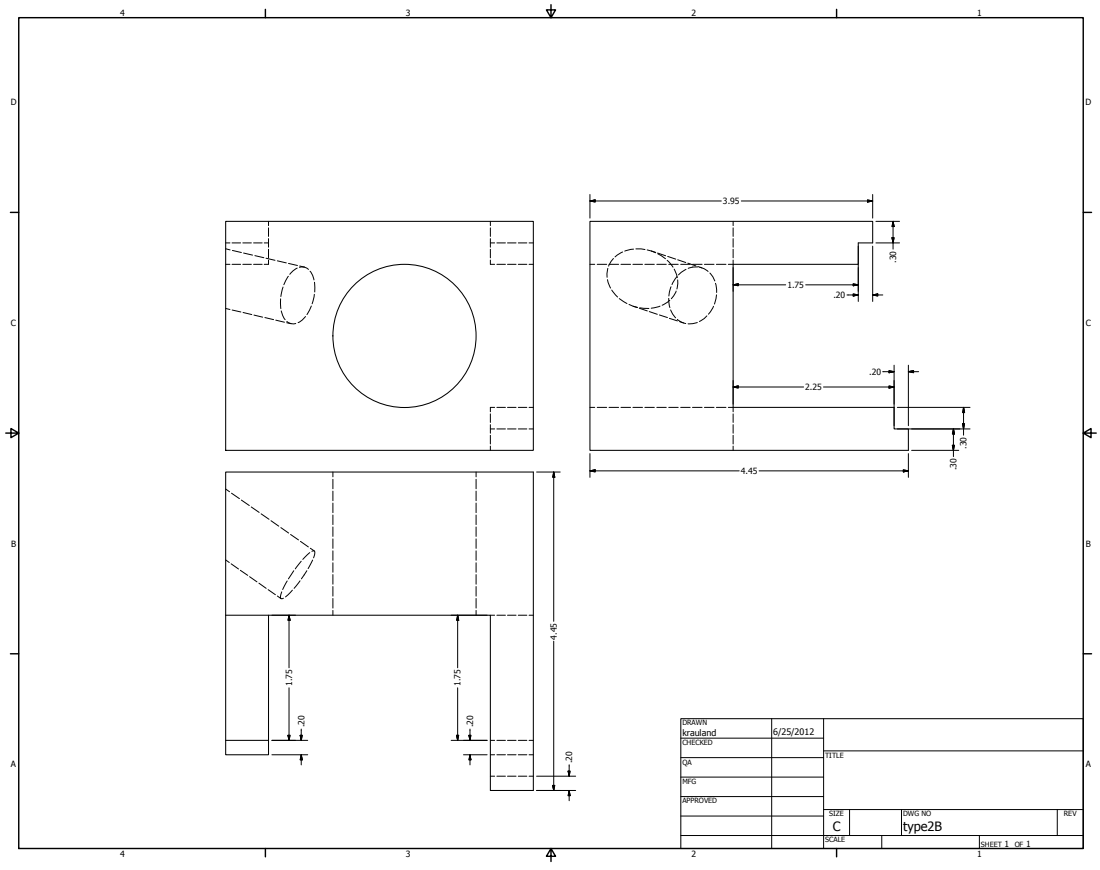

Figure A.26: Acrylic target body for 30° Al tilt

APPENDIX B

Catalog of radiographs and film background

The information contained in this appendix overviews some of the experimental issues that are observed in the x-ray radiography data collected during the course of this thesis work. It is organized and presented by experimental campaign date. A catalog is presented at the beginning of each section for all shots relating to the reverse shock research taken on the given day. This is followed by images and some discussion applicable to experimental errors. After film is developed, it is scanned with a Perkin-Elmer PDS microdensitometer. The microdensitometer measures the relative transmission of light through a spatially localized piece of exposed film. As implied in Chapter III, the films total optical density OD = log (I / I_0) is obtained. Sometimes referred to as raw film density, the OD data contains contributions from the film substrate, inherent film fog, background from scattered light, and finally the actual desired signal. This is depicted in Figure B.1. The portion of the raw film density resulting from the film substrate, or base, and fog is specific to each type of film. Moreover, these can vary with the films age or changes in the development process [52]. Also discussed in Chapter III, some fraction of the background undoubtedly results from high-energy bremsstrahlung emission. This will contribute to error in extracting mass densities from the radiograph assuming the high energy emission

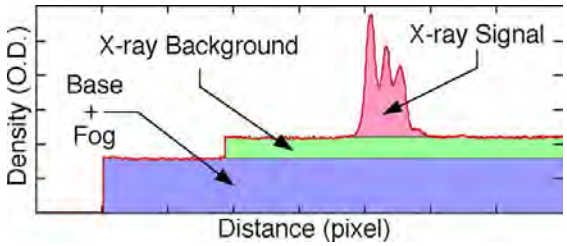

Figure B.1: The measured total optical density includes contributions from the film base, film fog, scattered background, and desired signal [52].

images the target as discussed in Chapter IV. As shown in Figure B.1, it is treated as non-imaging background exposure. It should be noted that all images below are raw data in the sense that have not been adjusted for background subtraction. Likewise the images have not been rotated, so the axis of flow of all radiographs shown in this appendix is roughly 18° off of the vertical direction in the counter clockwise direction. The flow will be moving towards the Al wall from the bottom of the image.

B.1 Experimental Campaign : August 5, 2010

Table B.1: Radiography overview : August 5, 2010

SHOT# (RID)	Radiography?	Pieces of Film	Comments
59001 (31864)	Yes	1	not usable
59002 (32688)	Yes	2	weak signal, shadow
59004 (32689)	Yes	3	bucket target, weak shadow
59006 (32803)	Yes	3	weak signal, shadow
59008 (32804)	Yes	1	not usable

Figure B.2: Shot 59002

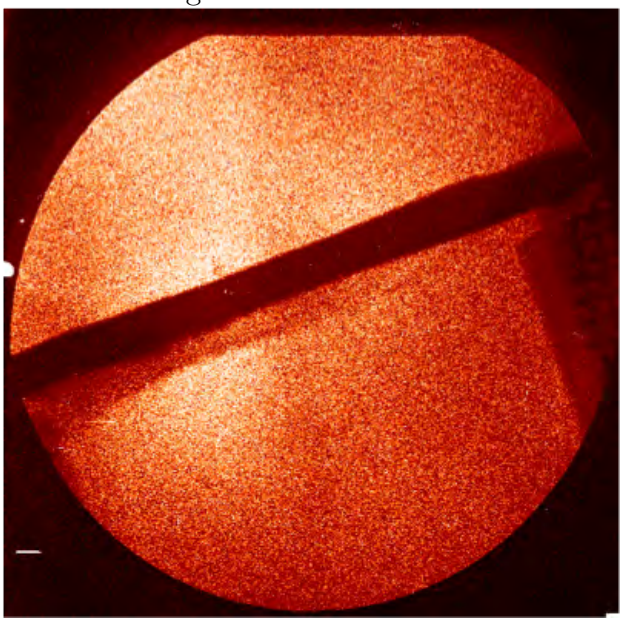

Figure B.3: Shot 59004

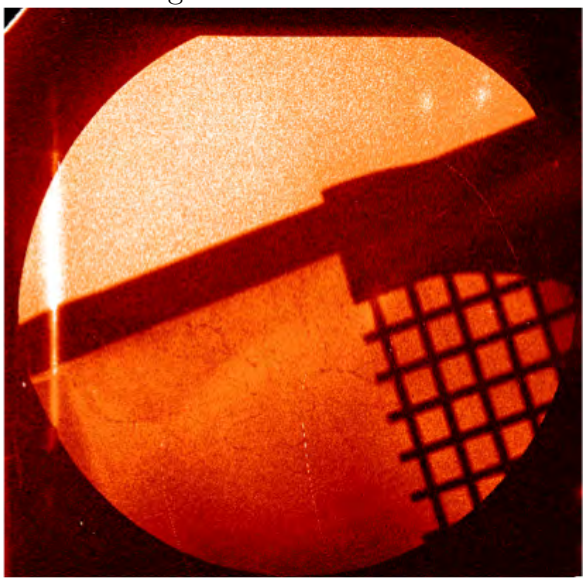

Figure B.4: Shot 59006

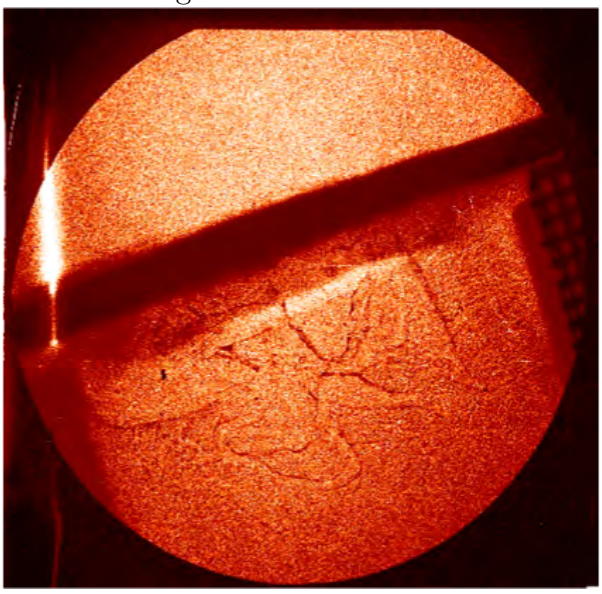

These data were the first collected in the initial experimental attempt at shooting reverse shock targets. For this campaign only, the target axis (or flow axis, often referred to in the text) was 4.8 mm long as opposed to 4.0 mm in the later campaigns. The longer distance was initially thought to be desirable for maximizing the velocity of the accelerating flow.

Two undesirable outcomes were discovered in these radiographs. The first was the x-ray signal on shot 59002 and shot 59006. Both radiographs were captured using a slightly different approach to creating an x-ray source. Much research has been done to make x-ray sources brighter, or in other words, make the laser conversion efficiency (CE) higher when irradiating metal foils. It has been shown that solid metallic targets exhibit much lower CE than underdense plasma sources [34, 35, 78, 92]. In order to produce metallic plasmas at lower density and higher temperature for better CE, a thin foil can be made into underdense plasma with a prepulse and then be subsequently heated by a main laser pulse [4]. This approach was attempted on both shot 59002 and shot 59006 where 2 beams are triggered 4 ns before 5 other backlighter beams. Unfortunately, the result of lower signal was realized in these radiographs and the method was not explored further. The decreased resolution is visually noticeable by the graininess of the image.

The second issue involves background exposure. All images captured during this campaign showed a shadow cast onto the film. It is not easily seen in these images and will be clearly shown and discussed in the next section.

B.2 Experimental Campaign : June 15, 2011

Table B.2: Radiography overview : June 15, 2011

SHOT# (RID)	Radiography?	Pieces of Film	Comments
62630 (35577)	No	0	Thomson scattering attempted
62631 (35578)	No	0	Thomson scattering attempted
62632 (36096)	No	0	μDMX only
62633 (36098)	No	0	Thomson scattering attempted
62634 (35581)	Yes	1	only piece in pack
62635 (35582)	No	0	BLANK, Filter pack error
62636 (35588)	Yes	3	4/6 foil, dark circle
62637 (35584)	No	0	BLANK, Filter pack error
62638 (35585)	Yes	1/3	Co/Al, low photon count, BC
62639 (36102)	No	0	BLANK, Filter pack error

Figure B.5: Shot 62634

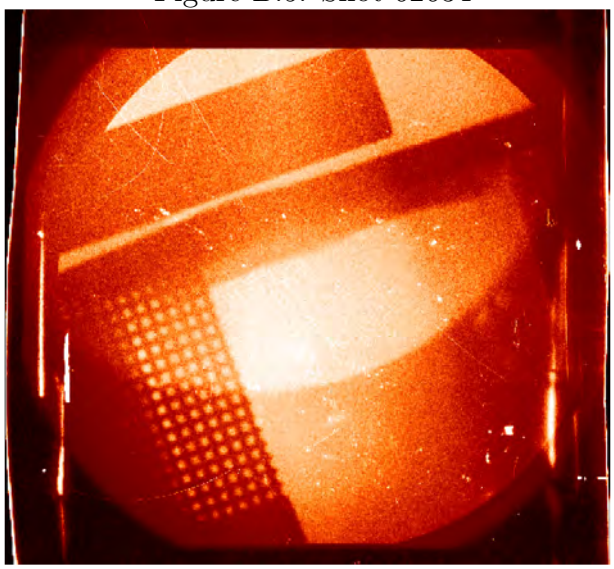

Figure B.6: Shot 62636

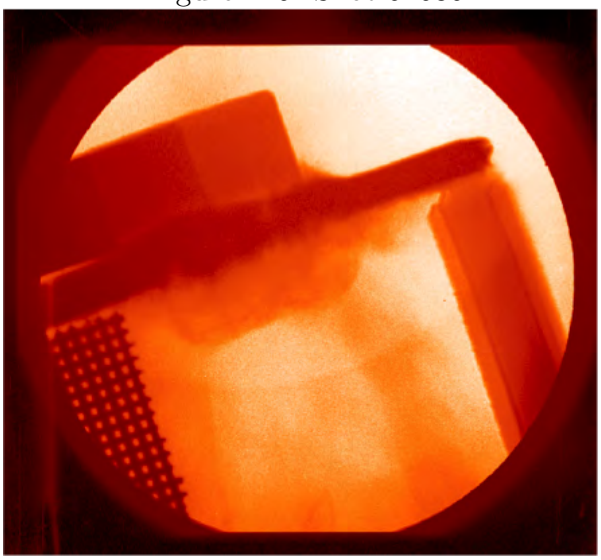

Figure B.7: Shot 62636 with shadow outlined

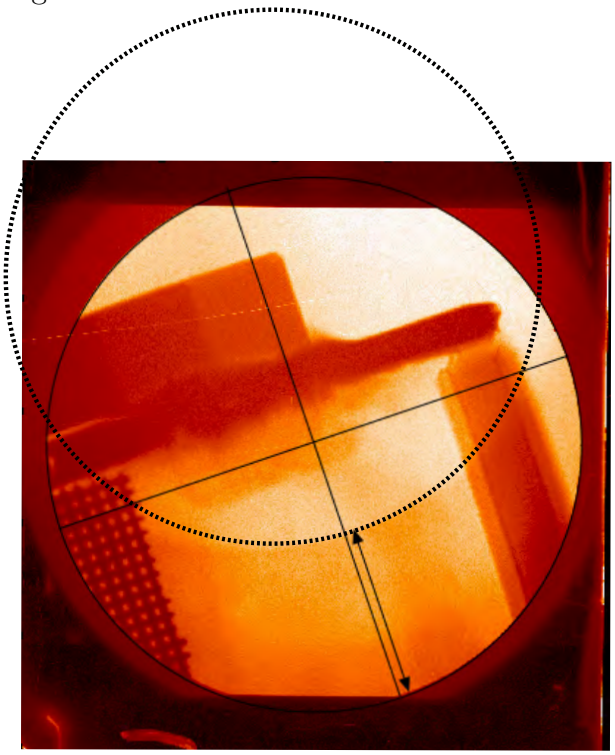

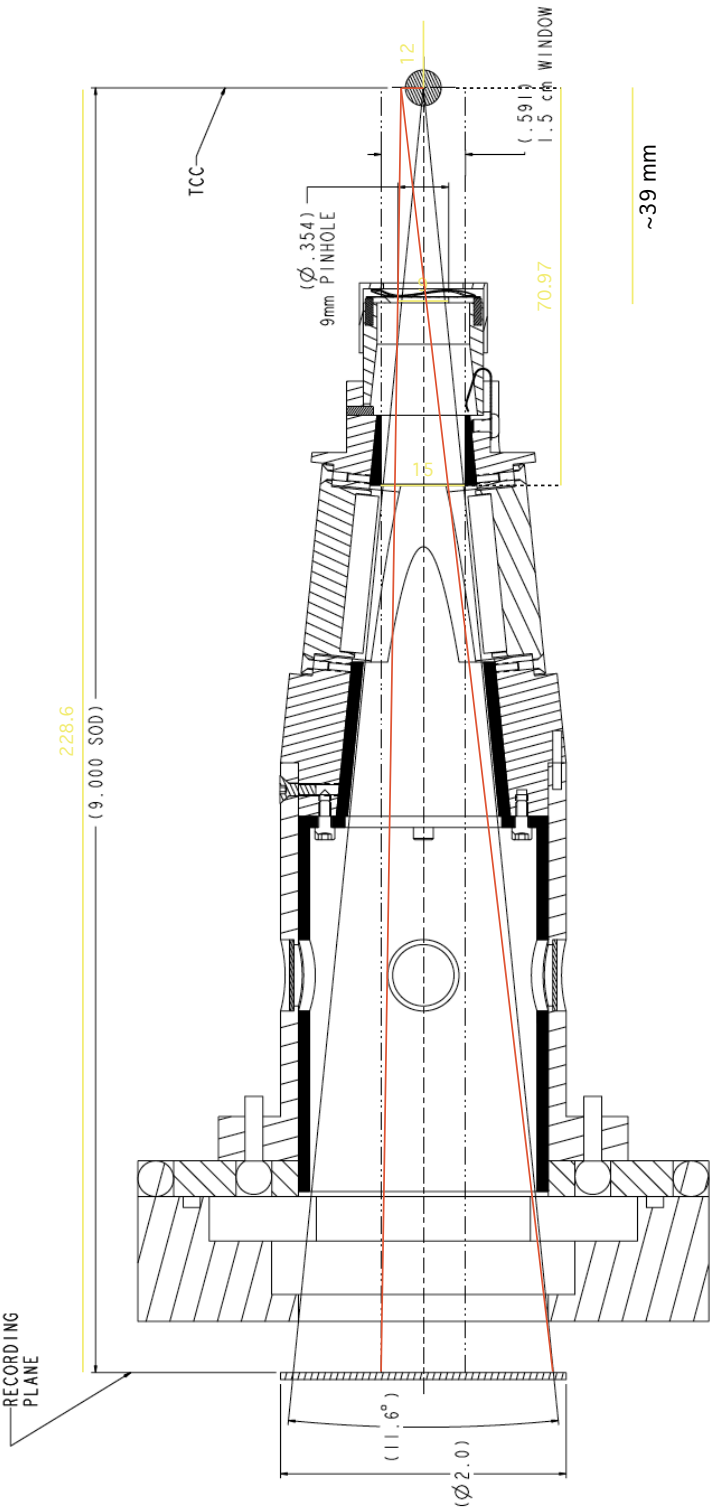

Figure B.8: Magnetic Point Backlighter (MPBL) assembly with ray tracing

Both Figure B.5 and Figure B.6 show the background shadow. Figure B.7 shows an outline of the field limiting aperture and and an outline of its displaced image cast by a secondary source of light. The shadow, by the traditional meaning, would be represented by the space between the arrows. For ease, we will call the displaced image (dotted circle) the anti-shadow. The structure of the diagnostic snout, called a Magnetic Point Backlighter (MPBL) snout, determines the image field of view with a 9 mm diameter pinhole, showing a mostly circular area of data. The solid line circle represents the magnified 9 mm pinhole but the data is clipped by the size of the back of the assembly where film is placed. The MPBL assembly can be seen in Figure B.8. It is evident from the shape and placement of the anti-shadow that the unshielded source is along the axis of flow. Measuring the displacement of the circular shadow revealed that the source is coming from very near to the drive foil initial location, i.e. the laser spot. Figure B.8 also shows a basic ray tracing of this secondary source, represented by the red lines. The importance of proper gold (Au) shielding around the drive foil was realized. The initial shield thickness, 50 μm of Au, transmits less than 10% of photon energies up to 30 keV and less than 1% for photon energies below 20 keV. If emission is transmitted through the shielding than it would be very high energy. It is also possible that the shielding was not properly covering the initial section of the target body, such that emission at the ablation surface had some line of sight to the film through the acrylic body. Based on these findings, thicker Au shielding was added to the later campaigns as well as extended further down the target.

B.3 Experimental Campaign : September 8, 2011

Table B.3: Radiography overview : September 8, 2011

SHOT# (RID)	Radiography?	Pieces of Film	Comments
63485 (36564)	Yes	1/3	Film damaged
63489 (36565)	Yes	3	4/6 foil, preheated
63491 (36566)	Yes	1/3	Low signal (tilted ph)
63492 (36567)	Yes	3	4/6 foil
63493 (37070)	Yes	1/3	Low signal (tilted ph), bright feature
63494 (37071)	No	0	maybe see a grid in 1, tilted ph
63495 (37072)	Yes	3	4/6 foil

Figure B.9: Shot 63485

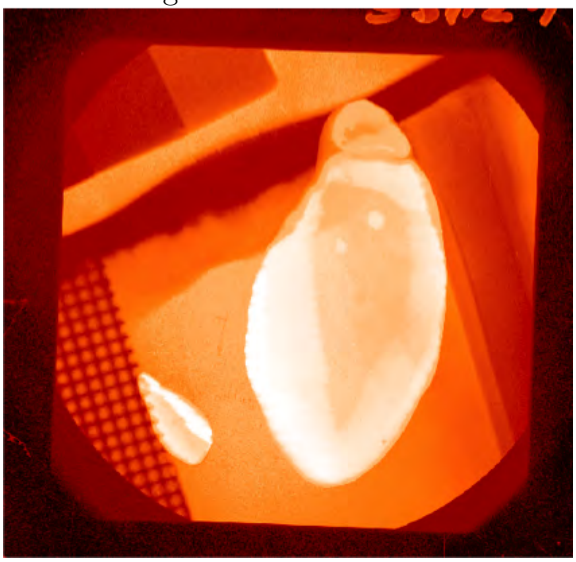

Figure B.10: Shot 63489

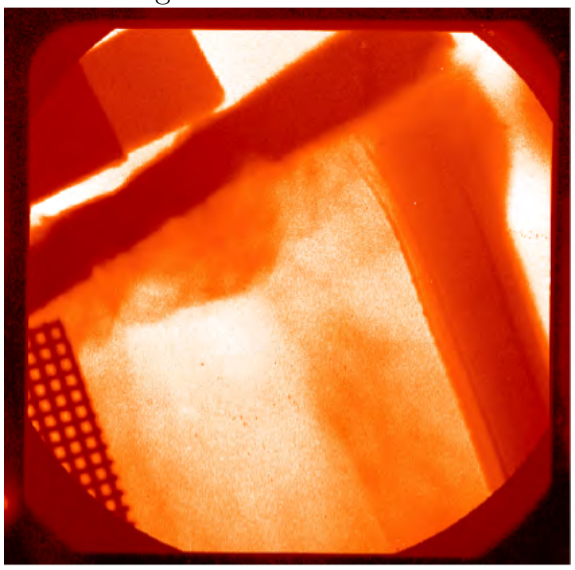

Figure B.11: Shot 63493

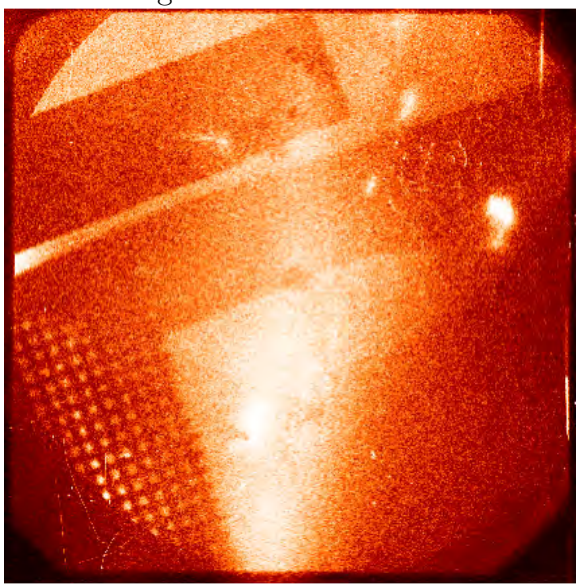

Figure B.12: Shot 63495

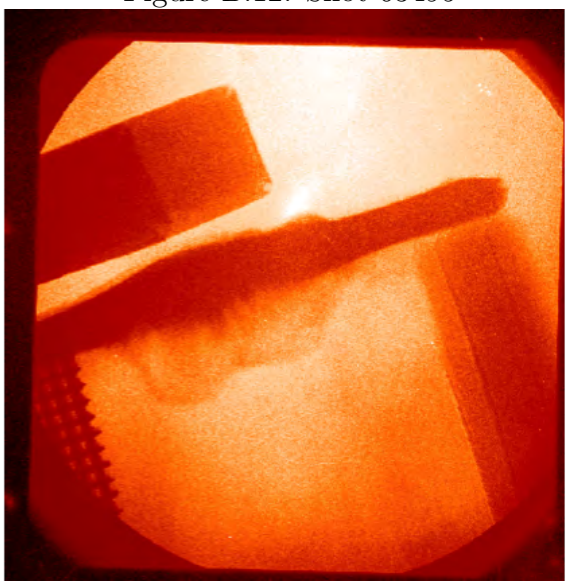

Other errors occasionally arise during film development. Figure B.9 shows damaged film with the large oval obscuring part of the data.

Although this is not an error in the radiography, images often show errors in the main target. Shot 63489 shown in Figure B.10 seems to clearly show the effects of a large amount of preheat. The Al wall has expanded and a denser material seems to be coming from the acrylic wall, as discussed in Chapter V. While the radiograph shown in Figure B.12 also has a good signal, the shock structure reveals the potential for target misalignment. The two hump structure is likely due to unevenness in the flow which may occur if the drive foil is not irradiated evenly. The effects of target or Al wall misalignment are also shown in the radiographs of the next section and discussed in Chapter V.

B.4 Experimental Campaign : July 19, 2012

Table B.4: Radiography overview : July 19, 2012

SHOT# (RID)	Radiography?	Pieces of Film	Comments
66797 (39466)	Yes	6	Dual
66798 (39467)	Yes	3	Dual
66799 (39468)	Yes	3	
66800 (39469)	Yes	6	Dual
66801 (39470)	Yes	3	
66802 (39471)	Yes	6	Dual
66803 (39472)	Yes	4/6	Dual
66805 (39473)	Yes	3	
66807 (39474)	Yes	3	
66809 (39475)	Yes	6	Dual
66810 (39476)	Yes	6	Dual
66811 (40453)	Yes	3	
66814 (40454)	Yes	0	Never found after shot day

Figure B.13: Shot 66798

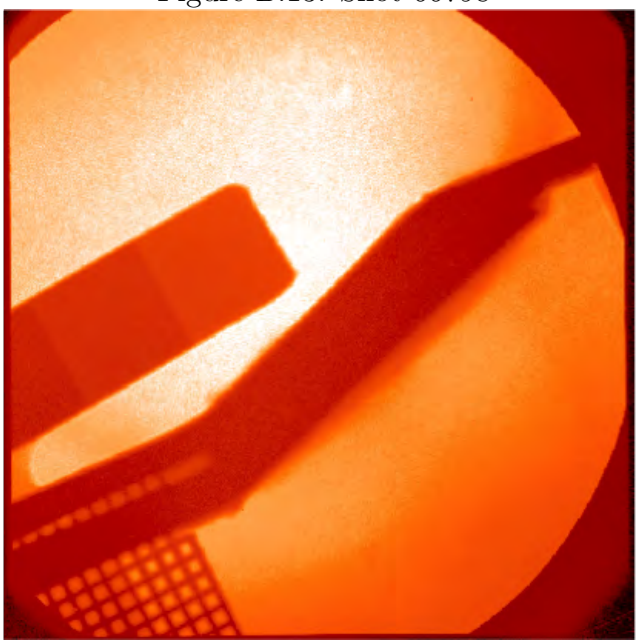

Figure B.14: Orthogonal views of shot 66800

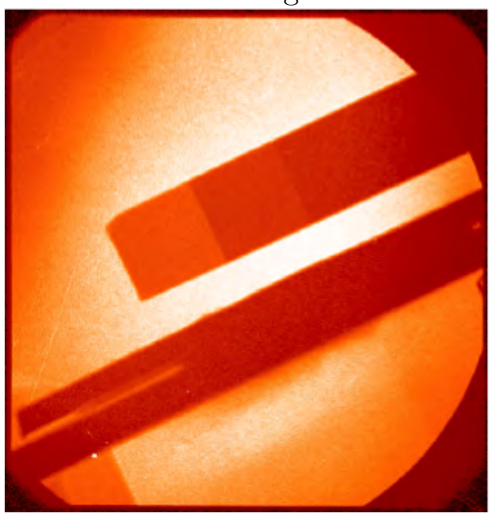

(a) View of $\hat{Y}$-$\hat{Z}$ plane

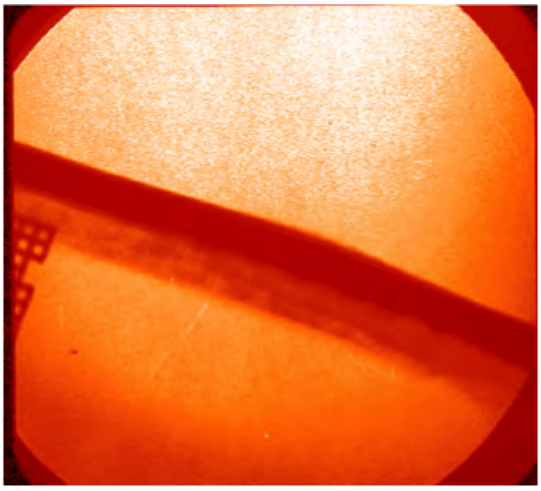

(b) View of $\hat{X}$-$\hat{Z}$ plane

APPENDIX C

Omega Laser Facility campaign specifications

This appendix contains the documents that detail parameters used by the laser facility. In each section, these documents, called Shot Request Forms (SRFs), are shown for a representative shot from each campaign. The SRF contains specifications for laser beam energy, pointing, and timing; diagnostic setup, pointing, and timing if applicable; and target identification, location, and orientation in the chamber. It is included for any technical data that may be of interest, such as temporal pulse shaping, relevant to the Omega-60 facility.

C.1 August 5, 2010 - RID 31864 - For Radiography and SOP

Report for RID 31864 Last Modified: [05-Aug-2010 08:07:49] -- Shot Number: 59001 at 05-Aug-2010 11:26:14

General / 31864

Last Updated:

Shot Scope	OMEGA Only		
Campaign	NLUF	**Planned Date**	05-Aug-2010
Series Name	RevRad	**Shot Series**	1
PI List	Drake/Paul// Kuranz/Carolyn// Loupias/Berenice//	**Shot Type**	Type 6: No Yield or Low Yield, Neutron Yield 1D predicted* to be less than 1e10
		1-D Yield	
		Expected Yield	
		Primary Objective	To produce and diagnose a radiative reverse shock
		Secondary Objective	
Special Instructions			
Abort Criteria	Abort on anything		

Driver / 31864

Last Updated:

Driver	Status	Pulse Shape	Request #	Timing Shift	Leg	X / Y Modulation
SSD	ON	SG1018		-34 ns		Max / Max
Main	OFF			0 ns		
Backlighter	ON	SG1017		0 ns	LEG1	
UV Fiducial	OFF					
Special Instructions						

Beams / 31864

Last Updated:

16 beam(s) are configured, 16 beam(s) go to target.									
Beams	**Group Name**	**Energy**	**Pointing**	**Focusing**	**Beam Delay (ns)**	**DPP**	**DPR**	**Termination**	**Report Group**
11,15-17,10,46	Backlighter	425 J/Beam (UV)	12020 um / 64.47 / 343.6	-800 um (spot size)	0	none	Yes	BL Target	A
21,23,25,27,29,35,39,30,50,64	Drive	450 J/Beam (UV)	4710 um / 147.74 / 19.62	0 mm (lens position)	0	SG4	Yes	Target	B

TIM / 31864

Last Updated:

Location	Priority	Description	Instrument PI/Specialist/Technician	
TIM 1	Secondary	XR Framing Camera - 4	Sorce, C., Bahr, R., Tellinghuisen, J.	Operating Procedures
TIM 3	Primary	LLNL TIM Target Positioner System - 1	Ayers, S., Sorce, C., Tellinghuisen, J.	Operating Procedures
TIM 4	Secondary	XR Framing Camera - 3	Sorce, C., Bahr, R., Tellinghuisen, J.	Operating Procedures
TIM 5	Primary	Off-Axis ASBO Telescope - 1	Park, H., Sorce, A., Kendrick, J.	Operating Procedures
TIM 6	Primary	Static Pinhole Camera Array - TIM_6	Sorce, C., Whiting, N., Tellinghuisen, J.	Operating Procedures

Fixed Diagnostics / 31864

Last Updated:

Port	Priority	Description	Instrument PI/Specialist/Technician	
	Primary	Active Shock Break Out Diagnostic (F)	Boehly, T., Sorce, A., Kendrick, J.	Operating Procedures
H16I	Primary	Dante (1)	May, M., Whiting, N., Tellinghuisen, J.	Operating Procedures
P2B	Secondary	Henway XR Spectrometer (1)	May, M., Tellinghuisen, J., Burke, M.	Operating Procedures
	Primary	Streak Optical Pyrometer (F)	Boehly, T., Sorce, A., Kendrick, J.	Operating Procedures
H8C	Secondary	XR Pinhole Camera (H8)	Marshall, F., Mastrosimone, D., Ruth, B.	Operating Procedures
P11D	Secondary	XR Pinhole Camera (P11)	Marshall, F., Mastrosimone, D., Ruth, B.	Operating Procedures
H12C	Secondary	XR Pinhole Camera (H12)	Marshall, F., Mastrosimone, D., Ruth, B.	Operating Procedures
H13C	Secondary	XR Pinhole Camera (H13)	Marshall, F., Mastrosimone, D., Ruth, B.	Operating Procedures

Static Pinhole Camera Array TIM_6 (SPCA) / TIM 6 Operating Procedures

Frame/Front End

	Make selections in one column only	
Nosecone Type	○ LLE	◉ LLNL
Cart Assembly		
Magnification		MPBL
Pinhole Size		other 9 mm
Blast Shield		other 20 mil Be + 3 mil PP
Standoff Distance	in.	9 in.
Frame Type		Straight
Pinhole Substrate	Ta	Ta
Rear Filter		20 mil Be

Detector Info

Detector Pack	
Detector Filter	Be
Detector Type	
# of Detectors	3

IP Scanning Parameters

Scan Time	Min.
Sensitivity	
Pixel Size	μm

Steering

Make selections in one row only				
◉	**Target Chamber Center**			
○	**Radius** um	**Theta**	**Phi**	
○	**Distance** um toward **Port**			

Comments/Requirements

Film pack: Agfa D8 Film + Black Kapton + IP.

Blast Shield: 20 mil Be + 3 mil
PP
Rear Filter: 20 mil Be

Off-Axis ASBO Telescope 1 (OATEL) / TIM 5 Operating Procedures

Axis

Select Axis	P6–P7: Theta = 106.03 deg, Phi = 260.28 deg

Steering

Make selections in one row only				
◉	**Target Chamber Center**			
○	**Radius** um	**Theta**	**Phi**	
○	**Distance** um toward **Port**			

C.2 June 15, 2011 - RID 35577 - For Thomson scattering

Report for RID 35577 Last Modified: [15-Jun-2011 11:43:12] -- Shot Number: 62630 at 15-Jun-2011 10:18:43

General / 35577

Last Updated:

Shot Scope	OMEGA Only		
Campaign	NLUF	**Planned Date**	15-Jun-2011
Series Name	RevRad	**Shot Series**	1
PI List	Drake/Paul// Kuranz/Carolyn// Loupias/Berenice// Ross/James/924-422-7290/ Sorce/Charles/50134/	**Shot Type**	Type 6: No Yield or Low Yield, Neutron Yield 1D predicted* to be less than 1e10
		1-D Yield	
		Expected Yield	
		Primary Objective	To produce and diagnose a radiative reverse shock
		Secondary Objective	
Special Instructions	Install full aperture 3w waveplate in Beam 41 set to 20 degrees. There will be a calorimeter in the opposing beam port (Beam 18).		
Abort Criteria	Abort on anything		

Driver / 35577

Last Updated:

19 beam(s) are configured, 10 beam(s) go to target.

Beams	Group Name	Energy	Pointing	Focusing	Beam Delay (ns)	DPP	DPR	Termination	Report Group
12	Ride Along for P510	20 J/Beam (UV)-FCC Detune	tcc	0 mm (lens position)	0	none	No	F-Cal	B
22,26,52,55,56,58,61,65,68,60	Drive	450 J/Beam (UV)	3905 um / 32.257 / 199.61	0 mm (lens position)	0	SG4	Yes	Target	A
32,37	Ridealong for timing	450 J/Beam (UV)	tcc	0 mm (lens position)	0	none	No	F-Cal	J
42,44,45,47,40	Ridealong for P510 setup	450 J/Beam (UV)	12542 um / 116.87 / 162.95	-800 um (spot size)	0	none	Yes	F-Cal	B
46	Ride Along	450 J/Beam (UV)	tcc	0 mm (lens position)	0	none	Yes	UVDT Dump	K

TIM / 35577

Last Updated:

Location	Priority	Description	Instrument PI/Specialist/Technician	
TIM 1	Primary	CEA XR Diode Array - 1	Villette, B., Armstrong, W.	Operating Procedures
TIM 4	Primary	TSS Alignment Carts - 4	Sorce, C., Katz, J., Tellinghuisen, J.	Operating Procedures
TIM 5	Primary	Off-Axis ASBO Telescope - 1	Park, H., Sorce, A., Kendrick, J.	Operating Procedures
TIM 6	Primary	Thomson Scattering System - 1	Froula, D., Katz, J.	Operating Procedures

Fixed Diagnostics / 35577

Last Updated:

Port	Priority	Description	Instrument PI/Specialist/Technician	
	Primary	Active Shock Break Out Diagnostic (F)	Boehly, T., Sorce, A., Kendrick, J.	Operating Procedures
	Primary	Electron Plasma Wave (ROSS)	Froula, D., Katz, J.	Operating Procedures
P2B	Secondary	Henway XR Spectrometer (1)	May, M., Tellinghuisen, J., Burke, M.	Operating Procedures
	Primary	Ion Acoustic Wave (ROSS)	Froula, D., Katz, J.	Operating Procedures
	Primary	Streak Optical Pyrometer (F)	Boehly, T., Sorce, A., Kendrick, J.	Operating Procedures
	Primary	Two Plasmon Decay (Imager)	Froula, D., Katz, J.	Operating Procedures
H8C	Secondary	XR Pinhole Camera (H8)	Marshall, F., Mastrosimone, D., Ruth, B.	Operating Procedures
H13C	Secondary	XR Pinhole Camera (H13)	Marshall, F., Mastrosimone, D., Ruth, B.	Operating Procedures
P11D	Secondary	XR Pinhole Camera (P11)	Marshall, F., Mastrosimone, D., Ruth, B.	Operating Procedures
H4F	Secondary	XR Pinhole Camera (H4)	Marshall, F., Mastrosimone, D., Ruth, B.	Operating Procedures
H12C	Secondary	XR Pinhole Camera (H12)	Marshall, F., Mastrosimone, D., Ruth, B.	Operating Procedures

C.3 June 15, 2011 - RID 35588 - For radiography

Report for RID 35588 Last Modified: [15-Jun-2011 17:42:54] -- Shot Number: 62636 at 15-Jun-2011 17:20:40

General / 35588

Last Updated:

Shot Scope	OMEGA Only		
Campaign	NLUF	**Planned Date**	15-Jun-2011
Series Name	RevRad	**Shot Series**	12
PI List	Drake/Paul// Kuranz/Carolyn// Loupias/Berenice// Froula/Dustin/3-3212/ Sorce/Charles/50134/	**Shot Type**	Type 6: No Yield or Low Yield, Neutron Yield 1D predicted* to be less than 1e10
		1-D Yield	
		Expected Yield	
		Primary Objective	To produce and diagnose a radiative reverse shock
		Secondary Objective	
Special Instructions			
Abort Criteria	Abort on anything		

Driver / 35588

Last Updated:

18 beam(s) are configured, 15 beam(s) go to target.

Beams	Group Name	Energy	Pointing	Focusing	Beam Delay (ns)	DPP	DPR	Termination	Report Group
22,26,52,55,56,58,61,65,68,60	Drive	450 J/Beam (UV)	3905 um / 32.257 / 199.61	0 mm (lens position)	0	SG4	Yes	Target	A
32,37	Ridealong for timing	450 J/Beam (UV)	tcc	0 mm (lens position)	0	none	No	F-Cal	J
42,44	BL	450 J/Beam (UV)	12542 um / 116.87 / 162.95	800 um (spot size)	0	none	Yes	Target	B
45,47,40	BL	450 J/Beam (UV)	12542 um / 116.87 / 162.95	-800 um (spot size)	0	none	Yes	Target	B
46	Ride Along	450 J/Beam (UV)	tcc	0 mm (lens position)	0	none	Yes	UVDT Dump	K

TIM / 35588

Last Updated:

Location	Priority	Description	Instrument PI/Specialist/Technician	
TIM 1	Primary	CEA XR Diode Array - 1	Villette, B., Armstrong, W.	Operating Procedures
TIM 2	Secondary	Static Pinhole Camera Array - TIM_2	Sorce, C., Whiting, N., Tellinghuisen, J.	Operating Procedures
TIM 3	Primary	LLNL TIM Target Positioner System - 1	Ayers, S., Sorce, C., Tellinghuisen, J.	Operating Procedures
TIM 4	Primary	Static Pinhole Camera Array - TIM_4	Sorce, C., Whiting, N., Tellinghuisen, J.	Operating Procedures
TIM 5	Primary	Off-Axis ASBO Telescope - 1	Park, H., Sorce, A., Kendrick, J.	Operating Procedures

Fixed Diagnostics / 35588

Last Updated:

Port	Priority	Description	Instrument PI/Specialist/Technician	
	Primary	Active Shock Break Out Diagnostic (F)	Boehly, T., Sorce, A., Kendrick, J.	Operating Procedures
P2B	Secondary	Henway XR Spectrometer (1)	May, M., Tellinghuisen, J., Burke, M.	Operating Procedures
	Primary	Streak Optical Pyrometer (F)	Boehly, T., Sorce, A., Kendrick, J.	Operating Procedures
H13C	Secondary	XR Pinhole Camera (H13)	Marshall, F., Mastrosimone, D., Ruth, B.	Operating Procedures
H12C	Secondary	XR Pinhole Camera (H12)	Marshall, F., Mastrosimone, D., Ruth, B.	Operating Procedures
P11D	Secondary	XR Pinhole Camera (P11)	Marshall, F., Mastrosimone, D., Ruth, B.	Operating Procedures
H8C	Secondary	XR Pinhole Camera (H8)	Marshall, F., Mastrosimone, D., Ruth, B.	Operating Procedures
H4F	Secondary	XR Pinhole Camera (H4)	Marshall, F., Mastrosimone, D., Ruth, B.	Operating Procedures

C.4 September 8, 2010 - RID 37070

Beams / 37070

Last Updated:

16 beam(s) are configured, 15 beam(s) go to target.									
Beams	**Group Name**	**Energy**	**Pointing**	**Focusing**	**Beam Delay (ns)**	**DPP**	**DPR**	**Termination**	**Report Group**
22,26,52,55,56,58,61,65,68,60	Drive	450 J/Beam (UV)	3905 um / 32.257 / 199.61	0 mm (lens position)	0	SG4	Yes	Target	A
42,44	BL	450 J/Beam (UV)	12542 um / 116.87 / 162.95	800 um (spot size)	0	none	Yes	Target	B
45,47,40	BL	450 J/Beam (UV)	12542 um / 116.87 / 162.95	-800 um (spot size)	0	none	Yes	Target	B
46	Ride Along	450 J/Beam (UV)	tcc	0 mm (lens position)	0	none	Yes	UVDT Dump	K

TIM / 37070

Last Updated:

Location	**Priority**	**Description**	**Instrument PI/Specialist/Technician**	
TIM 1	Secondary	XR Framing Camera - 3	Sorce, C., Bahr, R., Tellinghuisen, J.	Operating Procedures
TIM 2	Secondary	Static Pinhole Camera Array - TIM_2	Sorce, C., Whiting, N., Tellinghuisen, J.	Operating Procedures
TIM 3	Primary	LLNL TIM Target Positioner System - 1	Ayers, S., Sorce, C., Tellinghuisen, J.	Operating Procedures
TIM 4	Primary	Static Pinhole Camera Array - TIM_4	Sorce, C., Whiting, N., Tellinghuisen, J.	Operating Procedures

Fixed Diagnostics / 37070

Last Updated:

Port	**Priority**	**Description**	**Instrument PI/Specialist/Technician**	
P2B	Secondary	Henway XR Spectrometer (1)	May, M., Tellinghuisen, J., Burke, M.	Operating Procedures
H8C	Secondary	XR Pinhole Camera (H8)	Marshall, F., Mastrosimone, D., Ruth, B.	Operating Procedures
H12C	Secondary	XR Pinhole Camera (H12)	Marshall, F., Mastrosimone, D., Ruth, B.	Operating Procedures
H13C	Secondary	XR Pinhole Camera (H13)	Marshall, F., Mastrosimone, D., Ruth, B.	Operating Procedures
H4F	Secondary	XR Pinhole Camera (H4)	Marshall, F., Mastrosimone, D., Ruth, B.	Operating Procedures
P11D	Secondary	XR Pinhole Camera (P11)	Marshall, F., Mastrosimone, D., Ruth, B.	Operating Procedures

Beams / 37070

Last Updated:

16 beam(s) are configured, 15 beam(s) go to target.									
Beams	**Group Name**	**Energy**	**Pointing**	**Focusing**	**Beam Delay (ns)**	**DPP**	**DPR**	**Termination**	**Report Group**
22,26,52,55,56,58,61,65,68,60	Drive	450 J/Beam (UV)	3905 um / 32.257 / 199.61	0 mm (lens position)	0	SG4	Yes	Target	A
42,44	BL	450 J/Beam (UV)	12542 um / 116.87 / 162.95	800 um (spot size)	0	none	Yes	Target	B
45,47,40	BL	450 J/Beam (UV)	12542 um / 116.87 / 162.95	-800 um (spot size)	0	none	Yes	Target	B
46	Ride Along	450 J/Beam (UV)	tcc	0 mm (lens position)	0	none	Yes	UVDT Dump	K

TIM / 37070

Last Updated:

Location	**Priority**	**Description**	**Instrument PI/Specialist/Technician**	
TIM 1	Secondary	XR Framing Camera - 3	Sorce, C., Bahr, R., Tellinghuisen, J.	Operating Procedures
TIM 2	Secondary	Static Pinhole Camera Array - TIM_2	Sorce, C., Whiting, N., Tellinghuisen, J.	Operating Procedures
TIM 3	Primary	LLNL TIM Target Positioner System - 1	Ayers, S., Sorce, C., Tellinghuisen, J.	Operating Procedures
TIM 4	Primary	Static Pinhole Camera Array - TIM_4	Sorce, C., Whiting, N., Tellinghuisen, J.	Operating Procedures

Fixed Diagnostics / 37070

Last Updated:

Port	**Priority**	**Description**	**Instrument PI/Specialist/Technician**	
P2B	Secondary	Henway XR Spectrometer (1)	May, M., Tellinghuisen, J., Burke, M.	Operating Procedures
H8C	Secondary	XR Pinhole Camera (H8)	Marshall, F., Mastrosimone, D., Ruth, B.	Operating Procedures
H12C	Secondary	XR Pinhole Camera (H12)	Marshall, F., Mastrosimone, D., Ruth, B.	Operating Procedures
H13C	Secondary	XR Pinhole Camera (H13)	Marshall, F., Mastrosimone, D., Ruth, B.	Operating Procedures
H4F	Secondary	XR Pinhole Camera (H4)	Marshall, F., Mastrosimone, D., Ruth, B.	Operating Procedures
P11D	Secondary	XR Pinhole Camera (P11)	Marshall, F., Mastrosimone, D., Ruth, B.	Operating Procedures

C.5 July 19, 2012 - RID 39471

Report for RID 39471 Last Modified: [24-Jul-2012 14:09:17] -- Shot Number: 66802 at 19-Jul-2012 13:33:33

General / 39471

Last Updated:

Shot Scope	OMEGA Only		
Campaign	NLUF	**Planned Date**	19-Jul-2012
Series Name	RevRad	**Shot Series**	6
PI List	Drake/Paul// Kuranz/Carolyn// Loupias/Berenice// Jarrott/Charlie//	**Shot Type**	Type 6: No Yield or Low Yield, Neutron Yield 1D predicted* to be less than 1e10
		1-D Yield	
		Expected Yield	
		Primary Objective	To produce and diagnose a radiative reverse shock
		Secondary Objective	
Special Instructions			
Abort Criteria	Abort on anything		

Driver / 39471

Last Updated:

Driver	Status	Pulse Shape	Request #	Timing Shift	Leg	X / Y Modulation
SSD	ON	SG1018		-40 ns		Max / Max
Main	OFF			0 ns		
Backlighter	ON	SG1014		0 ns	LEG1	
UV Fiducial	OFF					
Special Instructions						

Beams / 39471

Last Updated:

19 beam(s) are configured, 18 beam(s) go to target.									
Beams	**Group Name**	**Energy**	**Pointing**	**Focusing**	**Beam Delay (ns)**	**DPP**	**DPR**	**Termination**	**Report Group**
11,13,14,18	BL_2	450 J/Beam (UV)	12575 um / 73.1 / 80.74	0 mm (lens position)	0	SG4	Yes	Target	C
15-17,10	BL_1	450 J/Beam (UV)	12575 um / 63.43 / 342	0 mm (lens position)	0	SG4	Yes	Target	B
22,26,52,55,56,58,61,65,68,60	Drive	450 J/Beam (UV)	3910 um / 32.26 / 199.61	0 mm (lens position)	0	SG4	Yes	Target	A
46	Ride Along	450 J/Beam (UV)	tcc	0 mm (lens position)	0	none	Yes	UVDT Dump	K

TIM / 39471

Last Updated:

Location	Priority	Description	Instrument PI/Specialist/Technician	
TIM 1	Primary	CEA XR Diode Array - 1	Villette, B., Armstrong, W.	Operating Procedures
TIM 2	Primary	LLNL TIM Target Positioner System - 2	Ayers, S., Sorce, C., Tellinghuisen, J.	Operating Procedures
TIM 3	Primary	LLNL TIM Target Positioner System - 1	Ayers, S., Sorce, C., Tellinghuisen, J.	Operating Procedures
TIM 4	Secondary	High Energy Radiography Imager - 1	Maddox, B., Whiting, N., Tellinghuisen, J.	Operating Procedures
TIM 5	Primary	Static Pinhole Camera Array - TIM_5	Sorce, C., Whiting, N., Tellinghuisen, J.	Operating Procedures
TIM 6	Primary	Static Pinhole Camera Array - TIM_6	Sorce, C., Whiting, N., Tellinghuisen, J.	Operating Procedures

Fixed Diagnostics / 39471

Last Updated:

Port	Priority	Description	Instrument PI/Specialist/Technician	
H10	Secondary	Hard XR Detector (1-4)	Stoeckl, C., Mileham, C., Katz, J.	Operating Procedures
H8C	Secondary	XR Pinhole Camera (H8)	Marshall, F., Mastrosimone, D., Ruth, B.	Operating Procedures
H12C	Secondary	XR Pinhole Camera (H12)	Marshall, F., Mastrosimone, D., Ruth, B.	Operating Procedures
H13C	Secondary	XR Pinhole Camera (H13)	Marshall, F., Mastrosimone, D., Ruth, B.	Operating Procedures
H4F	Secondary	XR Pinhole Camera (H4)	Marshall, F., Mastrosimone, D., Ruth, B.	Operating Procedures
P11D	Secondary	XR Pinhole Camera (P11)	Marshall, F., Mastrosimone, D., Ruth, B.	Operating Procedures

BIBLIOGRAPHY

BIBLIOGRAPHY

[1] K. U. Akli, R. B. Stephens, M. H. Key, T. Bartal, F. N. Beg, S. Chawla, C. D. Chen, R. Fedosejevs, R. R. Freeman, H. Friesen, E. Giraldez, J. S. Green, D. S. Hey, D. P. Higginson, J. Hund, L. C. Jarrott, G. E. Kemp, J. A. King, A. Kryger, K. Lancaster, S. LePape, A. Link, T. Ma, A. J. Mackinnon, A. G. MacPhee, H. S. McLean, C. Murphy, P. A. Norreys, V. Ovchinnikov, P. K. Patel, Y. Ping, H. Sawada, D. Schumacher, W. Theobald, Y. Y. Tsui, L. D. Van Woerkom, M. S. Wei, B. Westover, and T. Yabuuchi. Hot electron generation and transport using k emission. *Journal of Physics: Conference Series*, 244(2):022026, 2010.

[2] L. K. Ang, Y. Y. Lau, R. M. Gilgenbach, H. L. Spindler, J. S. Lash, and S. D. Kovaleski. Surface instability of multipulse laser ablation on a metallic target. *Journal of Applied Physics*, 83(8):4466–4471, 1998.

[3] P.J. Armitage and M. Livio. Hydrodynamics of the Stream-Disk Impact in Interacting Binaries. *Astrophysical Journal*, 493:898, January 1998.

[4] D. Babonneau, M. Primout, F. Girard, J.-P. Jadaud, M. Naudy, B. Villette, S. Depierreux, C. Blancard, G. Faussurier, K. B. Fournier, L. Suter, R. Kauffman, S. Glenzer, M. C. Miller, J. Grun, and J. Davis. Efficient multi-kev x-ray sources from laser-exploded metallic thin foils. *Physics of Plasmas*, 15(9):092702, 2008.

[5] K.R. Bell and D.N.C. Lin. Using FU Orionis outbursts to constrain self-regulated protostellar disk models. *Astrophysical Journal*, 427(2, Part 1):987–1004, Jun 1 1994.

[6] G. Birkhoff, D. P. MacDougall, E. M. Pugh, and S. G. Taylor. Explosives with lined cavities. *Journal of Applied Physics*, 19(6):563–582, 1948.

[7] D. V. Bisikalo, A. A. Boyarchuk, P. V. Kaigorodov, and O. A. Kuznetsov. Morphology of the Interaction Between the Stream and Cool Accretion Disk in a Semidetached Binary System. *Astronomy Reports*, 47:809–820, October 2003.

[8] J.M. Blondin, M.T. Richards, and M.L. Malinowski. Hydrodynamic simulations of the mass transfer in Algol. *Astrophysical Journal*, 445:939–946, June 1995.

[9] G. Bodo, S. Massaglia, P. Rossi, E. Trussoni, and A. Ferrari. Kelvin–helmholtz instabilities in radiating flows. *Physics of Fluids A: Fluid Dynamics*, 5(2):405–411, 1993.

[10] S. Bouquet, C. Stéhlé, M. Koenig, J.-P. Chièze, A. Benuzzi-Mounaix, D. Batani, S. Leygnac, X. Fleury, H. Merdji, C. Michaut, F. Thais, N. Grandjouan, T. Hall, E. Henry, V. Malka, and J.-P. J. Lafon. Observation of laser driven supercritical radiative shock precursors. *Phys. Rev. Lett.*, 92:225001, Jun 2004.

[11] J. L Bourgade, B. Villette, J. L. Bocher, J. Y. Boutin, S. Chiche, N. Dague, D. Gontier, J. P. Jadaud, B. Savale, R. Wrobel, and R.E. Turner. Dmx: An absolutely calibrated time-resolved broadband soft x-ray spectrometer designed for mj class laser-produced plasmas (invited). *Review of Scientific Instruments*, 72(1):1173–1182, 2001.

[12] J. C. Bozier, G. Thiell, J. P. Le Breton, S. Azra, M. Decroisette, and D. Schirmann. Experimental observation of a radiative wave generated in xenon by a laser-driven supercritical shock. *Phys. Rev. Lett.*, 57:1304–1307, Sep 1986.

[13] J. J. Carroll-Nellenback, B. Shroyer, A. Frank, and C. Ding. Efficient parallelization for amr mhd multiphysics calculations; implementation in astrobear. *Journal of Computational Physics*, 236(0):461 – 476, 2013.

[14] C. D. Chen, P. K. Patel, D. S. Hey, A. J. Mackinnon, M. H. Key, K. U. Akli, T. Bartal, F. N. Beg, S. Chawla, H. Chen, R. R. Freeman, D. P. Higginson, A. Link, T. Y. Ma, A. G. MacPhee, R. B. Stephens, L. D. Van Woerkom, B. Westover, and M. Porkolab. Bremsstrahlung and k alpha fluorescence measurements for inferring conversion efficiencies into fast ignition relevant hot electrons. *Physics of Plasmas*, 16(8):082705, 2009.

[15] C.D. Chen, J.A. King, M. H. Key, K.U. Akli, F.N. Beg, H. Chen, R.R. Freeman, A. Link, A.J. Mackinnon, A.G. MacPhee, P.K. Patel, M. Porkolab, R.B. Stephens, and L. D. Van Woerkom. A bremsstrahlung spectrometer using k-edge and differential filters with image plate dosimeters. *Review of Scientific Instruments*, 79(10):10E305–10E305–3, 2008.

[16] D. Chochol, A. Vittone, L. Milano, and L. Rusconi. The symbiotic eclipsing binary CI CYG - an Algol symbiotic system. *Astronomy & Astrophysics*, 140:91–104, November 1984.

[17] S.Roy Choudhury. Nonlinear evolution of the kelvin–helmholtz instability of supersonic tangential velocity discontinuities. *Journal of Mathematical Analysis and Applications*, 214(2):561 – 586, 1997.

[18] J.A. Crawford and R.P. Kraft. An Intrepretation of AE Aquarii. *Astrophysical Journal*, 123:44, January 1956.

[19] A. Dalgarno and R.A. McCray. Heating and Ionization of HI Regions. *Annual Review of Astronomy and Astrophysics*, 10:375, 1972.

[20] R. Dgani, M. Livio, and N. Soker. On the stream-accretion disk interaction - Response to increased mass-transfer rate. *Astrophysical Journal*, 336(1, Part 1):350–359, 1989.

[21] F. Doss, R.P. Drake, C.C. Kuranz, C.M. Huntington, C.M. Krauland, A. Visco, M.J. Grosskopf, and D. Marion. Radiative Shocks with Dense Post-Shock Layers at the Omega Laser. In *American Astronomical Society Meeting Abstracts #216*, volume 41 of *Bulletin of the American Astronomical Society*, page 410.03, May 2010.

[22] F. W. Doss, R. P. Drake, and C. C. Kuranz. Repeatability in radiative shock tube experiments. *High Energy Density Physics*, 6(2, Sp. Iss. SI):157–161, 2010. 2nd International Conference on High Energy Density Physics, Austin, TX, MAY 19-22, 2009.

[23] F. W. Doss, R. P. Drake, and E. S. Myra. Oblique radiative shocks, including their interactions with nonradiative polytropic shocks. *Physics of Plasmas*, 18(5):056901, 2011.

[24] F. W. Doss, R. P. Drake, and H. F. Robey. Early-Time Stability of Decelerating Shocks. *ArXiv e-prints*, June 2009.

[25] F.W. Doss, R.P. Drake, H.F. Robey, and C.C. Kuranz. Wall shock in high-energy-density shock tube experiments. *Physics of Plasmas*, 16(112705), 2009.

[26] F.W. Doss, H.F. Robey, R.P. Drake, and C.C. Kuranz. Wall shocks in high-energy-density shock tube experiments. *Physics of Plasmas*, 16(11):112705, November 2009.

[27] R. P. Drake. Radiative shocks in astrophysics and the laboratory. *Astrophysics and Space Science*, 298(1-2):49–59, Jun 2005. 5th International Conference on High Energy Density Laboratory Astrophysics, Tucson, AZ, MAR 10-13, 2004.

[28] R. P. Drake. *High-Energy-Density Physics: Fundamentals, Inertial Fusion, and Experimental Astrophysics*. Springer-Verlag, Berlin, 2006.

[29] R. P. Drake. Theory of radiative shocks in optically thick media. *Physics of Plasmas*, 14(4):043301, 2007.

[30] R.P. Drake, D.R. Leibrandt, E.C. Harding, C.C. Kuranz, M.A. Blackburn, H.F. Robey, B.A. Remington, M.J. Edwards, A.R. Miles, T.S. Perry, R. Wallace, H. Louis, J. Knauer, and D. Arnett. Nonlinear mixing behavior of the three-dimensional Rayleigh-Taylor instability at a decelerating interface. *Physics of Plasmas*, 11(5):2829–2837, 2004.

[31] E. Falize, C. Michaut, and S. Bouquet. Similarity Properties and Scaling Laws of Radiation Hydrodynamic Flows in Laboratory Astrophysics. *Astrophysical Journal*, 730:96, April 2011.

[32] É. Falize, A. Ravasio, B. Loupias, A. Dizière, C.D. Gregory, C. Michaut, C. Busschaert, C. Cavet, and M. Koenig. High-energy density laboratory astrophysics studies of accretion shocks in magnetic cataclysmic variables. *High Energy Density Physics*, 8(1):1 – 4, 2012.

[33] R.A. Forties and F.J. Marshall. In situ characterization of high-intensity laser beams on omega. *Review of Scientific Instruments*, 76(7):073505–073505–4, 2005.

[34] K. B. Fournier, C. G. Constantin, J. Poco, M. C. Miller, C. A. Back, L. J. Suter, J. Satcher, J. F. Davis, and J. Grun. Efficient multi-keV x-ray sources from Ti-doped aerogel targets. In G. A. Kyrala, J.-C. J. Gauthier, C. A. MacDonald, and A. M. Khounsary, editors, *Society of Photo-Optical Instrumentation Engineers (SPIE) Conference Series*, volume 5196 of *Society of Photo-Optical Instrumentation Engineers (SPIE) Conference Series*, pages 194–204, January 2004.

[35] F. Girard, J. P. Jadaud, M. Naudy, B. Villette, D. Babonneau, M. Primout, M. C. Miller, R. L. Kauffman, L. J. Suter, J. Grun, and J. Davis. Multi-kev x-ray conversion efficiencies of laser-preexploded titanium foils. *Physics of Plasmas*, 12(9):092705, 2005.

[36] M. J. Grosskopf, D. C. Marion, R. P. Drake, C. C. Kuranz, F. W. Doss, A. J. Visco, C. M. Huntington, C. M. Krauland, C. A. Di Stefano, and E. C. Harding. Target fabrication at the University of Michigan. *Fusion Science and Technology*, 59(1):250–256, Jan 2011. 19th Target Fabrication Meeting, Orlando, FL, FEB 21-26, 2010.

[37] J.A. Halbleib, R.P. Kensek, G.D. Valdez, S.M. Seltzer, and M.J. Berger. Its: the integrated tiger series of electron/photon transport codes-version 3.0. *Nuclear Science, IEEE Transactions on*, 39(4):1025–1030, 1992.

[38] J. F. Hansen, H. F. Robey, R. I. Klein, and A. R. Miles. Experiment on the mass stripping of an interstellar cloud following shock passage. *Astrophysical Journal*, 662:379–388, 2007.

[39] E. C. Harding, R. P. Drake, Y. Aglitskiy, T. Plewa, A. L. Velikovich, R. S. Gillespie, J. L. Weaver, A. Visco, M. J. Grosskopf, and J. R. Ditmar. Laser driven supersonic flow over a compressible foam surface on the nike laser. *Physics of Plasmas*, 17(5):056310, 2010.

[40] C. A. Haynam, P. J. Wegner, J. M. Auerbach, M. W. Bowers, S. N. Dixit, G. V. Erbert, G. M. Heestand, M. A. Henesian, M. R. Hermann, K. S. Jancaitis, K. R. Manes, C. D. Marshall, N. C. Mehta, J. Menapace, E. Moses, J. R. Murray, M. C. Nostrand, C. D. Orth, R. Patterson, R. A. Sacks, M. J. Shaw, M. Spaeth, S. B. Sutton, W. H. Williams, C. C. Widmayer, R. K. White, S. T. Yang, and B. M. Van Wonterghem. National ignition facility laser performance status. *Appl. Opt.*, 46(16):3276–3303, Jun 2007.

[41] C. Hellier. The SW Sextantis stars. *New Astronomy Review*, 44:131–136, April 2000.

[42] F. V. Hessman. On the Occurrence of Stream Overflow in Cataclysmic Variables withAccretion Disks. *Astrophysical Journal*, 510:867–873, January 1999.

[43] M. Hirose, Y. Osaki, and S. Mineshige. Three-dimensional structure of accretion disks in close binary systems. *Publications of the Astronomical Society of Japan*, 43:809–821, December 1991.

[44] M. Koenig and T. Vinci. Radiative shocks: An opportunity to study laboratory astrophysics. *Physics of Plasmas*, 13:056504, 2006.

[45] R.P. Kraft. *Science*, 134(1433), 1961.

[46] W. Krzeminski and R.P. Kraft. Binary Stars among Cataclysmic Variables. V. Photoelectric and Spectroscopic Observations of the Ultra-Short Binary Nova WZ Sagittae. *Astrophysical Journal*, 140:921, October 1964.

[47] W. Krzeminski and J. Smak. Eruptive Binaries. III. The Recurrent Nova WZ Sagittae. *Acta Astronomica*, 21:133, 1971.

[48] C. C. Kuranz, B. E. Blue, R. P. Drake, H. F. Robey, J. F. Hansen, J. P. Knauer, M. J. Grosskopf, C. Krauland, and D. C. Marion. Dual, orthogonal backlit pinhole radiography in OMEGA experiments. *Review of Scientific Instruments*, (77):10E327, 2006.

[49] C. C. Kuranz, R. P. Drake, E. C. Harding, M. J. Grosskopf, H. F. Robey, B. A. Remington, M. J. Edwards, A. R. Miles, T. S. Perry, T. Plewa, N. C. Hearn, J. P. Knauer, D. Arnett, and D. R. Leibrandt. 2D Blast-wave-driven Rayleigh-Taylor instability: experiment and simulation. *Astrophysical Journal*, 696(1):749–759, 2009.

[50] C.C. Kuranz, F.W. Doss, R.P. Drake, M.J. Grosskopf, and H.F. Robey. Using wall shocks to measure preheat in laser-irradiated, high-energy-density, hydrodynamics experiments. *High Energy Density Physics*, 6(2):215 – 218, 2010. ¡ce:title¿ICHED 2009 - 2nd International Conference on High Energy Density Physics¡/ce:title¿.

[51] CC Kuranz, RP Drake, KK Dannenberg, PJ Susalla, DJ Kremer, T Boehly, and J Knauer. Preheat issues in hydrodynamic Hedla experiments. *Astrophysics and Space Science*, 298(1-2):267–271, JUN 2005. 5th International Conference on High Energy Density Laboratory Astrophysics, Tucson, AZ, MAR 10-13, 2004.

[52] N.E. Lanier, J.S. Cowan, and J. Workman. Characterization and cross calibration of Agfa D4, D7, and D8 and Kodak SR45 x-ray films against direct exposre film at 4.0 - 5.5 keV. *Rev. Sci. Instrum.*, 77(043504), 2006.

[53] G. Lanzafame, G. Belvedere, and D. Molteni. 3D simulations of the SS CYG accretion disc in the quiescent phase. *Monthly Notices of the Royal Astronomical Society*, 258:152–158, September 1992.

[54] G. Lanzafame, G. Belvedere, and D. Molteni. A Three-Dimensional Smoothed Particle Hydrodynamics Simulation of the Active Phase of Ss-Cygni Type Discs

and its Implications for the Mass Transfer Burst Model. *Monthly Notices of the Royal Astronomical Society*, 263:839, August 1993.

[55] J.T. Larsen and S.M. Lane. HYADES: a plasma hydrodynamics code for dense plasma studies. *J. Quant. Spectrosc. Radiat. Transfer*, 51(1):179–186, 1994.

[56] M. Livio. *The Interaction Between the Stream and the Accretion Disk*, page 243. World Scientific, 1993.

[57] M. Livio, N. Soker, and R. Dgani. On the stream-disk interaction in accreting compact objects. *Astrophysical Journal*, 305:267–280, June 1986.

[58] S. H. Lubow and F. H. Shu. Gas dynamics of semidetached binaries. *ASTROPHYSICAL JOURNAL*, 198:383–405, June 1975.

[59] S. H. Lubow and F. H. Shu. Gas dynamics of semidetached binaries. II - The vertical structure of the stream. *Astrophysical Journal Letters*, 207:L53–L55, July 1976.

[60] S.H. Lubow and F.H. Shu. On the dynamics of mass-transfer over an accretion disk. *Astrophysical Journal*, 340(2, Part 1):1064, May 15 1989.

[61] F.J. Marshall, T. Ohki, D. McInnis, Z. Ninkov, and J. Carbone. Imaging of laser–plasma x-ray emission with charge-injection devices. *Review of Scientific Instruments*, 72(1):713–716, 2001.

[62] R. G. McClarren, R. P. Drake, J. E. Morel, and J. P. Holloway. Theory of radiative shocks in the mixed, optically thick-thin case. *Physics of Plasmas*, 17(9):093301, September 2010.

[63] E. A. McLean, S. H. Gold, J. A. Stamper, R. R. Whitlock, S. P. Obenschain, B. H. Ripin, S. E. Bodner, M. J. Herbst, H. R. Griem, and S. J. Gitomer. Preheat studies for foils accelerated by ablation due to laser irradiation. *Physical Review Letters*, 45:1246–1249, October 1980.

[64] D. Mihalas and B. W. Mihalas. *Foundations of radiation hydrodynamics*. Oxford University Press, 1984.

[65] J. E. Miller, T. R. Boehly, A. Melchior, D. D. Meyerhofer, P. M. Celliers, J. H. Eggert, D. G. Hicks, C. M. Sorce, J. A. Oertel, and P. M. Emmel. Streaked optical pyrometer system for laser-driven shock-wave experiments on OMEGA. *Review of Scientific Instruments*, 78(3), Mar 2007.

[66] B. Paczynski. Evolutionary Processes in Close Binary Systems. *Annual Review of Astron and Astrophys*, 9:183, 1971.

[67] B. Paczynski. A model of accretion disks in close binaries. *Astrophysical Journal*, 216:822–826, September 1977.

[68] R. Paul Drake. Energy balance and structural regimes of radiative shocks in optically thick media. *Plasma Science, IEEE Transactions on*, 35(2):171–180, 2007.

[69] A.B. Reighard, R. P. Drake, K.K. Danneberg, D. J. Kremer, T.S. Perry, B.A. Remington, R.J. Wallace, D.D. Ryutov, J. Greenough, J. Knauer, T. Boehly, S. Bouquet, A. Calder, R. Rosner, B. Fryxell, D. Arnett, M. Koenig, and N. Grandjouan. Collapsing Radiative Shocks in Xenon Gas on the Omega Laser. In *Proceedings of Inertial Fusion Science and Applications 2003*, pages 950–953, Monterey CA, 2004.

[70] A.B. Reighard, R.P. Drake, K.K. Dannenberg, J. Knauer, and L. Boireau S. Bouquet. Observation of Collapsing Radiative Shock in Laboratory Experiments. *Physics of Plasmas*, 13:082901, 2006.

[71] H.F. Robey, Ye Zhou, A.C. Buckingham, P. Keiter, B.A. Remington, and R.P. Drake. The onset of turbulence in high Reynolds number, accelerated flows. Part II. Experiment. *Phys. Plasmas*, 10:614, 2003.

[72] M. Rozyczka. 2-D hydrodynamical models of the stream-disk interaction in cataclysmic variables. II - Reflection of the stream from the disk. *Acta Astronomica*, 38:175–187, 1988.

[73] M. Rozyczka and A. Schwarzenberg-Czerny. 2-D Hydrodynamical Models of the Stream / Disk Interaction in Cataclysmic Binaries. *Acta Astronomica*, 37:141–+, 1987.

[74] D.D. Ryutov, R.P. Drake, J. Kane, E. Liang, B.A. Remington, and M. Wood-Vasey. Similarity Criteria for the Laboratory Simulation of Supernova Hydrodynamics. *Ap. J.*, 518(2):821, 1999.

[75] N. I. Shakura and R. A. Sunyaev. Black holes in binary systems. Observational appearance. *Astronomy & Astrophysics*, 24:337–355, 1973.

[76] N.I. Shakura and R.A. Sunyaev. Black holes in binary systems. Observational appearance. *Astronomy & Astrophysics*, 24(3):337–355, 1973.

[77] F.H. Shu, S.H. Lubow, and L. Anderson. Structure of contact binaries .3. Mass and energy-flow. *Astrophysical Journal*, 229(1):223–241, 1979.

[78] D. B. Sinars, G. R. Bennett, M. C. Herrmann, I. C. Smith, C. S. Speas, L. E. Ruggles, and J. L. Porter. Enhancement of x-ray yield from the z-beamlet laser for monochromatic backlighting by using a prepulse. *Review of Scientific Instruments*, 77(10):10E309, 2006.

[79] J. Smak. Eruptive binaries. VI - Rediscussion of U Geminorum. *Acta Astronomica*, 26:277–300, 1976.

[80] J. Smak. On the S-wave components of the emission lines in the spectra of cataclysmic variables. *Acta Astronomica*, 35:351–367, 1985.

[81] J. Smak. Disk Eclipse in IY UMa: Further Evidence for Stream Overflow. *Acta Astronomica*, 53:167–173, June 2003.

[82] C. Sorce, J. Schein, F. Weber, K. Widmann, K. Campbell, E. Dewald, R. Turner, O. Landen, K. Jacoby, P. Torres, and D. Pellinen. Soft x-ray power diagnostic improvements at the Omega Laser Facility. *Review of Scientific Instruments*, 77(10), Oct 2006. 16th Topical Conference on High-Temperature Plasma Diagnostics, Williamsburg, VA, MAY 07-11, 2006.

[83] J.M. Soures, R.L. McCrory, C.P. Verdon, A. Babushkin, R.E. Bahr, T.R. Boehly, R. Boni, D.K. Bradley, D.L. Brown, R.S. Craxton, J.A. Delettrez, W.R. Donaldson, R. Epstein, P.A. Jaanimagi, S.D. Jacobs, and et al. Direct-drive laser-fusion experiments with the OMEGA, 60-beam, 40 kJ, ultraviolet laser system. *Physics of Plasmas*, 3:2108–2112, May 1996.

[84] H. C. Spruit and R. G. M. Rutten. The stream impact region in the disc of WZ SGE. *Monthly Notices of the Royal Astronomical Society*, 299:768–776, September 1998.

[85] J.R. Thorstensen, F.A. Ringwald, R.A. Wade, G.D. Schmidt, and J.E. Norsworthy. Pg0027 + 260 - an example of a class of cataclysmic binaries with mysterious, but consistent, behavior. *Astronomical Journal*, 102:272–283, July 1991.

[86] B. van der Holst, G. Toth, and I. V. Sokolov. *Astrophysical Journal, Supplement*, 194(2):23, 2011.

[87] B. van der Holst, G. Toth, I.V. Sokolov, K. G. Powell, J. P. Holloway, E.S. Myra, Q. Stout, M.L. Adams, J. E. Morel, and R. P. Drake. A block-adaptive-mesh code for radiative shock hydrodynamics: Implementation and verification. *Astrophysical Journal Supplement Series*, 194:23, 2011.

[88] F. Verbunt. Accretion disks in stellar X-ray sources - A review of the basic theory of accretion disks and its problems. *Space Science Reviews*, 32:379–404, 1982.

[89] E. T. Vishniac. Nonlinear instabilities in shock-bounded slabs. *ApJ*, 428:186–208, June 1994.

[90] B. Warner. *Cataclysmic Variable Stars*. Cambridge University Press, September 2003.

[91] Jonathan Workman, James R. Fincke, George A. Kyrala, and Tim Pierce. Uniform large-area x-ray imaging at 9 kev using a backlit pinhole. *Appl. Opt.*, 44(6):859–865, Feb 2005.

[92] Guang yue Hu, Shen ye Liu, Jian Zheng, Chang shu Wu, Jing hong Li, Shun chao Wu, Ji-Yan Zhang, Jia min Yang, Guo hong Yang, Rong qing Yi, Hua bing Du, Yi xiang Huang, Xin Hu, and Yong kun Ding. Efficient k-shell x-ray sources produced with titanium foils. *Physics of Plasmas*, 14(3):033103, 2007.